ABSTRACT

New Approaches to Characterize and Simulate Reservoirs
by Machine Learning and Model-coupling Strategies

Jiajun Jiang, Ph.D.

Mentor: Scott C. James, Ph.D.

This dissertation comprises two topics. The first topic introduces an innovative multiphase, multicomponent reservoir simulator to simulate the solvent thermal resource innovation process (STRIP). In this framework, a STARS model injected steam only and governed the model by synchronizing temperature, pressure, and phase saturations for two parallel iterations of GEM models (GEM-1 and GEM-2). GEM models were used to mimic steam-CO_2 co-injection by adjusting injection rates and relative permeabilities to match targeted reservoir properties. The updated relative permeabilities representing viscosity reduction by CO_2 were then delivered back to the STARS model and the process repeated for the entire simulation. This new framework demonstrated the superior performance of STRIP compared to traditional steam injection.

The second topic investigates classification and segmentation of geologic features from image logs. CNNs were trained to identify vuggy facies from a well in the Arbuckle Group in Kansas. The complete dataset was culled by removing poor-quality images to generate a cleaned dataset for comparison. Various types of data were used to label the

image log for supervised learning. After hyperparameter optimization, median accuracy for vuggy/non-vuggy facies classification was 0.847 for the cleaned dataset (0.813 for the complete dataset). This study demonstrated the effectiveness of using microresistivity image logs in a CNN to classify facies while highlighting the importance of data quality control and hyperparameter optimization.

To characterize a reservoir, geologic features need to be segmented (pixel-wise identification). A modified U-Net, a form of FCN, was used to segment drilling-induced fractures (DIFs) from an image log. The U-Net algorithm was trained with borehole resistivity images (feature) against manually labeled image logs using two datasets (original and augmented where the mirror image of the original dataset was also included). A balanced cross-entropy loss function was used because of the unbalanced label data (60× more non-fracture than fracture pixels). The results demonstrated the robustness of this U-Net model for DIF segmentation. Moreover, the model trained on the augmented dataset outperformed that trained on the original dataset (intersection over union of 0.73 vs. 0.61). Finally, this study was in accord with previous studies that showed how overlapping pixels improved predictions.

New Approaches to Characterize and Simulate Reservoirs
by Machine Learning and Model-coupling Strategies

by

Jiajun Jiang, B.S., M.S.

A Dissertation

Approved by the Department of Geosciences

_____

Steven G. Driese, Ph.D., Chairperson

Submitted to the Graduate Faculty of
Baylor University in Partial Fulfillment of the
Requirements for the Degree
of

Doctor of Philosophy

Approved by the Dissertation Committee

_____

Scott C. James, Ph.D., Chairperson

_____

Stacy C. Atchley, Ph.D.

_____

John A. Dunbar, Ph.D.

_____

Joe C. Yelderman, Ph.D.

_____

David A. Jack, Ph.D.

Accepted by the Graduate School

August 2020

_____

J. Larry Lyon, Ph.D., Dean

Page bearing signatures is kept on file in the Graduate School.

TABLE OF CONTENTS

LIST OF FIGURES

LIST OF TABLES

ACKNOWLEDGMENTS

First, I must express my sincere gratitude to my mentor Dr. Scott C. James, who has granted me unlimited support. Through my trials and tribulations, he continuously spurred me to mature as a scholar and a man. I would like to thank Dr. Stacy Atchley, who has broadened my horizons to my career goals. I also sincerely thank to Dr. John Dunbar, who has been a constant source of knowledge and inspiration over the past five years. I would like to thank Dr. Joe Yelderman, who gave me support from both technical and emotional aspects. I would like to also thank Dr. David Jack, who put effort and insightful comments into my research projects. I would like to extend my gratitude to the Department of Geosciences and Graduate School at Baylor University for their financial support. I am indebted to Drs. Mohamad Mojarab, Weichang Li, Chicheng Xu, and Dawn McAlpin who are industry experts and contributed to my publications. Special thanks to Dr. Sharon Browning who trained me to become an awarded teacher. I would like to thank Paulette Penney, Jamie Ruth, and Janelle Atchley for their kindly help regarding my financial and scholastic issues. I am grateful for my lovely teammates Bulbul Ahmmed and Kathy Breen who encouraged me to conquer difficulties throughout my doctoral journey. Fred Schneider of RII International is gratefully acknowledged for his funding of the research in Chapter two. I wish to thank Lucinda Yang for her assistance with dissertation formatting.

DEDICATION

To my mentor, Dr. Scott C. James,
who rebuilt my career from scratch.

And

To my parents and grandmother, Weimin Jiang, Shengxia Lei, and Shujuan Du,
who have raised and supported me to be the person I am today.
献给我的父母和奶奶，蒋为民，雷省霞，和杜淑娟，
鸦有反哺之义，羊知跪乳之恩。

CHAPTER ONE

Introduction

In the second decade of 21st century, reducing environmental footprints and conducting digital transformation are two major challenges for the petroleum industry. This dissertation addressed two selected topics of these challenges. The first topic was simulating and evaluating the solvent thermal resource innovation process (STRIP), which is an eco-friendly, thermal-enhanced-oil-recovery (TEOR) method that provides improved recovery factors. The second topic focused on using cutting-edge deep-learning technology to automate traditionally labor-intensive geologic characterizations.

Compared to traditional TEOR methods, STRIP significantly improves the thermal efficiency and reduces greenhouse gas emission by delivering all the combustion heat to the pay zone. The second chapter developed a multi-phase multi-component simulation framework to simulate the STRIP technology. Traditionally, the commercial software package STARS (Thermal and Advanced Reservoir Simulator) employs a *K*-value method. However, the *K*-value method cannot accurately simulate the combustion byproduct CO_2 and steam co-injection process. Another simulator GEM (Compositional and Unconventional Simulator) has the capability to solve miscible or near-miscible gas injection but cannot handle thermal evolution. Hence, this innovative framework coupled the thermal features of STARS and compositional features of GEM. A STARS model governed the energy and material conservations for steam injection without CO_2. Two parallel GEM models (GEM-1 and GEM-2) synchronized temperature, pressure, and

phase saturation with the governing STARS model. GEM-1 simulated hot water injection with additional immiscible gas (CH_4) at increased injection rates to match gas (steam) saturations in STARS. A final GEM-1 run simulated hot water, CH_4, and CO_2 co-injection to mimic steam and CO_2 co-injection, which yielded the expected production increase. GEM-2 injected hot water and CH_4 at the calibrated rates from GEM-1 and yielded increased production in the final run of GEM-1 by adjusting relative permeabilities. Here, the adjusted relative permeabilities reflected the CO_2-altered rock-fluid properties. Finally, the updated relative permeabilities were fed back to STARS model and the simulation continued. Thermal efficiencies and oil recovery rates by STARS and traditional steam injection were compared through this new simulation framework. For this study, Jiajun Jiang developed and implemented ideas and analyzed results. Dr. Scott James provided critical review and served as corresponding author. Dr. Mohamad Mojarab provided manuscript review.

The second topic focused on charactering geologic features of carbonate reservoirs from microresistivity image logs. Unlike clastic reservoirs, carbonate reservoirs have poor permeability-porosity correlation due to the presence of diagenetic features such as vugs and fractures. The third chapter introduced an innovative deep-learning workflow for identifying vuggy facies from image logs. Traditionally, identifying vuggy facies is a labor-intensive process and requires the efforts of experienced geologists. Convolutional neural networks (CNNs), which have been broadly applied to multi-image classification in computer vision, were used in this study. First, the raw image-log data were clipped to half-foot interval. As a comparison, a cleaned dataset was generated by removing clipped images with poor quality. Next, facies labels

were interpreted based on core descriptions, conventional wireline logs, and nuclear magnetic resonance (NMR) data. The labeled data were split into training, validation, and test datasets. Finally, a hyperparameter optimization process was employed to improve model performance and reduce over-fitting. The results of models trained by the complete dataset and cleaned dataset were compared. For this study, Jiajun Jiang developed and implemented ideas and analyzed results. Dr. Chicheng Xu, Dr. Rui Xu, Dr. Scott James, and Dr. Weichang Li provided critical review. Dr. Dawn Jobe contributed to the data labelling process.

For an in-depth understanding subsurface rock-fluid properties and reservoir geomechanics, facies classification from image logs is only the first step for carbonated reservoir characterization. The deep-learning endeavors need to be extended to pixel-wise geologic feature segmentation. In the fourth chapter, a drilling-induced fractures (DIFs) segmentation pipeline was developed using a U-Net framework. Vertical DIFs were selected as segmentation targets for two reasons: (1) vertical DIFs are important indicators for horizontal maximum stress that significantly affect reservoir geomechanical analyses and (2) other types of fractures (such as natural fractures and en-echelon DIFs) were not widely distributed in the available dataset. U-Net is special form of a Fully Connected Network (FCN), which output labeled images. Labeled images were binary (0 denotes non-fracture pixels and 1 denotes fracture pixels) with the same dimensions as the input image. Image logs were labeled manually and clipped into a trainable size (128 × 128). An augmented training dataset was generated by simply mirroring the image and corresponding labels and adding these to the original dataset. The U-Net models were separately trained on these two training datasets and predictions

were made on the same test dataset. The importance of data augmentation and the robustness of the U-Net algorithm were evaluated by multiple classification/segmentation metrics. For this study, Jiajun Jiang developed and implemented ideas and analyzed results. Dr. Scott James provided critical review and served as corresponding author.

CHAPTER TWO

A Multiphase, Multicomponent Reservoir-simulation Framework for Miscible Gas and Steam Co-injection

This chapter was published as Jiang, J., James, S.C., Mojarab M., 2019, A Multiphase, Multicomponent Reservoir-simulation Framework for Miscible Gas and Steam Co-injection, *SPE Reservoir Evaluation & Engineering*.

Abstract

The Solvent Thermal Resource Innovation Process (STRIP), a downhole steam-generation technology, has the capacity to show improved recovery factors with a significantly reduced environmental footprint compared to traditional thermal-enhanced-oil-recovery (TEOR) methods, most notably by delivering all the combustion heat to the payzone. In this effort, a quarter-symmetry inverse-five-spot model and a multiphase, multicomponent, reservoir-simulation framework were used to simulate the STRIP technology. Commercial simulators such as CMG-STARS (thermal and advanced-processes reservoir simulator) often use the *K*-value approach to simulate TEOR. However, the method cannot simulate STRIP's carbon dioxide (CO_2) and steam coinjection because the *K*-value method does not consider miscible gas injection. On the other hand, CMG's GEM (compositional simulator) includes the effects of miscible gases but does not provide comprehensive support for steam injection processes, which are better handled by STARS. The novel simulation framework developed here leverages and combines the individual strengths of STARS (thermal features) and GEM (compositional features). In this framework, STARS simulated steam injection (but cannot directly simulate the effects of CO_2) and was the governing model that synchronized temperature,

pressure, and phase saturations for two parallel iterations of the GEM models (GEM-1 and GEM-2) at each time step. Immiscible CH_4 was added to GEM models to maintain gas saturations equivalent to the STARS model. GEM-1 simulated hot-water and CH_4 injection, but at increased rates to yield a pressure field and gas saturations equivalent to STARS. A final run of GEM-1 injected both CO_2 and hot water and demonstrated the expected increase in oil production. Calibrated injection rates from GEM-1 were specified in GEM-2 to ensure equivalence of the pressure field. Next, the GEM-2 model also simulated hot-water and CH_4 injection, but matched both water and oil productions along with oil saturations from the final GEM-1 run by altering relative permeabilities. Finally, the updated relative permeabilities were fed back to STARS and iteration proceeded. Results from this framework were verified against a STARS steam-injection simulation. Finally, when considering co-injection of CO_2, STRIP's superior performance was demonstrated through increased oil recovery and a lower steam-oil ratio.

Introduction

Petroleum engineers rely chiefly on numerical simulations to accurately predict hydrocarbon-reservoir performance under variable geologic conditions and development/exploitation strategies (Ertekin et al. 2001, Aziz and Settari 1979). Unlike conventional reservoirs, development methods for bitumen and heavy oil often rely on thermally enhanced oil recovery (TEOR) such as steam-assisted gravity drainage (SAGD, Cyr et al. 2001). Simulating TEOR methods is markedly more complicated than estimating the response of a black-oil reservoir (Chow and Butler 1996) because of the highly nonlinear response of the system to stimulation.

This effort was motivated by the need to simulate new technologies like RII North America Incorporated's (RII-NA's) Solvent Thermal Resource Innovation Process (STRIP), which is fuel efficient, environmentally friendly, and has the potential to recover more oil with less energy than traditional TEOR methods (Voskov et al. 2016). STRIP is a downhole steam-generation technology that delivers steam and combustion-product CO_2 to the payzone to generate a gas drive in heavy oil (Figure 2.1(a)). The steam transfers heat to the reservoir and the condensed hot water front drives the heated, more mobile oil. Simultaneously, the noncondensible CO_2 combustion product dissolves into the heavy oil to further decrease its viscosity. A STRIP burner is installed within the cavity of an existing well (drilled for primary production) completed in a heavy-oil reservoir (Figure 2.1(b)). Oxygen, fuel, and water are co-injected through annular tubes from the well head to the burner (Figure 2.1(c)). A slug of silane is cast down the innermost fuel tube and oxygen is coordinated to simultaneously issue from the burner (James et al. 2012, James et al. 2014, James et al. 2015). Silane auto-ignites in the presence of oxygen (Kondo et al. 1994, 1995, Hecht et al. 2011). The silane slug is chased with methane, which burns with stoichiometric oxygen (Hill et al. 1985). Water flows outside the combustion shroud to cool it and provide the steam source. Important advantages of STRIP include the fact that burners can be installed in existing wells, 100% of the combustion energy is delivered to the payzone, the potential to use produced gas as process fuel, and the potential to recycle produced water as the water source for steam. A steam quality of 0.8 was used in this study as specified according to STRIP combustion calculations by Voskov et al. (2016). Given the presence of CO_2, STRIP

injection fluids correspond to those often used in Expanding Solvent-SAGD (ES-SAGD), hence STRIP is an efficient version of solvent-steam co-injection technology.

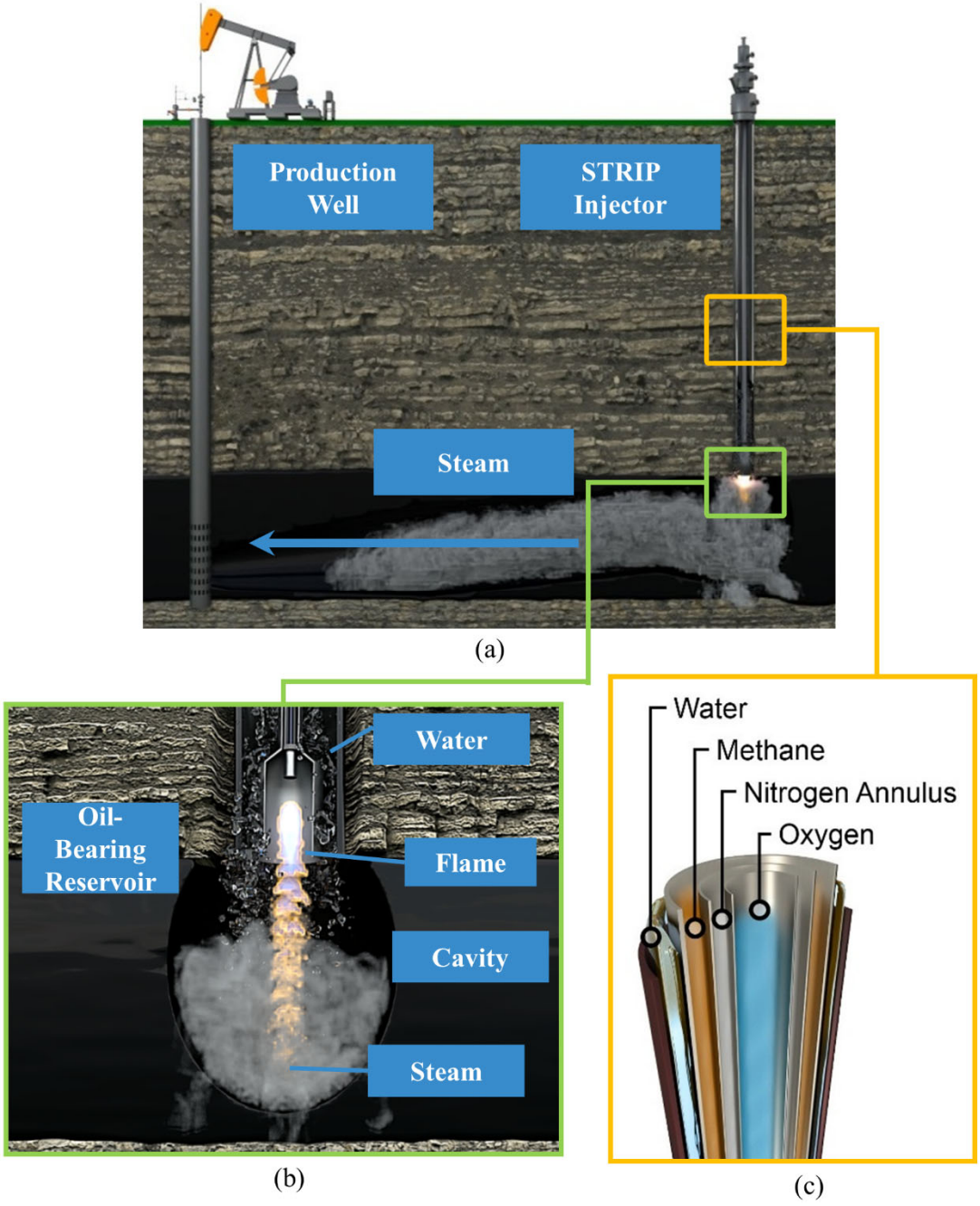

Figure 2.1. Cartoon of STRIP operation. (a) Heavy oil is displaced and driven by steam and CO_2 generation in the payzone. (b) The injected oxygen and fuel are auto-ignited by a slug of silane and generate steam and CO_2 in the combustion cavity. (c) Oxygen, fuel, and water are delivered through separate tubing strings from the wellhead to the burner.

A particular challenge to accurately simulating this complicated process is to faithfully replicate the highly nonlinear relationship between flow, transport, and heat transfer as components partition across phases and two common approaches are used to solve this multi-phase, multicomponent problem. One method uses *K* values, which are ratios of phases of single components calculated from flash calculations (Lucia 2010). The advantage of using *K* values is their computational efficiency because flash calculations are not required for each time step (Rannou et al. 2013). However, the *K* values are calculated from real-gas equations of state (EOS) and are quite sensitive to temperature and pressure, with lesser sensitivity to composition (Lucia et al. 2012, Lucia and Bonk 2012). Nevertheless, compositional effects cannot be ignored in near-miscible or miscible gas-injection systems such as STRIP (Orr 2007). The second, more computationally expensive approach solves EOS at each model gridblock at each time step (Hassanzadeh et al. 2008, Voskov et al. 2016), but it accurately describes the phase equilibrium and transport properties of reservoir fluids (Chang et al. 1996). Thermal compositional simulators have been studied for many years (Rubin and Buchanan 1985, Mifflin et al. 1991, Varavei and Sepehrnoori 2009, Voskov et al. 2016); however, because of numerical instabilities and computational expense, they have not been broadly implemented in commercial simulation software, although progress with research codes is underway (Voskov et al. 2016, Voskov 2017, Chen et al. 2018, Ganapathy and Voskov 2018, Khait et al. 2018).

There were three primary motivations for use of the full EOS approach over the *K*-value method:

1) Three-phase EOS and *K*-value approaches have been compared for steam and non-condensable gas co-injection (Zaydullin et al. 2017). That study concluded that EOS and *K*-values approaches yielded similar results. However, their ES-SAGD simulation injected methane and steam, which this framework can be extended to handle. The solubilities of methane in both heavy oil and water are about an order of magnitude lower than CO_2 for the same reservoir conditions (Dhima et al. 1999, Tharanivasan et al. 2006). Compositional effects cannot be ignored in near-miscible or miscible gas-injection systems such as STRIP (Orr 2007) so the EOS method is a sufficient if not better choice for steam-CO_2 co-injection. Other studies comparing EOS and *K*-value methods on hot-water injection and steam-condensable-gas co-injection, however, have demonstrated notable disparities (Heidari 2014, Varavei and Sepehrnoori 2009); production rates from these models showed that EOS-based cumulative oil production was more accurate than that for the *K*-value simulator.
2) During STRIP simulation, CO_2 and steam were considered miscible gases and *K* values were a function of composition. By definition, *K* values are calculated with respect to the key (or predominant) component only as a function of temperature and pressure. To relax this assumption, WINPROP uses Hand's Rule to calculate composition-dependent *K* values (CMG 2015c, Van-Quy et al. 1972). Hand's Rule is a tie-line relationship that, for a ternary system, assumes all tie-lines intersect at a point (CMG 2015b, Van-Quy et al. 1972, Young and Stephenson 1983). However, there are several drawbacks to

using Hand's Rule. First, it is an empirical method based on the assumption that all tie lines intersect at a point. Significant errors may result near the critical point (where the liquid and gas phases have the same density) because the *K* values are strong functions of composition near the critical point. Second, the phase envelopes may be nonlinear. Third, though not needed here, heavy oil can be composed of hundreds of component and selecting only one primary component for the *K*-value tables may lead to inaccuracies because composition-dependent *K* values are vectors with lengths equal to the number of components.

3) CO_2 is an important solution gas for producing heavy oil. The nature of heavy oil in terms of solution gas is quite different from conventional light oil. For example, foamy oil flow is a type of two phase oil-gas flow in which the gas phase (mostly CO_2) remains partially or completely dispersed in the oil (Maini 1999). Foamy oil drive and cyclic solvent/CO_2 injection are notably different from conventional solution gas drive and miscible/immiscible solvent injection (Maini 1999, Saner and Patton 1986).

This study outlines the development of a new thermal compositional simulation framework based on the widely used commercial tool, Thermal and Advanced Processes Reservoir Simulator (STARS, CMG 2015b) developed by Computer Modelling Group Ltd. (CMG), coupled to the Compositional and Unconventional Oil and Gas Reservoir Simulator (GEM, CMG 2015a) through the Parameter ESTimation software, PEST (Doherty 2016b, 2016a). This effort was motivated by RII-NA's desire to simulate their STRIP technology using commercial software accepted as the industry standard.

The non-condensable gases CO_2 and CH_4 have different liquid-gas relative permeabilities than water vapor (Nourozieh et al. 2015). However, simulating the effects of these non-condensable gases on endpoint saturations is an area of active research and was not attempted here. In GEM-2, the updated relative permeabilities were adjusted to match the production rates and oil saturations for the entire model domain, so the relative permeabilities were regarded as average relative permeabilities throughout the model domain. This was necessary because adding adjustable permeability parameters for each model cell would be computationally intractable and ill-defined with many more parameters than calibration data points.

The theory of rate-dependent dissolution and exsolution reveals that gas dissolution into bitumen at low temperature is slow and that exsolution of dissolved gas is minimal without significant pressure variation (Nourozieh et al. 2012). Another theory indicates that non-condensable gas can improve the thermal efficiency of steam-chamber development, because non-condensable gas can accumulate between the cold reservoir and steam front and acts as an insulator (Nourozieh et al. 2015). However, these effects were not explicitly studied here.

Mathematical Formulations

A comprehensive numerical model that considers the different mechanisms of fluid flow, reactive transport, and thermodynamic interactions within heterogeneous porous media is required to optimize ES-SAGD processes in heavy oil and bitumen reservoirs. Simulating ES-SAGD is complicated by the nonlinear interrelationships between oil, water, and condensable and non-condensable gas phases, all of which undergo varying degrees of fluid flow and transport. A particular challenge to this

modeling approach is to accurately describe how components partition across the multiple phases, which yields a highly nonlinear coupling between flow and heat transfer. There is an active debate as to whether the non-condensable gas accumulates at the steam front (thereby reducing heat transfer to the oil phase and decreasing oil production) or whether it accumulates at the top of the reservoir (where it acts as an insulator to reduce heat losses to the overburden thereby improving ES-SAGD thermal efficiency). Some experiments suggest that co-injection of a non-condensable gas with steam may reduce the steam-oil ratio (SOR, Nourozieh et al., 2015). A verified model of these scenarios may help resolve this debate.

In STARS, to ensure energy and mass conservation, accumulations are equal to the rate of change of net inflow plus sources and sinks. Mass conservation for flowing (and absorbing) component *i* is:

$$\frac{\partial}{\partial t}\left[V_{\mathrm{f}}\left(\rho_{\mathrm{w}}S_{\mathrm{w}}w_i+\rho_{\mathrm{o}}S_{\mathrm{o}}x_i+\rho_{\mathrm{g}}S_{\mathrm{g}}y_i\right)+V_{\mathrm{v}}A_i\right]= \\ \left(\rho_{\mathrm{w}}v_{\mathrm{w}}w_i+\rho_{\mathrm{o}}v_{\mathrm{o}}x_i+\rho_{\mathrm{g}}v_{\mathrm{g}}y_i+\phi\rho_{\mathrm{w}}D_{\mathrm{w}_i}\Delta w_i+\phi\rho_{\mathrm{g}}D_{\mathrm{g}_i}\Delta y_i+\phi\rho_{\mathrm{o}}D_{\mathrm{o}_i}\Delta x_i\right)+\left(\rho_{\mathrm{w}}q_{\mathrm{w}_k}w_i+\rho_{\mathrm{o}}q_{\mathrm{o}_k}x_i+\rho_{\mathrm{g}}q_{\mathrm{g}_k}y_i\right), \tag{1}$$

where t is time, V_{f} is volume of all fluid phases, w_i, x_i, and y_i are mole fraction of component i in aqueous, oleic, and gaseous phases, respectively, V_{v} is void volume, ρ_{w}, ρ_{o}, and ρ_{g} are mass densities of aqueous, oleic, and gaseous phases, respectively, S_{w}, S_{o}, and S_{g} are saturations of the aqueous, oleic, and gaseous phases respectively, ϕ is porosity, A_i is adsorption level, v_{w}, v_{o}, and v_{g} are the volumetric flow rates of aqueous, oleic, and gaseous phases, respectively, D_{w}, D_{o}, and D_{g} are the component dispersibilities in aqueous, oleic, and gaseous phases, respectively (component dispersibilities in the three phases are functions of geometric factors and component dispersion coefficients),

Δw_i is mole fraction change of component i in the aqueous, phase, q_w, q_o, and q_g are the volumetric well flow rates for aqueous, oleic, and gaseous phases, respectively, and subscript k is the well layer number, which is the model layer index vertical to the well path.

Energy is conserved as:

$$\frac{\partial}{\partial t}\left[V_f\left(\rho_w S_w U_w + \rho_o S_o U_o + \rho_g S_g U_g\right) + V_v c_s U_s + V_r U_r\right] = \left(\rho_w v_w H_w + \rho_o v_o H_o + \rho_g v_g H_g + \gamma\Delta T\right) + \left(\rho_w q_{w_k} H_w + \rho_o q_{o_k} H_o + \rho_g q_{g_k} H_g\right), \quad (2)$$

where U_r is energy per rock volume, c_s is total solids concentration, U_w, U_o, U_g, and U_s are the internal energies of aqueous, oleic, gaseous, and solid phases, respectively, γ is the thermal transmissibility (the product of geometric factors and thermal conductivity), ΔT is temperature change, and H_w, H_o, and H_g, are the enthalpies of aqueous, oleic, and gaseous phases, respectively.

The K values calculated from a real-gas EOS in STARS are most sensitive to temperature and pressure, but compositional effects must be considered (Orr 2007). During the STRIP simulation, CO_2 and steam were considered miscible gases and K values were a function of composition.

To address the shortcomings of the K-value method, GEM solves the EOS every time step when simulating solvent injection. GEM uses CMG's advanced EOS compositional simulator based on the Peng-Robinson EOS for complex phase behavior involving CO_2 (CMG 2015a).

The material balance finite-difference equations in GEM are:

$$\Delta\tau_{\mathrm{o}}^{m}x_{i}^{m}\left(\Delta P^{n+1}-\gamma_{\mathrm{o}}^{m}\Delta\mathrm{D}\right)+\Delta\tau_{\mathrm{g}}^{m}y_{i}^{m}\left(\Delta P^{n+1}+\Delta P_{\mathrm{cog}}^{m}-\gamma_{\mathrm{g}}^{m}\Delta\mathrm{D}\right)+q_{i}^{m}-\frac{V}{\Delta T}\left(M_{i}^{n+1}-M_{i}^{n}\right)=0$$

, (3)

$$\Delta\tau_{\mathrm{w}}^{m}\left(\Delta P^{n+1}-\Delta P_{\mathrm{cwo}}^{m}-\gamma_{\mathrm{w}}^{m}\Delta D\right)+q_{n_{\mathrm{c}}+1}^{n+1}-\frac{V}{\Delta T}\left(M_{n_{\mathrm{c}}+1}^{n+1}-M_{n_{\mathrm{c}}+1}^{n}\right)=0\,, \quad (4)$$

where τ_{o}, τ_{g}, and τ_{w} are the molar transmissibilities (product of effective permeability and geometric factors) of oleic, gaseous, and aqueous phases, respectively, P_{cog} and P_{cwo} are oil-gas and water-oil capillary pressures, respectively, P is oleic phase pressure, V is gridblock volume, q_i is injection/production rate of component i, n_c is number of non-water components, $n_c + 1$ refers to water, q_{n_c+1} is injection/production rate of water, Δ is depth, T is temperature, superscripts n and $n + 1$ are the previous and current time levels, when using the explicit solver, superscript m is n while it is $n + 1$ for the implicit solver, γ_{o}, γ_{g}, and γ_{w} are the pressure gradients of oleic, gaseous, and aqueous phases, respectively, M_i is moles of component i per unit gridblock volume, and M_{n_c+1} is moles of water per unit of gridblock volume.

The oil simulated in this model was a typical heavy oil described in Table 2.1. Initially, no gases were assumed dissolved in the oil (dead oil). The Peng-Robinson EOS estimated component-phase equilibrium behavior (Robinson and Peng 1978). Mixture viscosities were calculated according to the Modified Pedersen Method (Pedersen and Fredenslund 1987). Figure 2.2 shows the viscosity of dead oil as a function of temperature. WINPROP estimated EOS coefficients, which were used to predict gas-oil system behaviors including solubility of gas in oil for the GEM simulations. Gas

dissolution into aqueous phases was calculated using Henry's Law with Harvey's correlation applied to CO_2 (Harvey 1996).

Table 2.1. Heavy oil data.

Specific gravity	1.012
Molecular weight (kg/kmol)	600
Density (kg/m^3)	1011.8

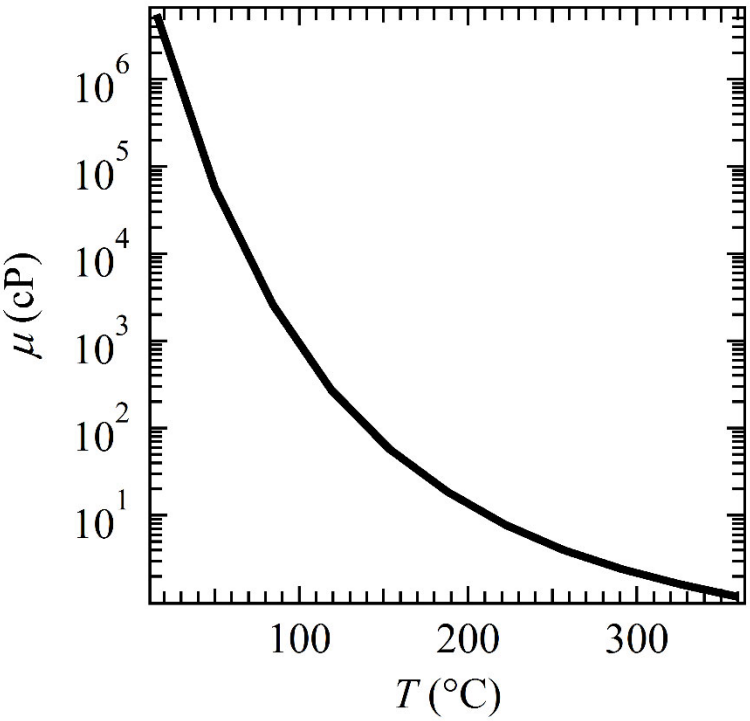

Figure 2.2. Heavy oil viscosity changes with temperature.

The simulated reservoir was an inverted five-spot, quarter-symmetry model with steam injection (Figure 2.3) and three layers in the vertical. The top and bottom layers were impermeable and represent overburden and underburden rocks. Heat transfer was allowed through all model layers. In traditional TEOR methods, wellbore heat loss can be as high as 50% (Petroleum Technology Alliance Canada 2005). Because STRIP generates steam directly in the payzone, wellbore heat loss was not included in the

framework. Reservoir physico-chemical parameters including dimensions, initial conditions, and thermal properties are listed in Table 2.2. Well-configuration information is presented in Table 2.3.

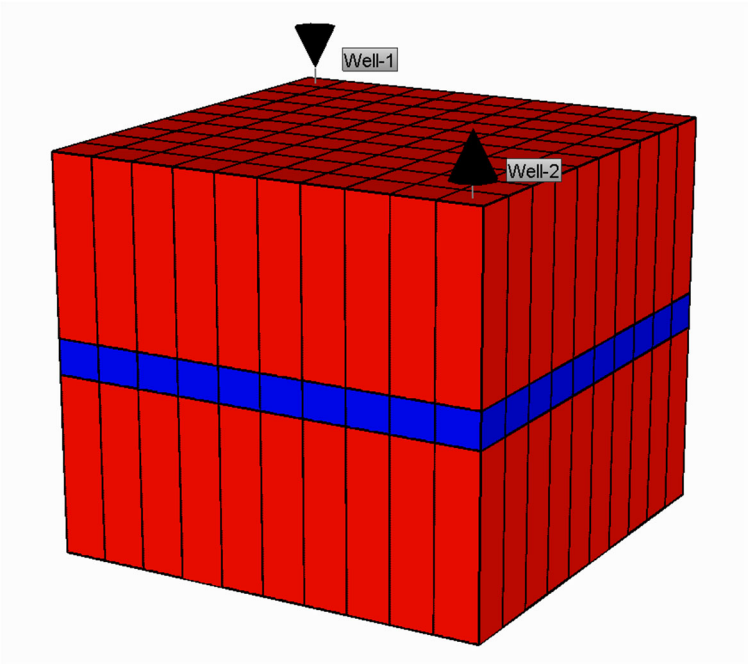

Figure 2.3. A 3D view of the inverse five-spot, quarter-symmetry model. Underburden and overburden layers in red are impermeable but conduct heat. The layer in blue is the reservoir.

Table 2.2. Reservoir conditions.

	Reservoir	Overburden	Underburden
Thickness (m)	10	50	50
Reservoir dimensions (m^3)	25×25×10	25×25×50	25×25×50
Grid block size (m^3)	2.5×2.5×10	2.5×2.5×50	2.5×2.5×50
Depth (m)	400	350	410
Porosity (-)	0.3	0	0
Permeability (md)	1,000	0	0
Oil saturation	0.7	0	0
Water saturation	0.3	0	0
Gas saturation	0	0	0
Reservoir temperature (°C)	11	11	11
Reservoir pressure (MPa)	1.596	1.596	1.596
Volume heat capacity (J/m^3-°C)	2.6×10^6	2.7×10^6	2.7×10^6
Rock thermal conductivity (J/m-d-°C)	232,877	230,000	230,000
Oil thermal conductivity (J/ m-d-°C)	12,960	12,960	12,960
Water thermal conductivity (J/ m-d-°C)	52,704	52,704	52,704
Gas thermal conductivity (J/ m-day-°C)	4,000	4,000	4,000

Table 2.3. Well configurations.

	STARS	GEM-1	GEM-1 final run	GEM-2
BHP (MPa)	8	8	8	8
Steam temperature (°C)	230	n/a	n/a	n/a
Steam quality (−)	0.8	n/a	n/a	n/a
Injected water mole fraction (−)	0.9	0.9	0.9	0.9
Injected CH_4 mole fraction (−)	0.1	0.1		0.1
Injected CO_2 mole fraction (−)	0	0	0.1	0
Water (steam) injection rate, q_w (m^3/d)	10	Varied	90 mole% of calibrated GEM-1 $q_w + q_{CH_4}^{mod}$	Same as GEM-1
Methane injection rate, q_{CH_4} (m^3/d)	0	Varied	10 mole% of calibrated GEM-1 $q_w + q_{CH_4}^{mod}$	Same as GEM-1

Two model parameters, maximum bottom-hole pressure (BHP) and maximum injection rate, constrain the STARS injection rate. By specifying the maximum BHP as

8 MPa, which is higher than typical situations, and a maximum injection rate of 10 m^3/day, this ensured that a constant injection rate of 10 m^3/day was maintained throughout the STARS simulation. Note that the high maximum BHP was never achieved during the simulation because it was constrained by the injection rate. The constant injection rate was required for the framework because without it, BHP could limit the volume input to the system, but only if the injection rate caused that pressure to be exceeded. If this condition was not met, PEST would not identify BHP as a sensitive variable, thus necessitating the arbitrarily high maximum BHP when calibrating maximum injection rate.

As opposed to STARS, GEM decouples the phase-equilibrium equations and solves them separately in an inner loop (Collins et al. 1992, CMG 2015a). GEM calculates the flow for each component, *i*, rather than the flow of each phase. Hence, GEM is better suited to solve the CO_2-steam co-injection problem. The Sigmund method was used to calculate non-condensable gas diffusion (Sigmund 1976). In GEM, fluid mixing is a combined result of diffusion, local velocity gradients, locally heterogeneous streamline lengths, and mechanical mixing (Lake 1989). However, GEM is not a thermal simulator, although different temperatures are allowed in each gridblock.

The PEST software suite facilitates parameter estimation and uncertainty analysis of complex models (Moore and Doherty 2005). In the GEM models, several parameters (injection rates and relative permeability coefficients) were calibrated to match previous STARS and GEM model outputs. PEST calibrated two GEM models by adjusting their input parameters such that their outputs matched previous model outputs (specified observation data). This was accomplished by minimizing an objective function

formulated as a weighted sum of squared errors between GEM outputs and the specified observation data. The framework managing the STARS model and GEM calibrations was built in MATLAB (although Python would work just as easily).

Coupling Methodology

CMG's STARS simulates thermal, non-isobaric, three-phase flow and transport (oil, water, and steam), but does not directly include the effects of a non-condensable CO_2 phase, which is miscible in the steam phase and has significant solubility in both the oil and water phases. On the other hand, CMG's GEM simulates the non-condensable CO_2 phase, but it is an isothermal model. The new framework couples STARS and GEM to simulate ES-SAGD technologies like STRIP.

In hydrocarbon reservoirs, relative permeabilities are strong functions of the solvent-gas concentrations in the vapor phase (Schneider and Owens 1976). These solvents also decrease liquid-phase viscosities particularly for heavy oils, which also swell, resulting in enhanced oil mobility. Considered from a different perspective, the physico-chemical changes effected by the solvent are conceptually equivalent to an increase in the relative permeability of the formation. The idea forwarded here is to use an isothermal GEM solvent-water co-injection simulation to identify augmented relative permeabilities that result in the equivalent enhanced oil mobility achieved through an ES-SAGD process. Then, STARS simulations using these augmented relative permeabilities will reflect the effects of non-isothermal co-solvent injection despite the fact that STARS only has the capacity to expressly simulate the effects of steam injection. A complication that had to be overcome was the incongruity between STARS and GEM because each uses different multi-phase and thermodynamic properties for water. Specifically, GEM

does not have the ability to consider the steam phase. To represent the steam phase in GEM, an immiscible gas phase (CH_4) was added to maintain gas saturations equivalent to the STARS model. If live oil was simulated, injecting N_2 would have been a better option to distinguish oil content from injected gas. The water and CH_4 injection rates in the GEM model were adjusted to match the pressure field and gas saturations from the STARS model. Even though hot water and CH_4 injections were used in GEM, the overall framework reflects the use of steam (not hot water) injection for two reasons: (1) the STARS model with steam injection governs mass and energy conservation; (2) the GEM models uses hot water and CH_4 co-injection to mimic the steam environment. An iterative approach was required to solve this nonlinear process wherein the strengths of each model were leveraged to overcome their individual weaknesses.

Overall, the framework required iteration of three models as shown in the flow chart in Figure 2.4: one STARS model and two GEM models for each user-defined time increment until the total simulation time period was completed. STARS simulated steam injection (but cannot directly simulate the effects of CO_2) and was the governing model that synchronized temperature, pressure, and phase saturations for the GEM models at each time step.

Framework Design

This novel framework leverages and combines the individual strengths of STARS (thermal features) and GEM (multicomponent features). A MATLAB script executed STARS, GEM, and PEST and also read and exchanged information between the three programs according to the flow chart in Figure 2.4, with steps summarized below:

0) Initialize the framework; see Note 0) below.
1) Execute the STARS model; see Note 1) below.
2) MATLAB Module 1: Generate the PEST-1 and GEM-1 input files; see Note 2) below.
3) Execute the PEST-1 calibration of GEM-1; see Note 3) below.
4) MATLAB Module 2: Generate the Final GEM-1 input file; see Note 4) below.
5) Execute the Final GEM-1 model; see Note 5) below.
6) MATLAB Module 3: Generate the PEST-2 and GEM-2 input files; see Note 6) below.
7) Execute the PEST-2 calibration of GEM-2; see Note 7) below.
8) MATLAB Module 4: Generate the next STARS input file; see Note 8) below.

Additional details are noted below:

0) All STARS and GEM models shared the same grid, reservoir properties, and well locations, which were sent to the first execution of STARS and the MATLAB script as initial and boundary conditions. Initial relative permeabilities are shown in Figure 2.5.Time was initialized, (e.g., $t = 0$ days), the STARS/GEM model time steps were set (e.g., $\delta t = 0.1$ days), the framework-iteration time step was established (e.g., $\Delta t = 1$ day), and the end time specified (e.g., $t_{max} = 365$ days).
1) Run the STARS model from t to $t + \Delta t$ in steps of δt (see Tables 2.1, 2.2, and 2.3)

2) Because there is no heat equation solution, spatially variable temperatures were independently specified in each gridblock of the GEM-1 input file equal to the output from the STARS run (i.e., $t \approx t + \Delta t$). Moreover, the effects of steam condensation were incorporated by injecting CH_4 ($q_{CH_4}^{mod}$), but only after modifying its physical properties in the GEM-1 input to be a weighted average of 90 mol% steam and 10 mol% CO_2 calculated at the P and T (output from the STARS model) in each gridblock – importantly with zero miscibility.

Moreover, because GEM ensures saturation conservation and global compositions for oleic and gaseous phases, STARS outputs (in terms of phase saturations) were modified as:

$$S_o + S_g + S_w = 1, \tag{5}$$

$$Z_o + Z_{CH_4} = 1, \tag{6}$$

$$\left(Z_o + Z_{CH_4}\right)\left(S_o + S_g\right) + S_w = 1, \tag{7}$$

$$Z_o = \frac{\frac{S_o}{d_o}}{\frac{S_o}{d_o} + \frac{S_{CH_4}}{d_{CH_4}}}, \tag{8}$$

$$Z_{CH_4} = \frac{\frac{S_{CH_4}}{d_{CH_4}}}{\frac{S_o}{d_o} + \frac{S_{CH_4}}{d_{CH_4}}}, \tag{9}$$

where Z_o and Z_{CH_4} are global compositions of oil and methane, respectively, d_o and d_{CH_4} are the molar densities at the temperature and pressure in each gridblock, and S_w, S_o, and S_g are saturations of aqueous, oleic, and gaseous phases in each gridblock. The preceding equations were used to translate STARS outputs into the calibration targets in the PEST-1 input file, which were used to when minimizing the objective function (see Table 2.5).

3) Calibrate the GEM-1 model (from t to $t + \Delta t$ in steps of δt) by adjusting water and modified-CH_4 volumetric well-injection rates, q_w and $q_{CH_4}^{mod}$, respectively, within specified bounds (Table 2.4). Initial values of these rates supplied to PEST came from the STARS model run.
4) To approximate the combustion products from the STRIP process, which were assessed by Voskov et al. (2016), q_{CO_2} was specified in the Final GEM-1 input file as 10 mole% of the total STARS injection rate ($q_w + q_{CH_4}$) thereby respecting stoichiometric combustion of CH_4 with pure oxygen while q_w was specified as the remaining 90 mole%. In the Final GEM-1 input run, global compositions and water saturations (indicated with the asterisk) were:

$$S_w^* = S_w \frac{1 - Z_o(1 - S_w) - Z_{CO_2}(1 - S_w)}{1 - Z_o(1 - S_w)}, \tag{10}$$

$$Z_{CH_4}^* = Z_{CH_4} \frac{1 - Z_o(1 - S_w) - Z_{CO_2}(1 - S_w)}{1 - Z_o(1 - S_w)} \frac{1 - S_w}{1 - S_w^*}, \tag{11}$$

$$Z_{\mathrm{o}}^{*} = Z_{\mathrm{o}} \frac{1-S_{\mathrm{w}}}{1-S_{\mathrm{w}}^{*}}, \tag{12}$$

$$Z_{\mathrm{CO_2}}^{*} = Z_{\mathrm{CO_2}} \frac{1-S_{\mathrm{w}}}{1-S_{\mathrm{w}}^{*}}, \tag{13}$$

where S_{w}, $Z_{\mathrm{CH_4}}$, and Z_{o} are outputs from the calibrated GEM-1 model while $Z_{\mathrm{CO_2}}$ was from the Final GEM-1 run at the previous time step (or zero the first time through the framework).

5) Execute the Final GEM-1 model from t to $t + \Delta t$ in steps of δt.

6) Build the GEM-2 input file using gridblock P and T from the MATLAB Module 1 as well as injection rates from q_{w} and $q_{\mathrm{CH_4}}^{\mathrm{mod}}$ from the calibrated GEM-1 run.

   Specify the calibration targets as the oil and water production rates, Q_{o} and Q_{w}, respectively, as well as the spatially variable $Z_{\mathrm{CH_4}}^{*}$ and Z_{o}^{*} calculated from STARS saturations making sure to also use $Z_{\mathrm{CO_2}}^{*}$ from the preceding Final GEM-1 run (output from t) in the PEST-2 input file.

   In the GEM-2 calibration (from t to $t + \Delta t$ in steps of δt), there were 27 observations to match comprising S_{o} for each of the 25 gridblocks along with water and oil productions (see Table 2.5). GEM-2 was calibrated to match productions, hence larger weights were assigned to water and oil productions during calibration (Table 2.6). Increased oil mobility due to the CO_2 combustion products from STRIP was represented by adjusting the relative permeability parameters listed in defining Stone's Model II

relative permeability curves (CMG 2015b, Aziz and Settari 1979). Because GEM ensures the maximum κ_{ro} for both oil-water (κ_{rocw}) and gas-fluid (κ_{rogcg}) relative permeability functions to be equal. κ_{rogcg} was fixed to κ_{rocw}, decreasing the number of adjustable parameters to 15. Next, GEM-2 was calibrated to match water and oil productions from the final GEM-1 run, as well as each payzone gridblock's oil saturations by varying the 16 parameters listed in Table 2.5.

7) . In Stone's Model II, relative permeability curves are defined as:

$$\kappa_{rw} = \kappa_{rwiro}\left(\frac{S_w - S_{wcrit}}{1.0 - S_{wcrit} - S_{oirw}}\right)^{N_w}, \tag{14}$$

$$\kappa_{row} = \kappa_{rocw}\left(\frac{S_o - S_{orw}}{1.0 - S_{wcon} - S_{orw}}\right)^{N_{ow}}, \tag{15}$$

$$\kappa_{rg} = \kappa_{rogcl}\left(\frac{S_g - S_{gcrit}}{1.0 - S_{gcrit} - S_{oirg} - S_{wcon}}\right)^{N_g}, \tag{16}$$

$$\kappa_{rog} = \kappa_{rogcg}\left(\frac{S_l - S_{org} - S_{wcon}}{1.0 - S_{gcon} - S_{org} - S_{wcon}}\right)^{N_{og}}, \tag{17}$$

where S is endpoint saturation, specifically S_{wcrit} is critical water saturation, S_{wcon} is connate water saturation, S_{oirw} is irreducible oil saturation in the water-oil relative permeability function, S_{orw} is residual oil saturation in the water-oil relative permeability function, S_{oirg} is irreducible oil saturation in the gas-liquid relative permeability function, S_{org} is residual oil saturation in the gas-liquid relative permeability

function, S_{gcrit} is critical gas saturation above which gas flows, S_{gcon} is connate gas saturation, κ_{rocw} is oil relative permeability at connate water saturation, κ_{rwiro} is water relative permeability at irreducible oil saturation, κ_{rgcl} is gas relative permeability at connate liquid saturation, κ_{rogcg} is oil relative permeability at connate gas saturation, and N_w, N_{ow}, N_{og}, and N_g are exponents for κ_{rw}, κ_{rg}, κ_{row}, and κ_{rog}, respectively.

Finally, these 15 calibrated relative permeability parameters were used to formulate the relative permeabilities (κ_{rw}, κ_{rg}, κ_{row}, and κ_{rog} described in the next Section) built into STARS input file that will simulate the next time step (or output the overall framework simulations if t_{max}, was exceeded).

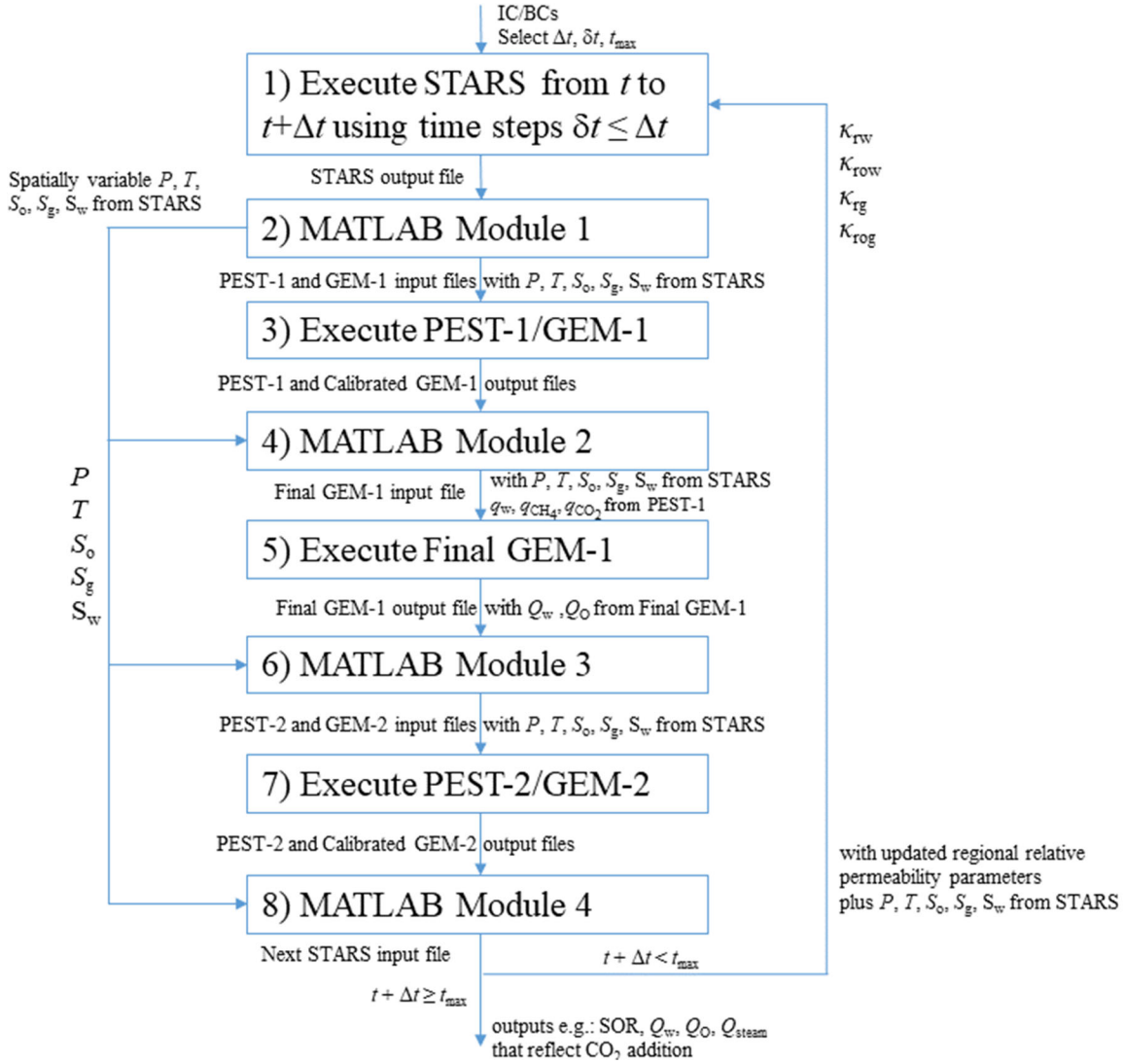

Figure 2.4. Flow chart for the simulation framework. For each time step, the governing STARS model runs with updated relative permeabilities from the GEM-2 calibration, which was run with appropriate $q_{\mathrm{w}} + q_{\mathrm{CH_4}}^{\mathrm{mod}}$ and $q_{\mathrm{CO_2}}$ injection rates from the final run of GEM-1.

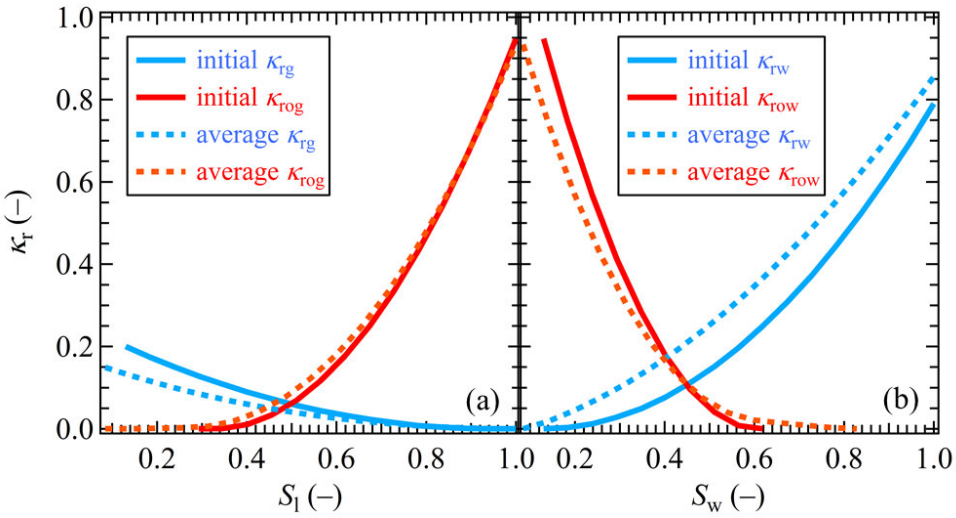

Figure 2.5. (a) Initial and adjusted average relative permeabilities for the liquid-gas system. (b) Initial and adjusted average relative permeabilities for the oil-water system. The solid curves are initial κ_r curves, and the dashed curves are adjusted average κ_r curves from GEM-2.

Table 2.4. Adjustable parameters for GEM-1.

Adjustable Parameter	Initial value	Lower bound	Upper bound
q_w (m^3/day)	10	0	15
CH_4 injection rate (m^3/day)	0	0	5

Table 2.5. Number of adjustable parameters and observations with corresponding weights for the GEM calibrations.

Model	Adjustable parameters	Numbers of observations	Weight
GEM-1	P at each gridblock	25	1
	S_o and S_g at each gridblock	25	1
GEM-2	Q_w for $t + \Delta t$	1	20
	Q_o for $t + \Delta t$	1	20
	S_o at each gridblock	25	1

Table 2.6. Adjustable parameters from the GEM-2 calibration defining the relative permeability curves.

Adjustable parameter	Initial value	Lower bound	Upper bound
S_{wcrit}	0.13	0.05	0.3
S_{wcon}	0.13	0.04	0.3
S_{oirw}	0	0	0.2
S_{orw}	0.39	0.2	0.45
S_{oirg}	0	0	0.1
S_{org}	0.2	0.05	0.25
S_{gcrit}	0.05	0	0.1
S_{gcon}	0	0	0.5
κ_{rocw}	0.948	0.8	1
κ_{rwiro}	0.79	0.6	1
κ_{rgcl}	0.2	0.1	0.3
κ_{rogcg}	κ_{rocw}	Fixed	Fixed
N_w	2	1	3
N_{ow}	2	1	3
N_{og}	2	1	3
N_g	2	1	3

Model Analysis

To ensure mass and energy conservation, a verification model demonstrated that the framework can replicate the results of a simple steam-injection model from STARS. A verification model was built using the reservoir properties, well configurations, and fluid properties described in Tables 2.1−2.4 and 2.6 except that the injection composition in the final run of GEM-1 was 100% water (no CO_2). For verification, the framework must be able to faithfully represent a steam-injection model. Figure 2.6 shows that the recovery factors from both the new framework and the STARS steam-injection model for a year-long run are identical. To further verify the framework, a coarsened model with 5×5 m^2 gridblocks (four times the original resolution of 2.5×2.5 m^2) also demonstrated an identical match.

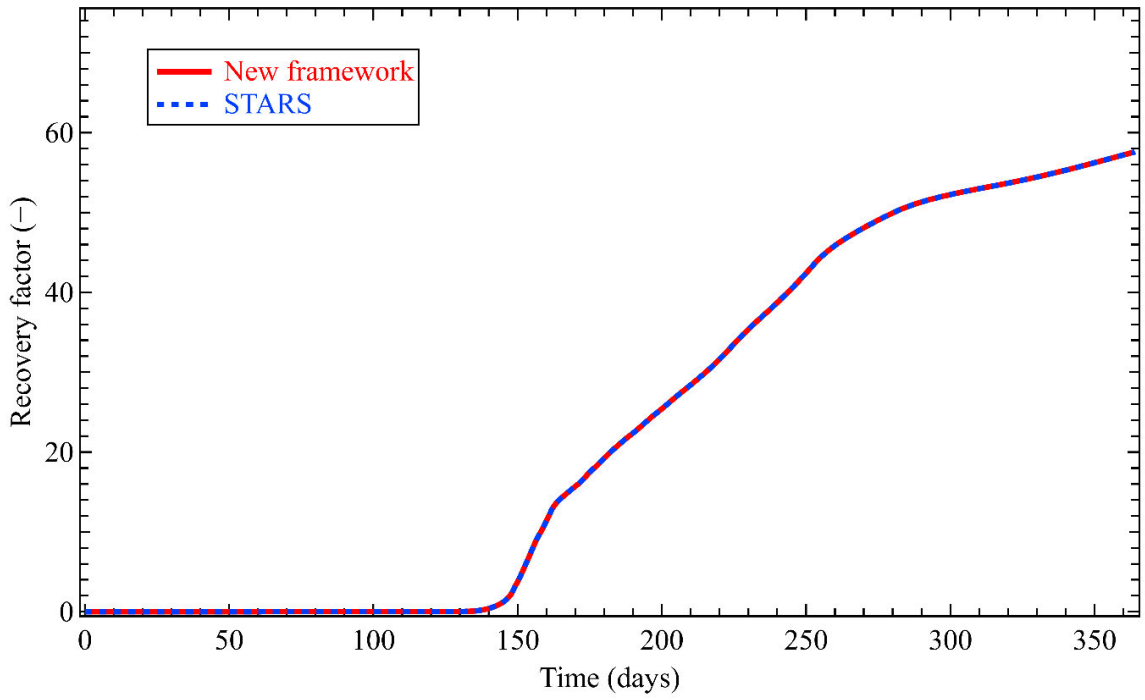

Figure 2.6. Recovery factor for a steam-injection-only STARS simulation compared to the equivalent from the new framework. The blue curve is from STARS and the red curve is from the new framework.

Using the verified framework, a CO_2-steam co-injection model was run for one year. Figure 2.7 compares recovery factors from the CO_2-steam co-injection model from the new framework to an equivalent STARS steam-injection model. At equivalent reservoir conditions and volumetric injection rates, pure steam and STRIP's CO2-steam mixtures will have different enthalpies. Because this study focused on developing a new coupling method for simulating and comparing the performance of STRIP to steam injection at equal enthalpy injection rates, no enthalpy correction was considered although such a correction could be added in the Final GEM-1 run. More oil was produced from the CO_2-steam co-injection model than from the steam-injection model. At the end of the year-long simulation, the CO_2-steam co-injection model produced 6% more oil than the steam-injection model. Figure 2.8 compares oil production rates from steam injection to those from STRIP. After 129 days of operation, the CO_2-steam co-injection model indicated injection/production connectivity (with oil production rates > 5 m^3/day), whereas the steam-injection model had connectivity after 146 days of operation. Unconventional oil and gas companies tend to be smaller companies subject to larger financial pressure (Weijermars 2011). The early breakthrough between injection and production wells would improve economic feasibilities and mitigate early cash-flow problems. The increased productivity and early breakthrough illustrate the effects of CO_2 viscosity reduction on oil recovery. Steam injection alone reached a minimum cumulative SOR of 3.6 on the 281st day while the CO_2-steam co-injection achieved a minimum cumulative SOR of 3.1 on 262nd day (Figure 2.9). At the end of the simulation, the cumulative SOR for the CO_2-steam co-injection model was 3.8 compared to 4.0 for steam

injection. The high SOR (out of range in Figure 2.9) was due to minimal production rates before a steam-chamber connection was established.

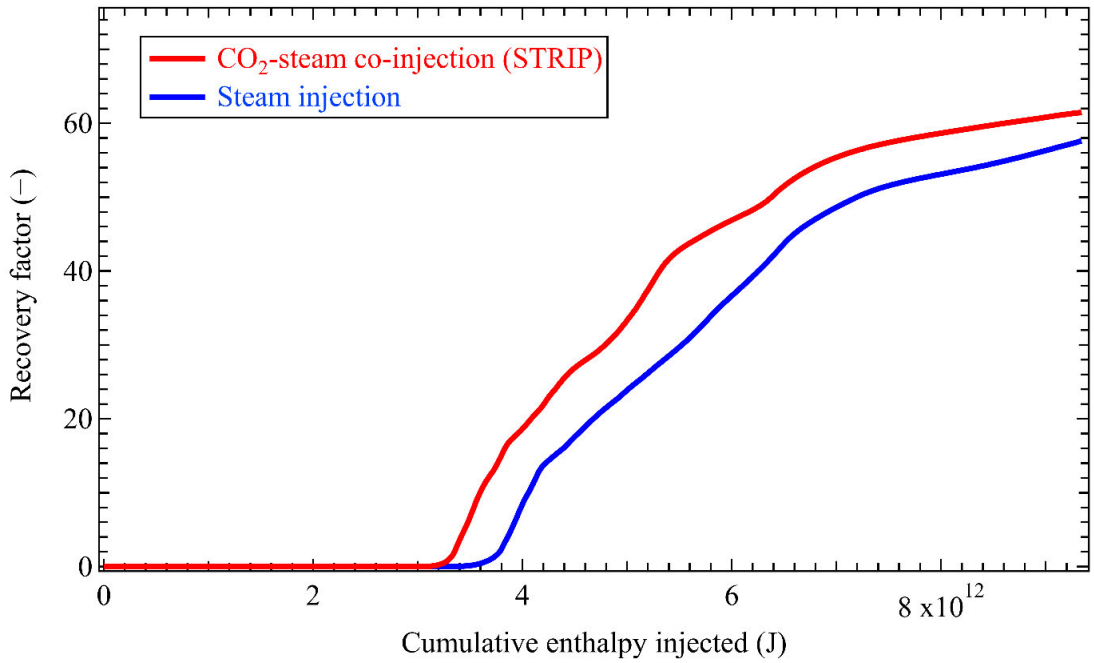

Figure 2.7. Recovery factor versus cumulative enthalpy injected for steam injection compared to STRIP.

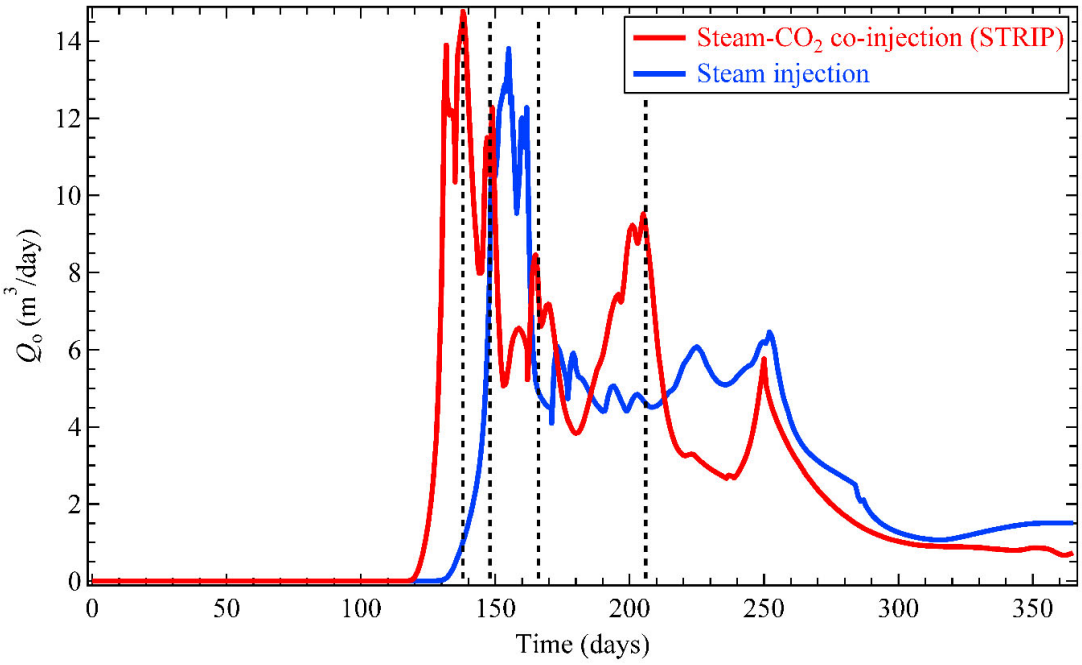

Figure 2.8. Oil production rates for steam injection compared to those from STRIP. Dashed lines indicate four oil-rate peaks.

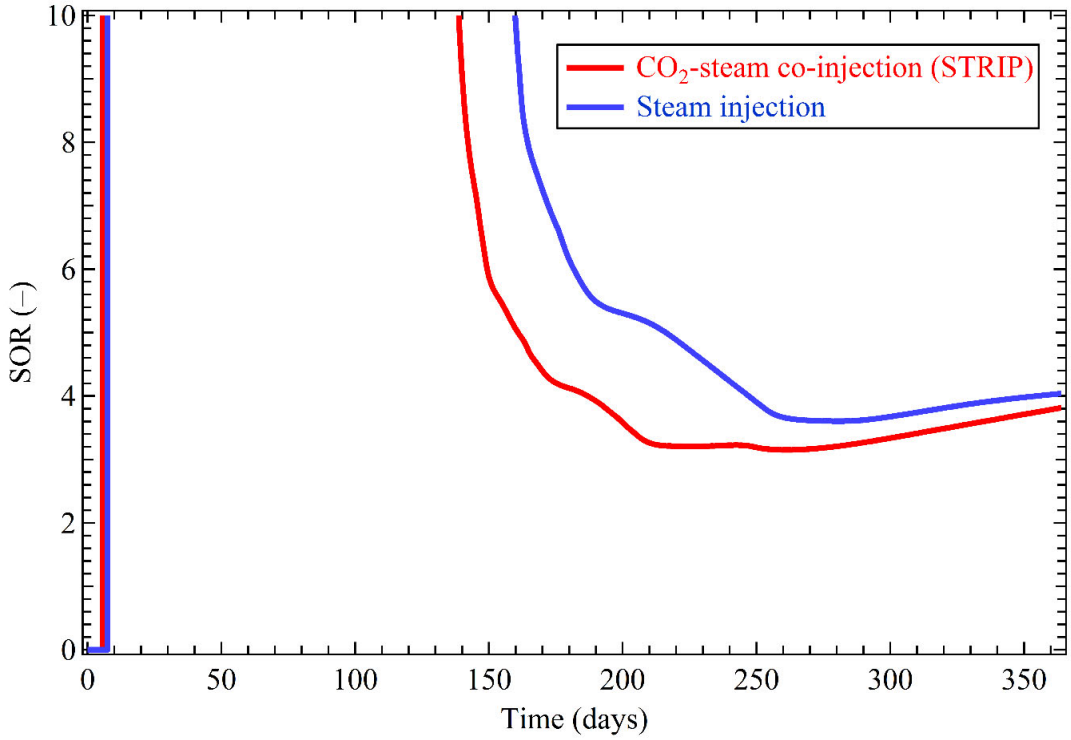

Figure 2.9. Cumulative SOR for steam injection compared to that from STRIP.

In Figure 2.7 and Figure 2.9, recovery factor and cumulative SOR of steam injection tend to approach those of STRIP at end of model run. As mentioned earlier, compared to steam injection, STRIP achieved steam breakthrough sooner. In real operations, well controls would establish steady production upon an early breakthrough of STRIP. For example, if injection and production rates were controlled (reduced) by defining maximum BHP at production wells and maximum instantaneous SOR at production wells, a low SOR would be maintained (Voskov et al. 2016). In this study, to maintain a constant injection rate and simplify the simulation framework, a high maximum BHP was defined at the injection well. Without simulating well control, the catch-up performance of steam injection was operationally related rather than process-related. In practice, STRIP will further outperform steam injection when well control is implemented.

Figure 2.10 reveals four peaks in BHP for STRIP are observed but only one for steam injection. STRIP's four BHP peaks coincide with the four oil-production-rate peaks in Figure 2.8. These multiple oil peaks indicate superior sweep efficiency and produce more oil for STRIP. What's more, the higher final (steady-state) BHP also improved sweep efficiency and reduced residual oil saturation because of the CO_2 injected into the formation.

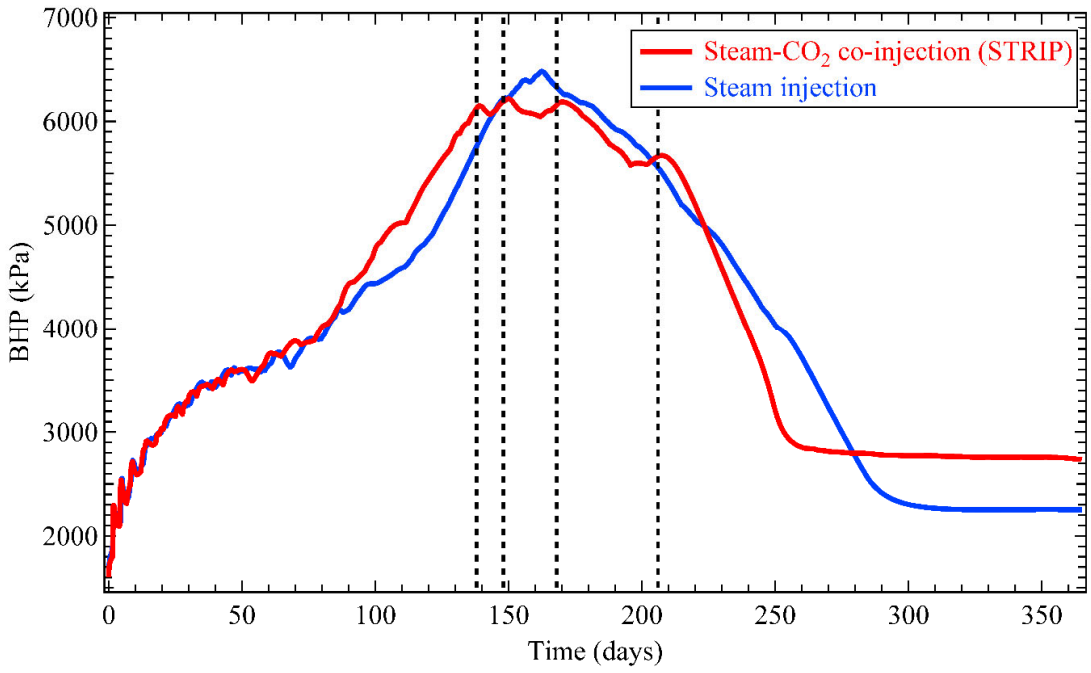

Figure 2.10. Injection well BHP for steam injection compared to that from STRIP. Dashed lines indicate four BHP peaks.

Average relative permeabilities through the entire model run were plotted and compared to the initial relative permeability curves in Figure 2.5. In the gas-fluid system (left), the relative permeability of the fluid increased while the relative permeability of the gas decreased. In the oil-water plot (right), oil relative permeability decreased at low water saturations, but increased at high water saturations while water relative permeability was increased throughout. The increased water relative permeability explains the increased water production observed for STRIP compared to steam injection (Figure 2.11). Oil cut curves for STRIP and steam injection have similar but shifted shapes (Figure 2.12). STRIP's similar oil cut with more water production than for steam injection demonstrate that STRIP produces more oil than steam injection even for equivalent energy input. Figure 2.13 compares the oil per unit area from the two models

on day 90; the CO_2-steam co-injection model reveals a more condensed oil front and higher sweep efficiency.

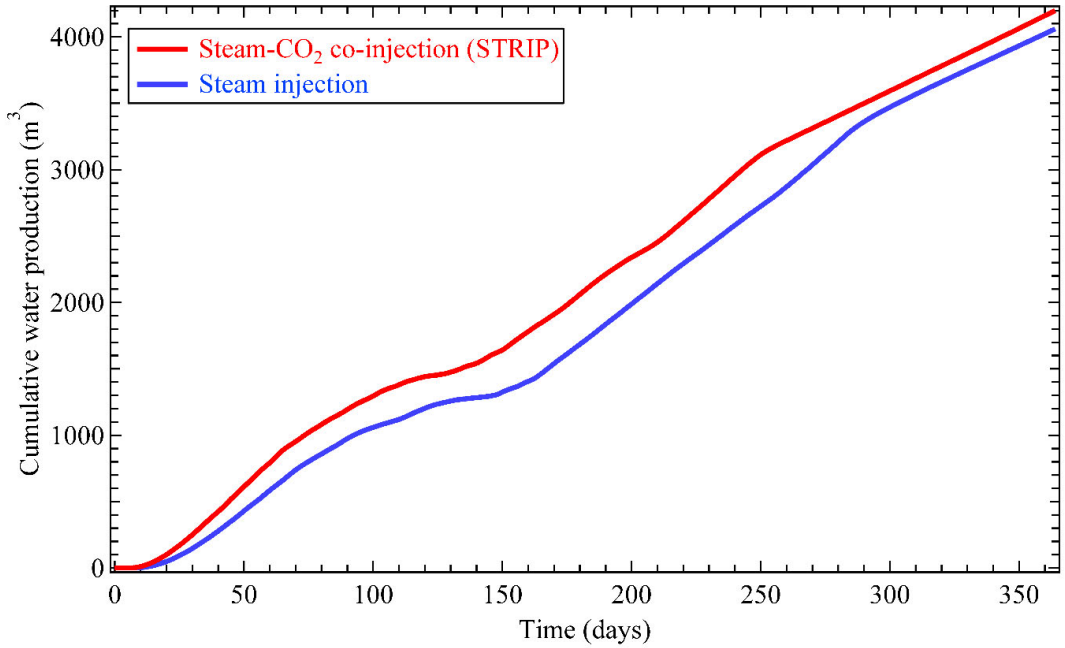

Figure 2.11. Cumulative water production for steam injection compared to that from STRIP.

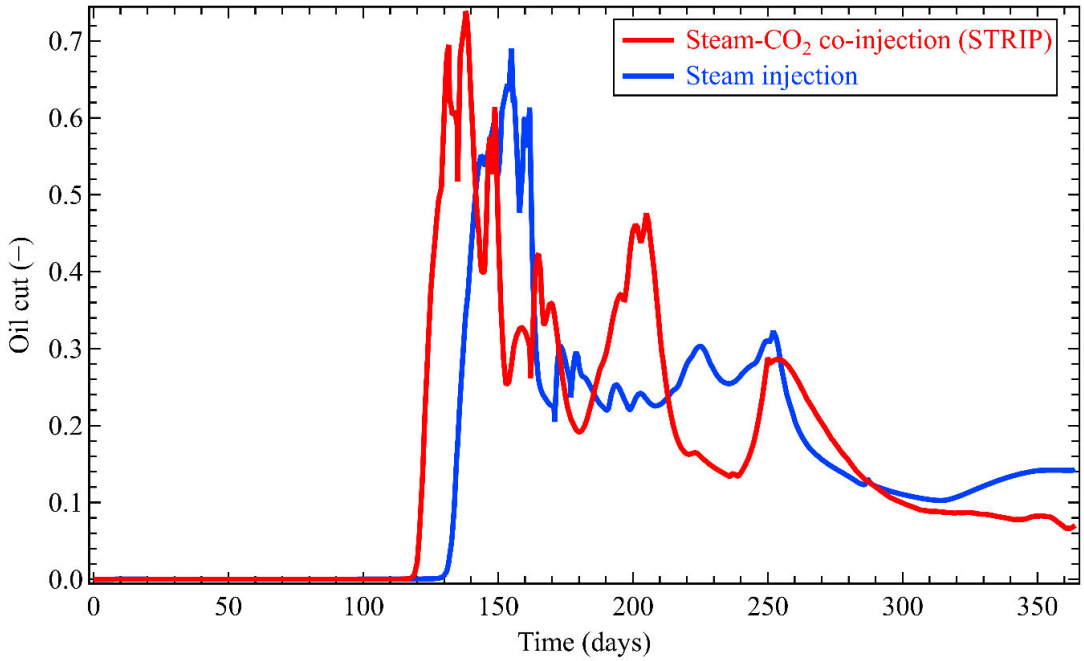

Figure 2.12. Oil cut for steam injection compared to that from STRIP.

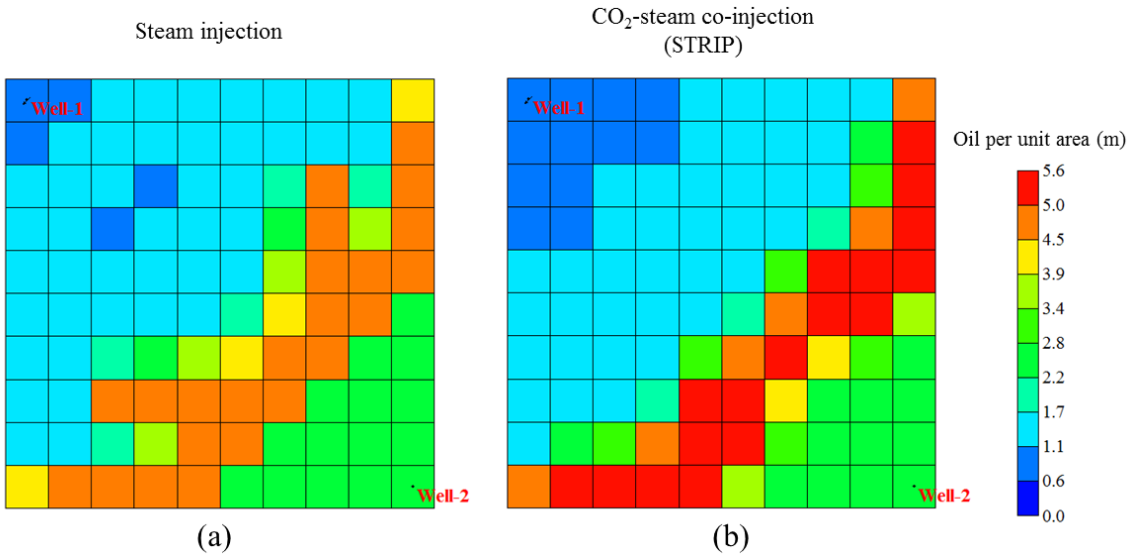

Figure 2.13. Oil per unit area on the 90th day for (a) steam injection and (b) STRIP, which demonstrates higher sweep efficiency and a condensed oil front.

Of course, there is no free lunch. The framework is much more computationally expensive, because at each time step, the framework calls PEST to do two history-matching exercises, which each require on the order of 100 GEM model runs (although these are only run for Δt days).

Conclusion and Future Works

A new framework integrating CMG STARS and GEM was built to simulate STRIP operation, conceptually similar to ES-SAGD, only more thermally and materially efficient. An inverted five-spot, quarter-symmetry model with typical heavy-oil reservoir characteristics was used for this demonstration. The framework was verified by reproducing a simple steam-injection model from STARS. In addition to the environmental advantages, the STRIP CO_2-steam co-injection process has the potential to produce more oil for the same enthalpy injected into a given reservoir. Compared with steam injection, STRIP achieved an early breakthrough, which can mitigate the early

cash-flow problems for unconventional operators. The CO_2-steam co-injection model demonstrated that solvent CO_2 plays an important role in increasing oil recovery corresponding to adjusting relative permeabilities to yield a lower SOR and increased oil produced compared to traditional steam-injection. By implementing practical well controls, STRIP will further improve performance.

Future research will focus on decreasing the computational costs and testing the framework on a larger domain. The framework called STARS, PEST (twice), and many runs of GEM each time step. As the number of payzone gridblock increases, STARS and GEM computational expenses will commensurately increase. Reducing the numbers of parameters adjusted by PEST will spare model calls and insensitive relative-permeability parameters could be fixed to affect this reduction. If the sensitivity of a parameter is lower than some user-defined limit, the parameter could be set as a constant. For example, initial investigations revealed that parameters S_{oirw}, S_{oirg}, and S_{gcon} might be fixed in the GEM-2 model for homogeneous subsurface rock properties.

Acknowledgements

The generous support of Fred Schneider, President and Chief Executive Office of RII North America Incorporated is gratefully acknowledged.

References

Aziz, K. and Settari, A. 1979. *Petroleum Reservoir Simulation*: Chapman & Hall.

Chang, Y.-B., Coats, B. K., and Nolen, J. S. 1996. A Compositional Model for Co_2 Floods Including Co_2 Solubility in Water. *SPE Res Eval & Eng* **1** (2): 155-160. SPE-35164-PA. https://doi.org/10.2118/35164-PA.

Chen, Y., Voskov, D., and Khait, M. 2018. Optimization of Co_2 Injection Using Multi-Scale Reconstruction of Compositional Transport. *Proc.,* ECMOR XVI-16th European Conference on the Mathematics of Oil Recovery, Barcelona, Spain, 3–6 September. https://doi.org/10.3997/2214-4609.201802240.

Chow, L. and Butler, R. 1996. Numerical Simulation of the Steam-Assisted Gravity Drainage Process (Sagd). *Journal of Canadian Petroleum Technology* **35** (06): 9. PETSOC-96-06-06. https://doi.org/10.2118/96-06-06.

CMG. 2015a. Cmg Gem User's Guide.

CMG. 2015b. Cmg Stars User's Guide.

CMG. 2015c. Cmg Winprop User's Guide.

Collins, D. A., Nghiem, L. X., Li, Y. K. et al. 1992. An Efficient Approach to Adaptive-Implicit Compositional Simulation with an Equation of State. *SPE Journal* **7** (02): 395-401. SPE-15133-PA. https://doi.org/10.2118/15133-PA.

Cyr, T., Coates, R., and Polikar, M. 2001. Steam-Assisted Gravity Drainage Heavy Oil Recovery Process; International (PCT) Patent No. 6,257,334.

Dhima, A., de Hemptinne, J.-C., and Jose, J. 1999. Solubility of Hydrocarbons and Co2 Mixtures in Water under High Pressure. *Industrial & engineering chemistry research* **38** (8): 3144-3161. https://doi.org/10.1021/ie980768g.

Doherty, J. E. 2016a. Model-Independent Parameter Estimation User Manual Part I: Pest, Sensan and Global Optimisers, PEST Manual, Watermark Numerical Computing, Brisbane, Australia.

Doherty, J. E. 2016b. Model-Independent Parameter Estimation User Manual Part Ii: Pest Utility Support Software, PEST Addendum, Watermark Numerical Computing, Brisbane, Australia.

Ertekin, T., Abou-Kassen, J. H., and King, G. R. 2001. *Basic Applied Reservoir Simulations*: Society of Petroleum Engineers.

Ganapathy, C. and Voskov, D. V. 2018. Multiscale Reconstruction in Physics for Compositional Simulation. *Journal of Computational Physics* **375**: 747-762. https://doi.org/10.1016/j.jcp.2018.08.046.

Harvey, A. H. 1996. Semiempirical Correlation for Henry's Constants over Large Temperature Ranges. *AIChE Journal* **42** (5): 1491-1494. https://doi.org/10.1002/aic.690420531.

Hassanzadeh, H., Pooladi-Darvish, M., Elsharkawy, A. M. et al. 2008. Predicting Pvt Data for Co2–Brine Mixtures for Black-Oil Simulation of Co2 Geological Storage. *International Journal of Greenhouse Gas Control* **2** (1): 65-77. https://doi.org/10.1016/S1750-5836(07)00010-2.

Hecht, E. S., Shaddix, C. R., Houf, W. G. et al. 2011. Evaluation of Light-Off Limits for a Novel Oxy-Combustion Process for Advanced Eor, Sandia National Lab.

Heidari, M. 2014. *Equation of State Based Thermal Compositional Reservoir Simulator for Hybrid Solvent/Thermal Processes*. PhD, University of Calgary, Calgary, Alberta, Canada.

Hill, R. W., Dewey, F. S., and Thorsness, C. B. 1985. Silane-Propane Ignitor/Burner. USA Patent Application No. 498,438; International (PCT) Patent No. 4,499,945.

James, S. C., Moore, K., Muuray, D. et al. 2014. Rii Na's Strip Technology Pilot Project: Progress Report, 1206940.000 2746, E^{x}ponent, Inc., Irvine, CA.

James, S. C., Murray, D., Caffaro, L. et al. 2015. Rii Na's Strip Technology Pilot Project: Summary Report, Baylor University, Waco, TX.

James, S. C., Shaddix, C. R., Hecht, E. S. et al. 2012. Solvent Thermal Resource Innovations Process (Strip) Research and Development Report, E^{x}ponent Inc., Irvine, CA.

Khait, M., Voskov, D., and Konidala, G. 2018. Tie-Simplex Parametrization for Operator-Based Linearization for Non-Isothermal Multiphase Compositional Flow in Porous. *Proc.,* ECMOR XVI-16th European Conference on the Mathematics of Oil Recovery, Barcelona, 3-6 September. https://doi.org/10.3997/2214-4609.201802183.

Kondo, S., Tokuhashi, K., Nagai, H. et al. 1994. Experimental Study of Spontaneous Ignition Limit of Oxygen-Lean Silane Mixtures. *Combustion and Flame* **97** (3): 296-300. https://doi.org/10.1016/0010-2180(94)90022-1.

Kondo, S., Tokuhashi, K., Nagai, H. et al. 1995. Spontaneous Ignition Limits of Silane and Phosphine. *Combustion and Flame* **101** (1–2): 170-174. https://doi.org/10.1016/0010-2180(94)00175-R.

Lake, L. W. 1989. *Enhanced Oil Recovery*: Prentice Hall.

Lucia, A. 2010. A Multiscale Gibbs-Helmholtz Constrained Cubic Equation of State. *Journal of Thermodynamics* **2010**. http://dx.doi.org/10.1155/2010/238365.

Lucia, A. and Bonk, B. M. 2012. Molecular Geometry Effects and the Gibbs–Helmholtz Constrained Equation of State. *Computers & Chemical Engineering* **37**: 1-14. https://doi.org/10.1016/j.compchemeng.2011.08.006.

Lucia, A., Bonk, B. M., Waterman, R. R. et al. 2012. A Multi-Scale Framework for Multi-Phase Equilibrium Flash. *Computers & Chemical Engineering* **36**: 79-98. https://doi.org/10.1016/j.compchemeng.2011.07.011.

Maini, B. B. 1999. Foamy Oil Flow in Primary Production of Heavy Oil under Solution Gas Drive. *Proc.,* SPE Annual Technical Conference and Exhibition, Houston, TX. SPE-56541-MS. https://doi.org/10.2118/56541-MS.

Mifflin, R., Watts, J., and Weiser, A. 1991. A Fully Coupled, Fully Implicit Reservoir Simulator for Thermal and Other Complex Reservoir Processes. Presented at the SPE Symposium on Reservoir Simulation, Anaheim, California. 17–20 February. SPE-21252-MS. https://doi.org/10.2118/21252-MS.

Moore, C. and Doherty, J. 2005. Role of the Calibration Process in Reducing Model Predictive Error. *Water Resources Research* **41** (5). https://doi.org/10.1029/2004WR003501.

Nourozieh, H., Kariznovi, M., and Abedi, J. 2012. Development and Evaluation of a Modified Experimental Apparatus for Phase Behavior Study of Solvent–Heavy Crude Systems. *Fuel processing technology* **102**: 116-123. https://doi.org/10.1016/j.fuproc.2012.04.032.

Orr, F. M. 2007. *Theory of Gas Injection Processes*, Vol. 5. Copenhagen, Denmark: Tie-Line Publications.

Pedersen, K. S. and Fredenslund, A. 1987. An Improved Corresponding States Model for the Prediction of Oil and Gas Viscosities and Thermal Conductivities. *Chemical Engineering Science* **42** (1): 182-186. https://doi.org/10.1016/0009-2509(87)80225-7.

Petroleum Technology Alliance Canada. 2005. Ptac Knowledge Centre: Upstream Oil and Gas Energy Efficiency, Petroleum Technology Alliance Canada, Calgary, Alberta, Canada.

Rannou, G., Voskov, D., and Tchelepi, H. A. 2013. Tie-Line-Based K-Value Method for Compositional Simulation. *SPE Journal* **16** (06): 1112-1122. PETSOC-96-06-06. https://doi.org/10.2118/167257-PA.

Robinson, D. B. and Peng, D. 1978. *The Characterization of the Heptanes and Heavier Fractions for the Gpa Peng-Robinson Programs*. Tulsa, Okla.: Gas Processors Association.

Rubin, B. and Buchanan, W. L. 1985. A General Purpose Thermal Model. *SPE Journal* **25** (02): 202-214. SPE-11713-PA. https://doi.org/10.2118/11713-PA.

Saner, W. and Patton, J. 1986. Co2 Recovery of Heavy Oil: Wilmington Field Test. *Journal of Petroleum Technology* **38** (07): 769-776. SPE-12082-PA. https://doi.org/10.2118/12082-PA.

Schneider, F. and Owens, W. 1976. Relative Permeability Studies of Gas-Water Flow Following Solvent Injection in Carbonate Rocks. *SPE Journal* **16** (01): 23-30. SPE-5554-PA. https://doi.org/10.2118/5554-PA.

Sigmund, P. M. 1976. Prediction of Molecular Diffusion at Reservoir Conditions. Part 1-Measurement and Prediction of Binary Dense Gas Diffusion Coefficients. *Journal of Canadian Petroleum Technology* **15** (02). PETSOC-76-02-05. https://doi.org/10.2118/76-02-05.

Tharanivasan, A. K., Yang, C., and Gu, Y. 2006. Measurements of Molecular Diffusion Coefficients of Carbon Dioxide, Methane, and Propane in Heavy Oil under Reservoir Conditions. *Energy & fuels* **20** (6): 2509-2517. https://doi.org/10.1021/ef060080d.

Van-Quy, N., Simandoux, P., and Corteville, J. 1972. A Numerical Study of Diphasic Multicomponent Flow. *SPE Journal* **12** (02): 14. SPE-3006-PA. https://doi.org/10.2118/3006-PA.

Varavei, A. and Sepehrnoori, K. 2009. An Eos-Based Compositional Thermal Reservoir Simulator. Presented at the SPE Reservoir Simulation Symposium, Woodlands, Texas. 2–4 February. SPE-119154-MS. https://doi.org/10.2118/119154-MS.

Voskov, D., Zaydullin, R., and Lucia, A. 2016. Heavy Oil Recovery Efficiency Using Sagd, Sagd with Propane Co-Injection and Strip-Sagd. *Computers & Chemical Engineering* **88**: 115-125. http://dx.doi.org/10.1016/j.compchemeng.2016.02.010.

Voskov, D. V. 2017. Operator-Based Linearization Approach for Modeling of Multiphase Multi-Component Flow in Porous Media. *Journal of Computational Physics* **337**: 275-288. http://dx.doi.org/10.1016/j.jcp.2017.02.041.

Weijermars, R. 2011. Credit Ratings and Cash-Flow Analysis of Oil and Gas Companies: Competitive Disadavantage in Financing Costs for Smaller Companies in Tight Capital Markets. *SPE Economics & Management* **3** (02): 54-67. https://doi.org/10.2118/144489-PA.

Young, L. C. and Stephenson, R. E. 1983. A Generalized Compositional Approach for Reservoir Simulation. *SPE Journal* **23** (05): 727-742. SPE-10516-PA. https://doi.org/10.2118/10516-PA.

Zaydullin, R., Voskov, D., and Tchelepi, H. 2017. Comparison of Eos-Based and K-Values-Based Methods for Three-Phase Thermal Simulation. *Transport in Porous Media* **116** (2): 663-686. https://doi.org/10.1007/s11242-016-0795-7.

CHAPTER THREE

Vuggy Facies Identification from Borehole Images Using a Convolutional Neural Network

This chapter prepared as: Jiang, J., Xu, R., James, S.C., Xu, C. Vuggy Facies Identification from Borehole Images Using a Convolutional Neural Network, *SPE Reservoir Evaluation & Engineering*.

Abstract

Identification of vuggy intervals and understanding their connectivity are critical for predicting carbonate reservoir performance. Although core samples and conventional well logs have been traditionally used to classify vuggy facies, this process is labor intensive and often suffers from data inadequacies. Recently, Convolutional Neural Network (CNN) algorithms have approached human-level performance at multi-image classification and identification tasks. In this study, CNNs were trained to identify vuggy facies from a well in the Arbuckle Group in Kansas. Borehole resistivity images were pre-processed into half-foot intervals; this complete dataset was culled by removing poor-quality images to generate a cleaned dataset for comparison. Core descriptions along with conventional gamma ray, neutron/density porosity, photoelectric factor, and nuclear magnetic resonance T2 data were used to label these datasets for supervised learning. Hyperparameters defining the CNN network architecture (numbers of convolutional layers and filters and the numbers of dense layers and neurons) and minimize overfitting (dropout rates, patience, and minimum delta) were optimized. The median losses and accuracies from five Monte Carlo realizations of each hyperparameter combination were the metrics defining CNN performance. After hyperparameter optimization, median

accuracy for vuggy/non-vuggy facies classification was 0.847 for the cleaned dataset (0.813 for the complete dataset). This study demonstrated the effectiveness of using microrestivity image logs in a CNN to classify facies as either vuggy or non-vuggy, while highlighting the importance of data quality control. Moreover, this effort lays the foundation for developing CNNs to segment images to estimate vuggy porosity.

Introduction

Unlike clastic reservoirs, carbonate reservoirs typically have poor porosity-permeability correlations due to the presence of vugs and fractures. Vugs were defined as non-fabric selective secondary solution pores by Choquette and Pray (1970). Another important study defined vugs as pore spaces significantly larger than particles (Lucia 1983, Lucia 1995). For reservoir characterization, the debate continues as to which definition is superior (Lucia 1983, Lucia 1995, Lønøy 2006). Regardless of which definition you prefer, this study developed a method for identifying vuggy intervals from image data, not a new carbonate porosity-classification system. Here, vugs are simply defined as solution-enlarged cavities in rock. Depositional pores as well as cracks formed during tectonism may be enlarged by secondary diagenetic processes such as dissolution to form grain- to fist-sized or larger vugs.

Vuggy intervals can be difficult to identify on conventional wireline logs because these logs lack dimensional resolution; vugs are 3D features and wireline data are 1D (Cunningham et al. 2004, Ausbrooks et al. 1999, Newberry et al. 1996). Identification of vuggy intervals and understanding their connectivity are critical for predicting reservoir performance. Intervals with isolated vugs may yield a high neutron-log porosity signal,

yet they produce less oil than intervals with lower neutron-log porosity and more connectivity.

Vug identification is traditionally a labor-intensive process requiring acquisition of subsurface core for experienced geologists to describe the geologic facies and pore-types. Lucia (1983) summarized a general process for geologists to identify vugs from cores: (1) recognize interparticle pore space; (2) visually estimate particle size; and (3) visually recognize vuggy porosity. Recently, nuclear magnetic resonance (NMR), micro-computed tomography, and computed tomography were used to identify vugs in carbonates with fine particles (e.g., clay-silt particles) and then to quantify vuggy porosity (Li et al. 2017, Vik et al. 2007, Doveton and Watney 2014). Traditional core descriptions, NMR, and tomography measurements are important inputs for geologic modeling and reservoir simulation. However, these techniques are limited by the availability of cores. Therefore, tools and workflows for identifying vugs from subsurface log data are needed to act as surrogates for core-based descriptions.

Microresistivity imaging logs support identification of vuggy intervals and can potentially be used as proxies for core-based vug identification. Unlike conventional wireline logs, microresistivity logs provide a higher degree of geologically relevant information using images from the sidewall of a borehole from which reservoir properties can be inferred including lithology, grain-size, bedding and dip angles, fracture orientations, and pore-types. Interpretation of image logs can be time-consuming and heavily dependent upon the experience of the interpreter. In this study, we developed a method for rapid interpretation of vuggy intervals from image logs so that vug identification can be extended to wells without cores.

Microresistivity logs are a type of unstructured data (images that are not organized in a pre-defined model) generated by indirect electrical measurements of the surrounding rock formations in a borehole. These unstructured data can be interpreted using computer-assisted object detection and image classification.

Newberry et al. (1996) proposed an analytical method using the classic Archie saturation equation to compute porosity distributions from resistivity image logs. Cunningham et al. (2004) applied filters and pixel counts to quantify vuggy porosity from optical image logs. A geostatistical approach has been used to generate porosities from images logs to achieve reliable matches to core plug measurements (Tilke et al. 2006). Igneous lithology classification from image logs was undertaken using feature engineering and principal component analysis (Jungmann et al. 2011). However, in each of these studies, challenges remained when assessing geologic information. Even though image logs provide more and different information from conventional logs, there may be significant data insufficiency. In other words, unlike color images with the three RGB channels, data collected by resistivity image-logging tools are single-channel images. Previous quantitative studies only focused on classification through pixel counts for rocks with limited heterogeneity with features that could be easily distinguished. For example, Newberry et al. (1996) and Cunningham et al. (2004) used dark pixels (high resistivity responses) to identify vugs in shales and carbonate formations without fractures, but dark pixels in image logs are non-unique and can also indicate vugs, fractures, shales, cherty layers, etc. As a result, these approaches are limited to fairly homogeneous materials.

Machine learning (ML) has proven to be a powerful tool for identification of geologic features from unstructured data (Lary et al. 2016, Bergen et al. 2019, Xu et al.

2019, James et al. 2018). Among ML algorithms, a convolutional neural network (CNN) was selected because of successful applications to computer-vision problems (Krizhevsky et al. 2012, Kalchbrenner et al. 2014, LeCun et al. 2015). Moreover, CNNs have been successfully applied to geoscientific image classification in mineralogy, seismic, and remote-sensing studies (Jobe et al. 2018, Hu et al. 2015, Xu et al. 2019, Wu et al. 2019). This study identified vuggy intervals by applying a CNN to borehole-resistivity image logs.

Geologic Background

This study focused on the Arbuckle Group shown in gray in Figure 3.1, which appears throughout Kansas and ranges from 150 to 1500 m thick (Keroher and Kirby 1948, Cole 1975). The current conceptual model of the Arbuckle Group is based on early petroleum well drillings (1917–1940); however, they only penetrated shallow portions of the formation (3 to 15 m) and provided low-quality logging data that do not meet modern standards (Franseen and Byrnes 2012). In recent decades, deep wells with modern logging data became available for Arbuckle Group rocks, but most wells lack core correlation. What's more, the dearth of equivalent strata and a biostratigraphic framework precludes a complete understanding of the Arbuckle Group. As a target, especially for gas production, the Arbuckle Group needs more study to appraise its production potential.

The Arbuckle Group is part of the Cambrian-Ordovician Great American Carbonate Bank, which ranges from the north flank to the south of the North American Craton (Wilson et al. 1991). During the Cambrian to Ordovician, Kansas was located 20 to 30° south of the equator and south of the Transcontinental Arch (Ross Jr 1976).

Shallow marine limestone was deposited north of the Transcontinental Arch with cherty dolomite and dolomitic limestone in the north (Ross Jr 1976). Sea levels started to fall at the end of the early Ordovician and exposed Cambrian-Ordovician-deposited carbonates. A series of uplifts in the early Pennsylvanian, especially the Nemaha and Central Kansas uplifts, intensified erosion and uneven paleotopography of these carbonates (thickness contours in Figure 3.1). Another significant event induced by uplift and erosion yielded an unconformity between the Arbuckle Group and overlying Simpson Group. Structural-stratigraphic traps developed with karstic fractures that enhanced porosity on the tops of these paleohighs (Adler et al. 1971, Walters 1958, Franseen and Byrnes 2012).

The Arbuckle Group is mainly composed of shallow-water ramp-type subtidal to peritidal carbonates (Franseen 1994, 2000, Franseen et al. 2004, Franseen and Byrnes 2012, Steinhauff et al. 1998). Different scales of subtidal to peritidal cycles (<3 ft to >20 ft) controlled the distribution of depositional facies and increased the vertical heterogeneity of the Arbuckle formation (Franseen 2000, Steinhauff et al. 1998). Furthermore, the vertical heterogeneity (packing of thin layers) complicates labelling and identification of facies intervals. Historically, most oil and gas reservoirs were only found in the top 25–50 ft of the Arbuckle formation, suggesting that it was a karstic fracture-controlled reservoir with a short oil column (Adler et al. 1971). Later studies revealed remarkable matrix porosity in the deeper unkarsted carbonates indicating the potential for oil reserves in these strata (Franseen and Byrnes 2012).

Data used in this study were from the Wellington KGS 1-32 well (location indicated in Figure 3.1) and include borehole images, conventional and nuclear magnetic resonance (NMR/NMR-T2) log data, as well as core descriptions. In addition, gamma ray

(GRTC), resistivity (RT-10, -20, -30, -60, and -90), neutron/density porosity (NPHI, RHOB), and photoelectric factor (PEF) wireline logs were collected. Figure 3.2 shows the stratigraphic column of Wellington KGS 1-32 (Franseen and Byrnes 2012). Diagenesis including dolomitization, dissolution and karsting, fracturing, and hydrothermal alteration have added complexity to the lithologies. The dataset (2,695 ft of images) covers the Cambrian-Ordovician Arbuckle Group as well as the overburden Simpson Group and underburden Precambrian igneous formations. The well was chosen because it has a full-spectrum data set covering most well-log data types.

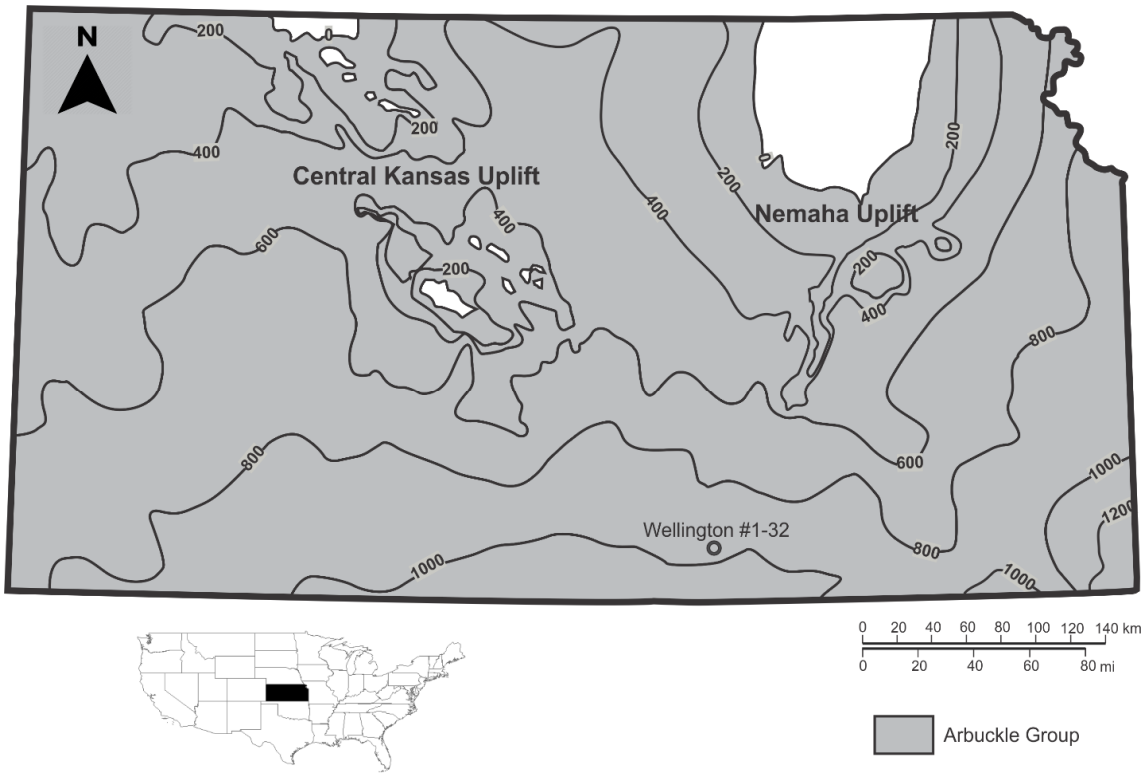

Figure 3.1. Location of Wellington #1–32 and isopach map of the Kansas Arbuckle Group, which is thicker in southeastern Kansas and absent in the white area. Contours were modified from Cole (1975).

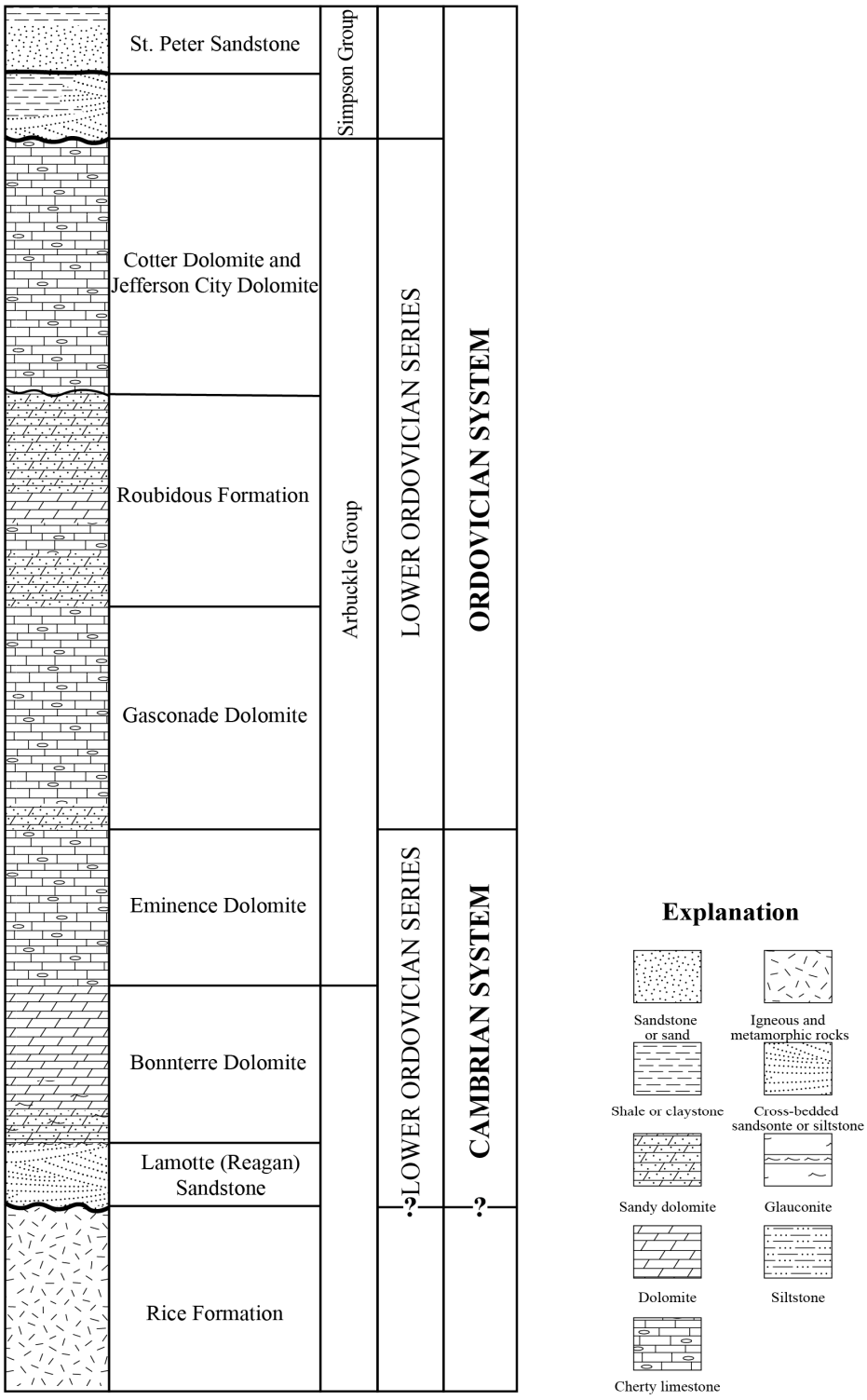

Figure 3.2. Stratigraphic chart for the Arbuckle Group and adjacent formations (modified from Franseen and Byrnes, 2012).The lithologic patterns were from USGS (2006). Cambrian-Ordovician Arbuckle Group rocks are mainly composed of shallow-water subtidal to peritidal carbonates.

The lithologies present in Wellington KGS 1-32 include sandstone, shale, limestone, dolomite, cherty limestone, and granite. The Arbuckle Group experienced non-destructive dolomitization, so the original texture of the depositional facies was maintained. Previous studies identified eight dominant depositional facies in the Arbuckle Group: clotted algal boundstone, laminated algal boundstone, peloidal packstone-grainstone, mixed packstone-grainstone, ooid packstone-grainstone, wackestone-mudstone, intra-Arbuckle shale, and conglomerate and breccia (Steinhauff et al. 1998, Franseen and Byrnes 2012).

Methods

Figure 3.3 shows the workflow for this study. Preprocessing took about 50% of the time and effort due to the various data types and complicated data pre-processing. Training took about 30% of the time because the CNNs used in this study were relatively small. Post-processing took about 20% of the time.

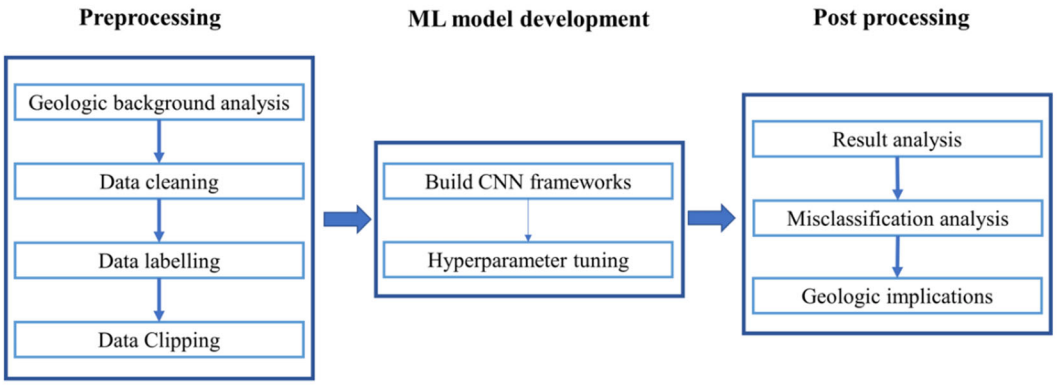

Figure 3.3. Workflow for this study.

Data Quality

Image logs were visualized with Schlumberger's Techlog 2019.1. The data were pre-processed to harmonize them such that they were all properly correlated with depths (depth correction). Image log pixel values ranged from 0 to 255 and were plotted with a white-yellow-black color scheme (see Figure 3.4) where high-resistivity responses are represented by yellow-white colors and low-resistivity by brown-black.

A typical resistivity image-logging tool has 4, 6, or 8 pads that are pressed against the borehole side wall. Electrical currents are forced into the rock through electric node arrays on the pads. Geologic features can be identified by different resistivity responses received by the tool. Inadequate contact between the pads and the side wall (e.g., due to sidewall collapse, the presence of low-resistivity brine, or vugs larger than the pads) can yield low-quality data (add reference).

A data-quality check revealed three types of poor-quality images (Figure 3.4): (1) over-saturated image logs (e.g., false high-resistivity measurements due to loss of pad contact with the sidewall) that do not reveal any information (Figure 3.4(a)); (2) improper function of the logging tool (e.g., pad slippage) generated elongated striping (Figure 3.4(b)); and (3) malfunction of at least one pad leading to partial information loss (Figure 3.4(c)). Removing these poor-quality images from the training data set should provide a more robust CNN model and boost prediction accuracies. However, the ultimate goal of ML is full automation (i.e., the ML algorithm should have the capability to process even poor-quality-images). In this study, CNN models were trained using both the complete dataset and the cleaned dataset with poor-quality images removed and

accuracies were compared. The 3rd type was not removed in the cleaned dataset because it still contains considerably useful information.

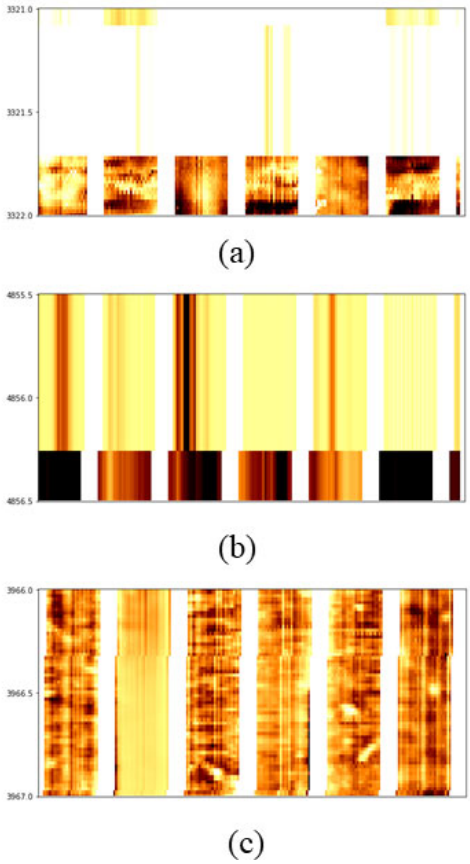

Figure 3.4. (a) Image log too bright to reveal any information; (b) image logs shows elongated features and loss of vertical resolution; (c) malfunction of pad two of six.

Data Labelling

Binary vuggy/non-vuggy facies were manually classified using gamma ray (GRTC), resistivity (RT10, RT20, RT30, RT60, and RT90), neutron/density porosity (NPHI, RHOB), photoelectric factor (PEF), core descriptions, and NMR T2. During facies labeling, there were several challenges that had to be addressed. For example, from 3168 to 3186 ft, the high gamma ray, low NMR T2, and low resistivity implied a possible shale section (outlined in turquoise in Figure 3.5). The image column in this region

indicates shale interbedded with carbonate and this was labeled as non-vuggy although this was a more qualitative assessment and a judgment call by the geologist.

Figure 3.6 (a) and (d) show image logs with corresponding NMR T2 and core photos for non-vuggy facies, whereas (b) and (c) are vuggy facies. Another issue was related to identifying black strips or laminae. Previous studies have used simple pixel counts on image logs to measure vug-porosity and gamma-ray cutoff to identify shale, which has low resistivity and is represented by darker colors (Ausbrooks et al. 1999). Due to the lower resistivity of shale, a resistivity threshold was used to label shale pixels in image logs. But this approach is not possible here because of the inability to distinguish low-resistivity chert and horizontal fractures from shale. In Figure 3.6 (a) and (c), the cherty layers have similar resistivities (layers of dark colors) to shale layers. A third issue was that the neutron-density logs sometimes contradicted the NMR T2 distributions, which are the transverse relaxations times that are proportional to pore-throat radii. Finally, both vuggy facies and fractures had NMR T2 distributions with peaks at longer times (Figure 3.6). Longer NMR T2 times indicate larger pores, but these data alone do not provide enough information to distinguish pore types (vugs or fractures, e.g., Figure 3.6 (b) and (d)). These challenges highlight the importance of using diverse data types for facies labeling.

Recall the data quality issues mentioned earlier, the data-quality indices were labelled based on image data only. The first and second types of image with poor quality were label as bad (0) and rest images are good (1).

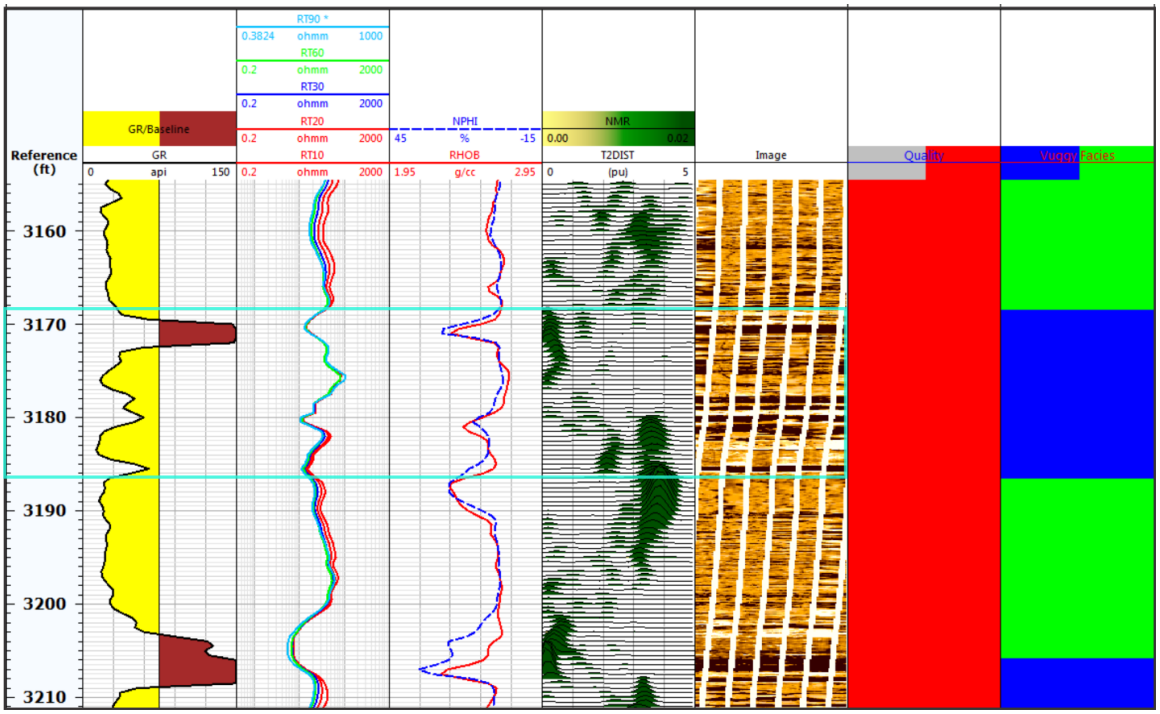

Figure 3.5. Wireline data (GRTC, RT-10, -20, -30, -60, -90, NPHI, RHOB, PEF, and NMR T2) used for labeling vuggy facies.

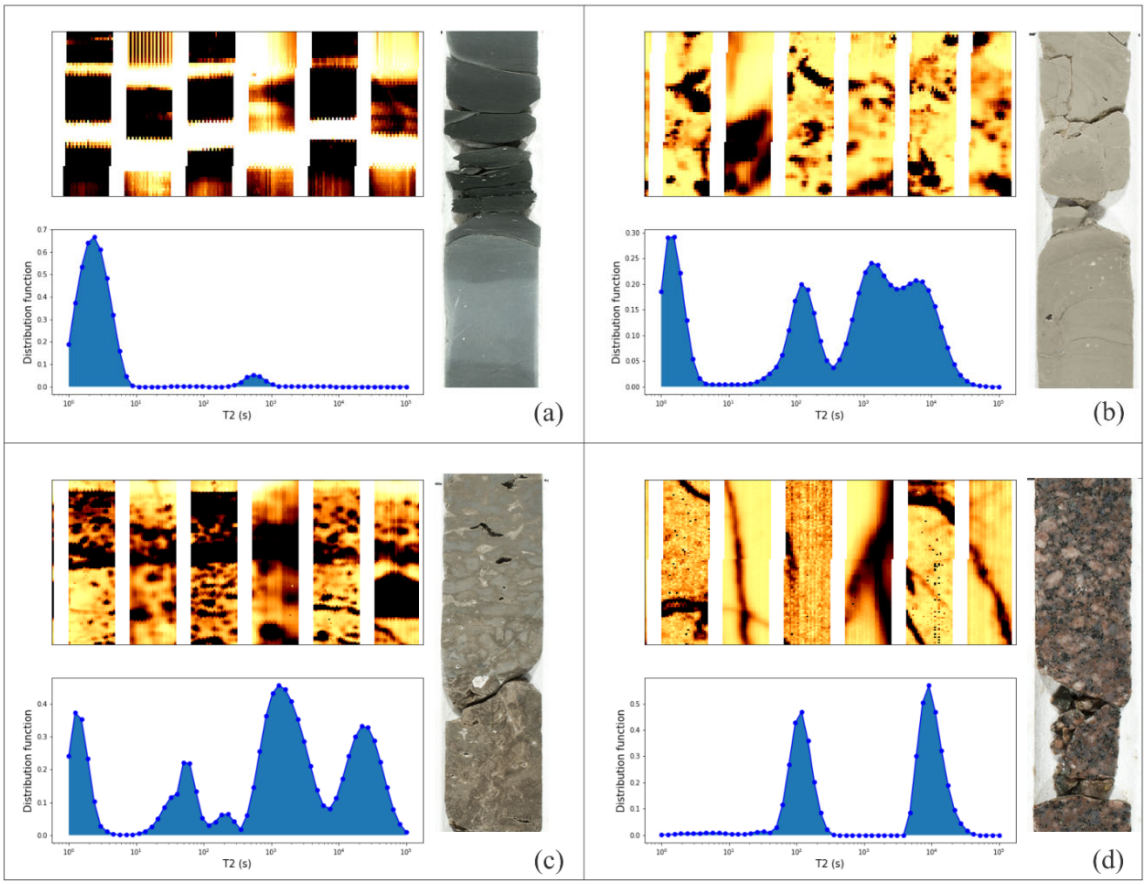

Figure 3.6. Images for (a) shale, (b) dolomite, (c) dolomite with chert, and (d) granite with corresponding average NMR T2 distributions and core photos. Clear large T2 distributions are apparent in both vuggy facies and fractured rocks. Here, NMR T2 averages comprise four quarter-foot intervals over the one-foot image.

Data Clipping

A Python script divided the single-well borehole image log into multiple smaller images with a user-defined number of pixels. A moving window sequentially scanned the image and saved each scan as an input sample (no overlap) for CNN training and testing. The image log was divided into 60×200-pixel samples in depth and width, respectively, representing half-foot intervals. To accommodate feature map reduction (discussed later), each sample was zero padded to a size of 64×208. The resulting 5355 samples with corresponding facies labels were split into training/validation/test datasets in a ratio of

0.8/0.1/0.1 (Table 3.1). A total of 199 samples (3.7%) were identified as images with poor quality. Cleaned datasets included the same samples from the previous split but removed those images with poor quality. Note that stratification (ensuring that the ratio of vuggy to non-vuggy facies was consistent in the training/validation/test datasets) was not necessary because the ratio of vuggy to non-vuggy facies was close to 1 (0.82).

Table 3.1. Number of samples comprising the complete and cleaned datasets.

Dataset name	Complete datasets	Cleaned datasets
Training	4285	4129
Validation	535	516
Test	535	511

CNN Framework

CNNs have been used in computer vision for decades (LeCun and Bengio 1995, Krizhevsky et al. 2012, Kalchbrenner et al. 2014) and successful implementation on powerful graphical processing units (GPUs) combined with ever-increasing availability of training data has increased the popularity of CNNs (Russakovsky et al. 2015, LeCun et al. 2015). Today, CNNs are also used for natural language processing, hyperspectral image processing, and medical information analyses (Lee and Kwon 2017, Chen et al. 2017, Yamashita et al. 2018).

CNNs typically comprise three types of layers: convolutional, pooling, and fully connected layers. Convolutional layers are the primary building blocks for CNNs; they apply filters to the upstream input data to generate feature maps that identify and classify local features. An image comprising one (e.g., grayscale) or more (e.g., RGB) two-

dimensional arrays are output. An output tensor from a convolutional layer is calculated as:

$$\mathbf{A}_j = f\left(\sum_{i=1}^{N} \mathbf{I}_i * \mathrm{K}_j + B_j\right) \qquad j = 1,\mathrm{K}\ J. \tag{0.18}$$

In the preceding equation, input tensor, $\mathbf{I}_i$ (one of N channels of an image or a feature map), is convoluted ($*$) with filter $\mathbf{K}_j$. These convoluted tensors are summed and bias, B_j, is added to produce the total input to the nonlinear activation function, f. This activation function is applied to each element of all input channels, thereby yielding output tensor $\mathbf{A}_j$. Output tensors calculated from J filters are then assembled into a 3D tensor. The goal when training a CNN is to update the values of each filter that determine the local features that optimize image classification.

To progressively reduce the size of the feature maps and speed computation, convolutional layers are followed by pooling layers. The most common pooling layer, max pooling, reduces array size of the feature maps (outputs from convolutional layers) by selecting only the maximum value from a block with a user-defined size (e.g., a 2 × 2 kernel size):

$$\mathbf{A}_j^l = \max_s\left(\mathbf{A}_j^{l-1}\right). \tag{0.19}$$

Here, maxs extracts the maximum values from the output of the previous convolutional layer ($\mathbf{A}_j^{1-1}$) from each distinct $s \times s$ pooling block. The resulting number of elements from each output tensor are s^2 times smaller than the input, but the total number of output tensors remains unchanged.

After several sets of convolutional layers and pooling layers, CNNs are usually finalized through several fully connected (FC) layers and an output layer. The output 3D feature maps (**A**) from convolutional layers are unrolled into vector **h**. The FC layers calculate:

$$\mathbf{z} = \sigma\left(\mathbf{w} \cdot \mathbf{h} + b_{\mathrm{f}}\right), \tag{0.20}$$

where **z** is the output from the FC layer, **w** is the weight vector applied to the FC layer, σ is a nonlinear activation function, and b_{f} is the bias for the FC layer. Finally, predictions are made from the output layer:

$$\hat{\mathbf{y}} = S\left(\mathbf{w}_{\mathrm{o}} \cdot \mathbf{z} + b_{\mathrm{o}}\right), \tag{0.21}$$

where $\hat{\mathbf{y}}$ is the prediction vector from the output layer, $\mathbf{w}_{\mathrm{o}}$ is the weight vector applied to the output layer, S is the softmax function, and b_{o} is the bias for the output layer. In this study, the $\hat{\mathbf{y}}$ has two classes: [1, 0] represents non-vuggy and [0, 1] represents vuggy facies. The cross-entropy loss function was used.

In computer vision, if thousands of objects are identified from millions of pictures, CNN architectures with many layers, such as ResNet, Inception, and VGGNet (152, 19, and 16 layers respectively), demonstrate good performance (He et al. 2016, Szegedy et al. 2017, Simonyan and Zisserman 2014). However, for a small dataset like the greyscale image inputs with resolution 60×200 and binary output in this study, large CNNs are not necessary. A recent machine learning competition, the Statoil/C-CORE Iceberg Classifier Challenge, required participants to identify icebergs from two-channel 75×75 images. The top solutions implemented CNNs with few layers and parameters. Figure 3.7 shows the base CNN model with three layers used in this study. The padded

input image (64×208) was fed into convolutional layer 1 (Conv1) with 32 filters yielding output feature maps of dimension 64×208×32. A max pooling layer (Pool1) followed Conv1 to reduce the feature maps to 32×104×32. Conv2 and Pool2 worked similarly to Conv1 and Pool1 but with different sizes. After Pool2, the 3-D feature maps were unrolled into a 1-D vector and fed into a fully connected layer (FC1). Finally, the vuggy or non-vuggy facies labels were predicted.

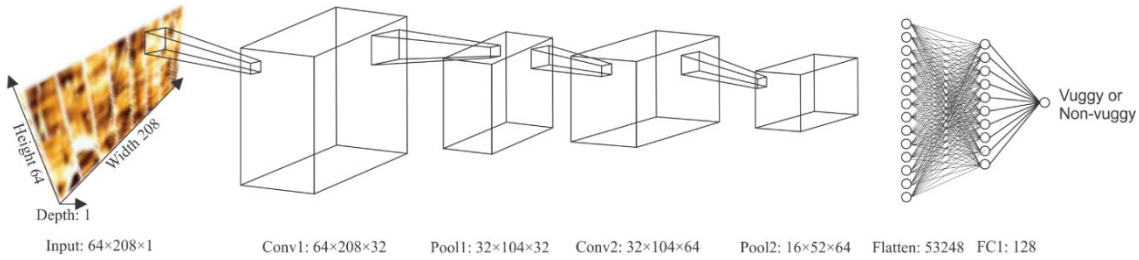

Figure 3.7. Base CNN used in this study.

CNNs were built with TensorFlow GPU 1.8.0 and Keras GPU 2.2.4. TensorFlow is a free and open-source software library for deep learning written in Python. Keras is a high-level neural network application program interface capable of running on top of TensorFlow. Depending on the CNN architecture in this study, training a CNN for 200 epochs took 3 to 7 minutes (NVIDIA Tesla V100). An epoch is defined as presentation of all samples in a training dataset (Table 3.1) to the network.

Hyperparameter Optimization

Hyperparameter optimization is required to maximize classification accuracy for the test dataset by minimizing validation loss. Recall that the CNN was not privy to the test dataset during either training or validation. Hyperparameters provide overarching control of the learning process but are not learned as are network parameters (e.g., node weights and biases). These hyperparameters were divided into two groups: those that

specify network architecture (numbers of convolutional layers and filters and the numbers of dense layers and neurons) and those that minimize overfitting (dropout rates and the patience and minimum delta for early stopping). Dropout randomly disconnects neurons ($w = 0$) during training (Srivastava et al. 2014). Patience is defined as the number of epochs that transpire without decreasing the validation loss by some minimum delta (Witten et al. 2016), whereupon training is stopped. When optimizing the early stopping hyperparameters, additional training runs were not necessary because all training and validation loss data were available from the runs used to optimize the network architecture and dropout rates. Patience ranged from 0 to 20 in unit increments with minimum deltas from 0 to 0.01 in steps of 0.001.

The hyperparameter tuning process was conducted for both the complete and cleaned datasets. Because the GPU algorithm (NVIDIA CUDA® Deep Neural Network library, CuDNN) used in the TensorFlow is non-deterministic (i.e., the same seed number for the random number generator yields slightly different results) (Alberti et al. 2018, Marrone et al. 2019), five Monte Carlo-type iterations were performed for each validation exercise. The CNN was trained five times for each combination of hyperparameters in Table 3.2 (bold entries indicate optimized results) for 200 epochs. These 4800 training runs (10 convolution layer options × 8 dense layer options × 3 convolution layer dropout rates × 4 FC dropout rates × 5 iterations) required fifteen days on the GPU.

Table 3.2. Hyperparameter variations interrogated in this study.

Conv layers	Dense layers	Conv dropout	FC dropout
16, 32	32	0.15	0.3
32, 64	64‡	0.25	0.4
64, 128	128	0.35‡, †	0.5†
16, 32, 64	64, 32		0.6‡
32, 48, 64	128, 64		
32, 64, 128	256, 128†		
64, 128, 256	512, 256		
64, 128, 128	128, 64, 32		
32, 64, 128, 256‡, †			
64, 100, 128, 150			

‡Cleaned dataset.
†Complete dataset.

Figure 3.8 shows the median loss per epoch from these five Monte Carlo iterations where the median training loss (blue curve) always decreased; however, the median validation loss (red curve) reached a minimum before increasing. Table 3.3 lists the optimized early stopping hyperparameters along with overall performance metrics. The validation exercise was stopped at the 74th epoch with a patience of 6 and a minimum delta of 0.03. Despite differences in network sizes, for both datasets the training processes was interrupted at around the 75th epoch. Upon supplying the test datasets to the trained CNN models using optimized hyperparameters, unsurprisingly the cleaned dataset outperformed the complete dataset through both a lower median validation loss and a higher median test accuracy.

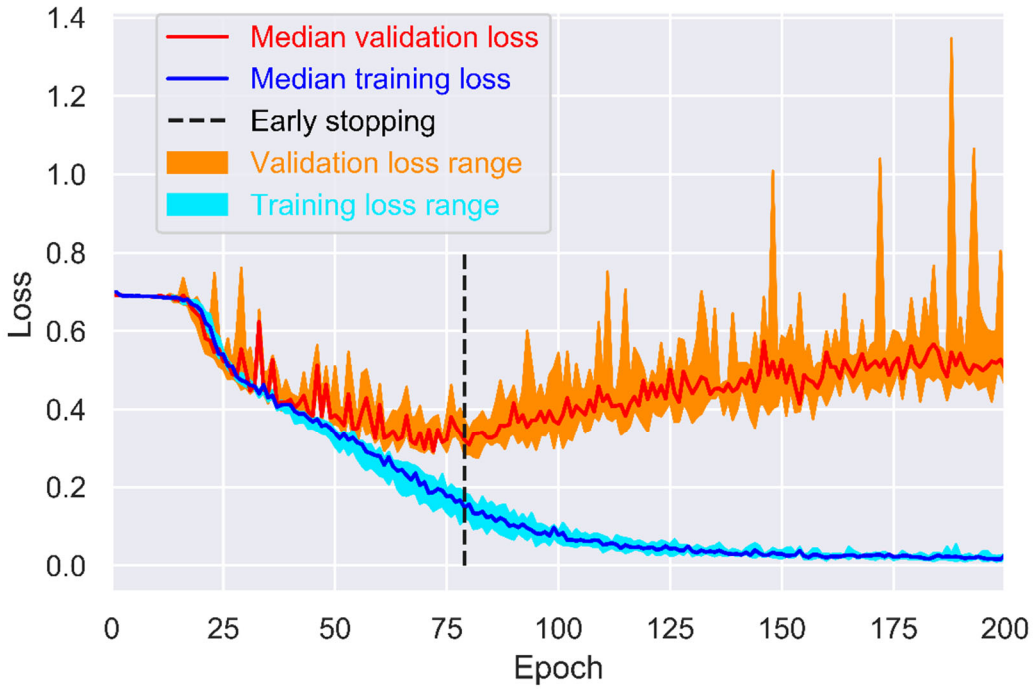

Figure 3.8. Range of the five Monte Carlo iterations showing validation loss (orange) and training loss (cyan) with medians (red and blue curves, respectively). The black dashed line is at the 74th epoch where the training process was interrupted. These results are from the cleaned dataset yielding the lowest validation loss.

Table 3.3. Optimized early stopping hyperparameters for the complete and cleaned datasets as well as model-performance metrics.

Hyperparameters and metrics	Complete dataset	Cleaned dataset
Minimum delta	0	0.03
Patience	8	6
Stopped epoch	79	74
Median validation loss	0.308	0.277
Median test accuracy	0.813	0.847

Results and Discussion

Using the complete dataset to train the base model yielded a median accuracy of 0.791 on the test dataset. After hyperparameter optimization, prediction accuracies from the five Monte Carlo realizations trained using the complete dataset ranged from 0.794 to 0.836 with a median of 0.813 (a 3% improvement); however, the cleaned dataset had a median test accuracy of 0.847 (a 7% improvement) and ranged from 0.800 to 0.861. The improved accuracy reflects the significance of hyperparameter optimization and data-quality control in this image-based deep-learning study. Figure 3.9 compares the CNN outputs from the complete and cleaned dataset to the labeled dataset.

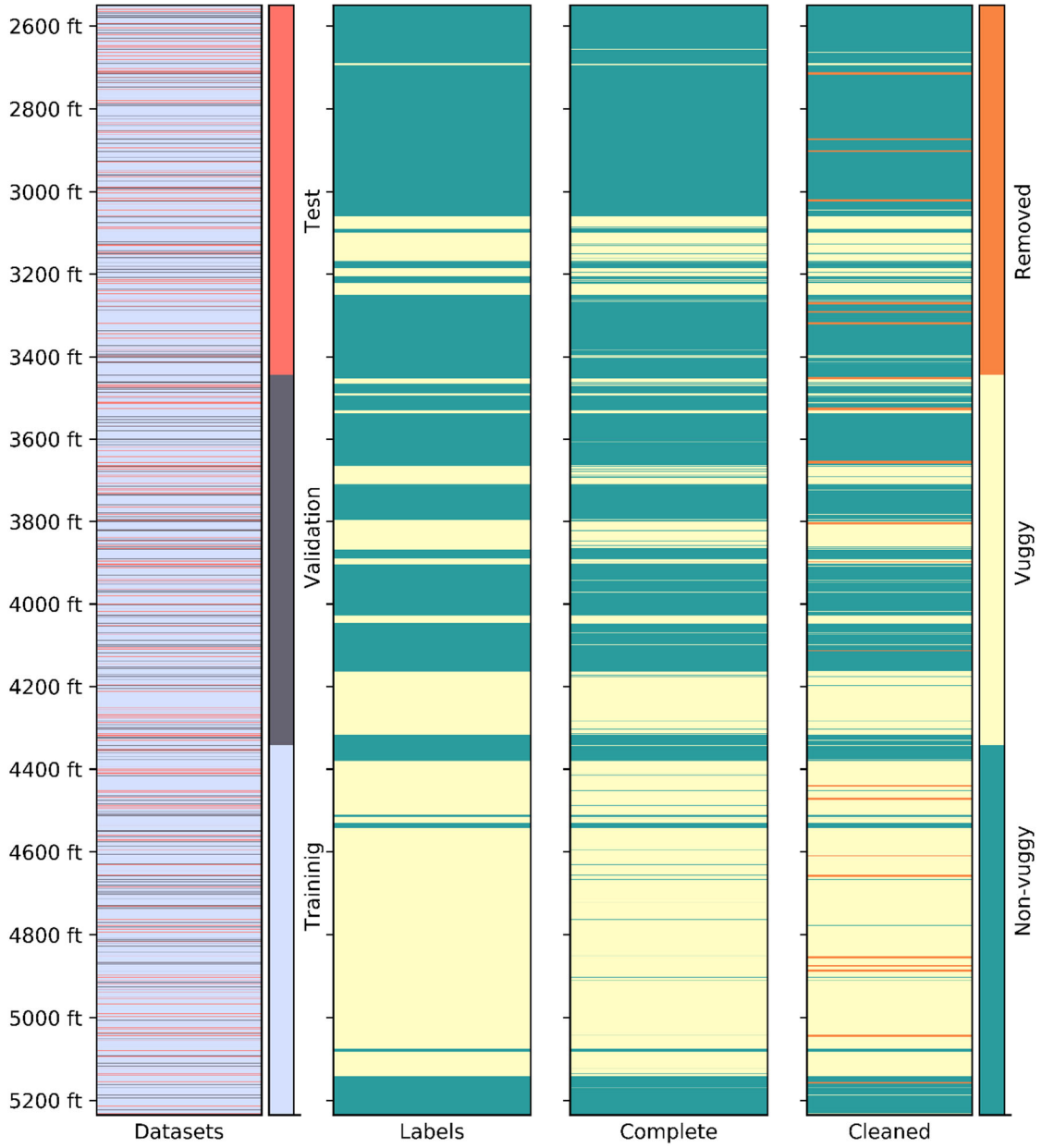

Figure 3.9. Facies predictions for both complete and cleaned datasets using the optimized hyperparameters (Tables 3.2 and 3.3) compared to the labeled dataset. The first column indicates how the data were partitioned into training, validation, and testing datasets.

It is not uncommon to hear deep learning be described as a "black box;" however, the authors believe that it is critical to dispel this myth. By combining domain expertise with the science and numerics behind machine learning, we go beyond simply reporting accuracies to identify the reasons why the model failed to correctly classify vuggy formations. Figure 3.10 shows three examples of misclassification from the optimized CNN trained on the cleaned dataset (median accuracy of 0.847) with columns indicating the input image, label, prediction, and vuggy/non-vuggy probability, respectively. Shale layers, which frequently appeared in the datasets, were associated with dark pixels. Moreover, there was a pattern in their spatial continuity; they were arranged contiguously, especially in horizontal directions because of layering. In Figure 3.10, misclassifications were due to (a) interbedded thin shale layers, (b) a cavity, and (c) horizontal fractures. Figure 3.10(a) substantiates the concerns discussed in the Geologic Background about vertical geologic heterogeneity in the Arbuckle group. If an input sample had interbedded alternating facies (e.g., thin shale layers between thicker limestone layers), a geologist might label this interval as vuggy because limestone was the dominant facies. However, the CNNs were sensitive to the presence of dark pixels, which are interpreted as shale (non-vuggy). Figure 3.10(b) further demonstrates misclassifications of an interval with dark pixels; the CNN classified this image as non-vuggy because of the chunk of dark pixels, which were interpreted as shale. Artifact can also arise from the way in which the images were partitioned (clipped). The dark pixels at the bottom of Figure 3.10(c) are a horizontal fracture. When the image was clipped across this fracture, to the CNN, the pixel arrangement was consistent with the common spatial contiguity of shale pixels. Without more training data, these less-frequent features

(e.g., horizontal fractures, cavities, cherts, etc.) were misidentified as shale layers (non-vuggy). Note also that misclassified samples such as Figure 3.10(c) often had nearly equal probabilities of being vuggy or non-vuggy facies indicating less confidence in this prediction from the CNN.

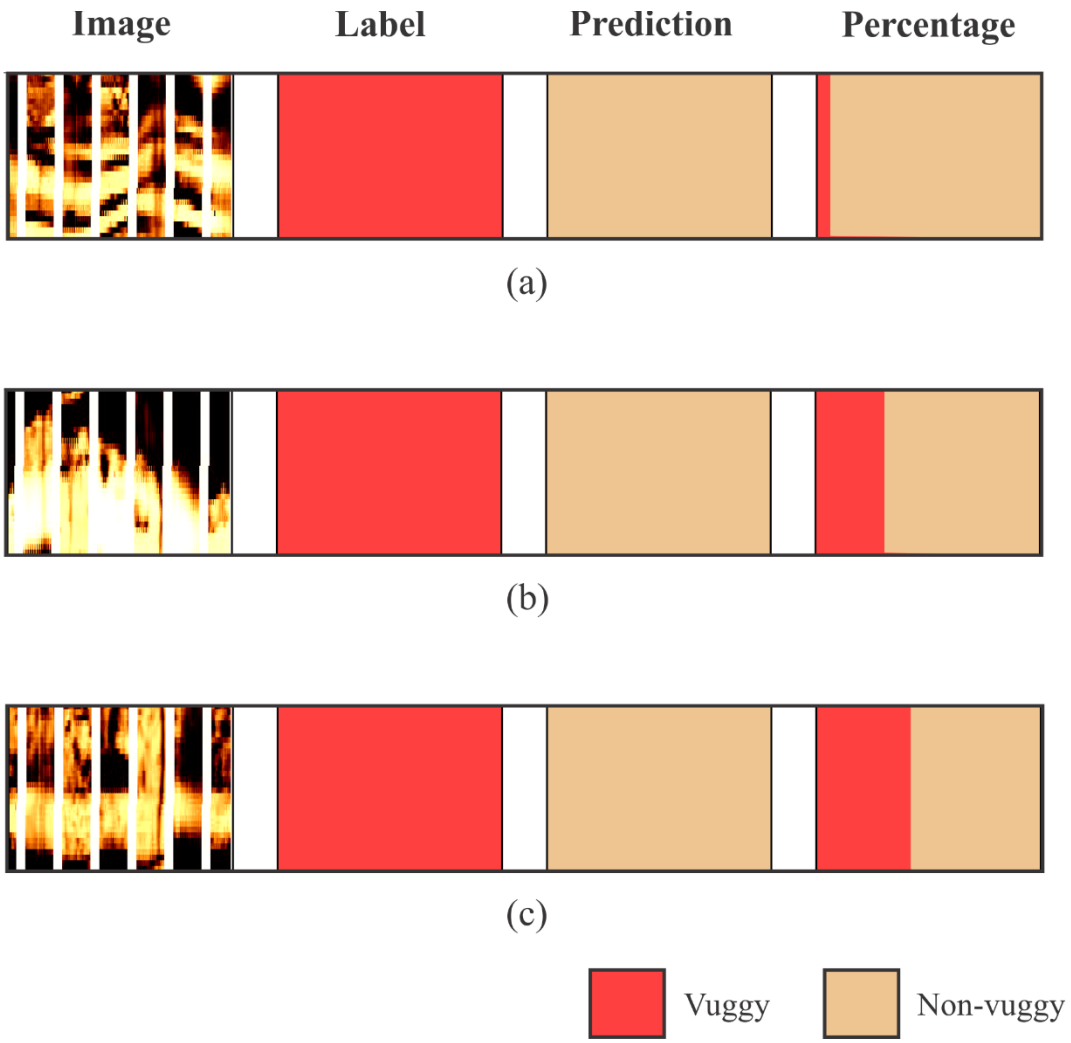

Figure 3.10. Misclassification due to (a) thin shale layers; (b) with cavity; (c) horizontal and vertical fractures, however the probability still provides some information.

Figure 3.11 shows confusion matrices for the median accuracy of the complete and cleaned datasets (Tables 3.2 and 3.3). Rows indicate prediction accuracies for each facies while columns represent the labels. Overall accuracies were higher for the cleaned dataset with a more balanced performance between vuggy and non-vuggy facies.

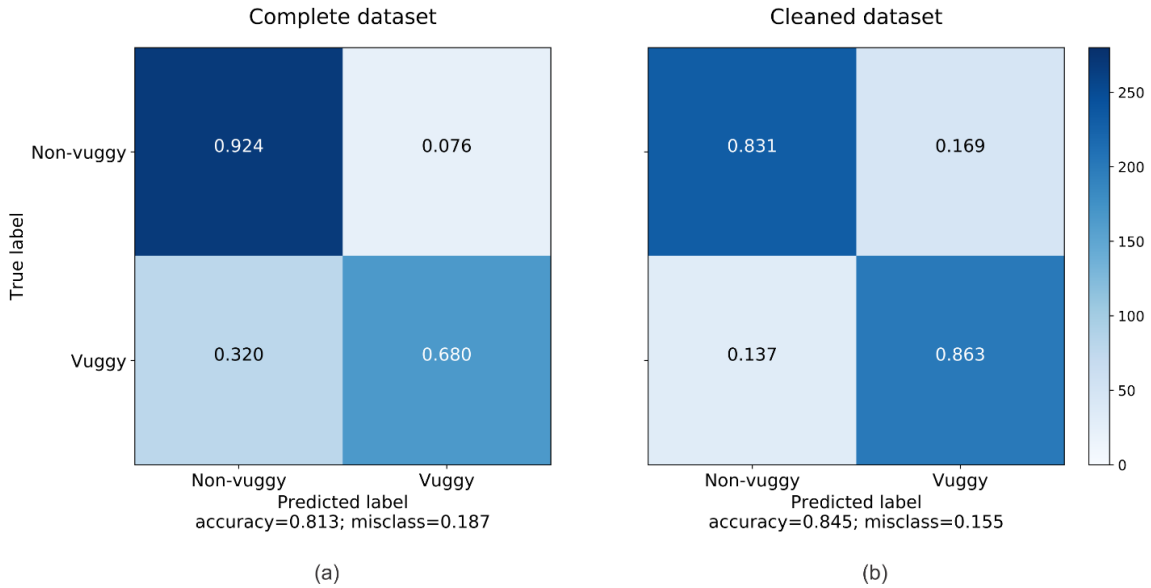

Figure 3.11. Confusion matrices for (a) the complete and (b) cleaned datsets based on the configurations in (Tables 3.2 and 3.3). Rows indicate prediction accuracies for each facies while columns are those for manual interpreted labels. There is better accuracy for non-vuggy facies prediction than vuggy faices for the complete dataset and equal accuracy for the cleaned dataset.

It is important to keep in mind that because the datasets came from a single well, it would not be appropriate to apply this trained CNN with its optimized hyperparameters to datasets from different wells without additional validation exercises. To extend the application of this modeling framework, a larger dataset must be assembled – one that includes the range of lithologic and diagenetic features present in the Arbuckle Group.

Conclusions and Future Work

In this study, the geology at the Wellington 1-32 borehole was classified as either vuggy or non-vuggy using a combination of core descriptions and conventional data including gamma ray, neutron/density porosity, photoelectric factor, and NMR T2. Next, a CNN-based deep-learning framework was constructed to automate facies classification according to microrestivity images. First, the microresistivity image for the entire borehole was divided into 5355 images (64×208 pixels after padding). This complete dataset was analyzed and those images with poor quality were removed from consideration (cleaned dataset). Next, both complete and cleaned datasets were split into training/validation/test datasets in a 0.8/0.1/0.1 ratio. Hyperparameters defining the network architecture and minimizing overfitting were optimized to minimize validation losses. Importantly, because the GPU algorithm is not repeatable, during the optimization process, each hyperparameter combination was repeated five times and the median validation losses were reported. Before hyperparameter optimization, the base CNN model yielded an accuracy of 0.791, which was improved to 0.813 (3%) with the complete dataset and 0.847 (7%) with the cleaned dataset when using optimized hyperparameters, highlighting the significance of data quality control in machine learning projects.

Optimal results can never be achieved by blindly applying machine-learning models. Instead, both domain knowledge and insight from data science are needed to interpret the results from machine learning models. Mispredictions were investigated and were largely a result of the single-well dataset failing to adequately capture the range of heterogeneity in the Arbuckle Group. For example, features like cavities, which have

dark pixels, were under-represented in the training and validation data, thus making them difficult to distinguish from shale, which are also characterized by dark pixels.

To improve its robustness, this method should be applied to multiwell datasets because the ultimate goal is to use trained machine learning models to quickly classify newly acquired microresistivity logs. Moreover, the framework developed here could easily be extended to identify other geologic features including fractures, beddings, and lithologies. Finally, the present study has laid the foundation for pixelwise segmentation of microrestivity logs. In addition to classifying vuggy formations, the authors intend to use CNNs to estimate vug porosity by counting the number of vug pixels in each image.

Acknowledgments

The authors wish to acknowledge the use of the Aramco Americas Houston Research Center facilities for this study. Jiajun Jiang was a graduate intern for Aramco Americas for a portion of the time that this study was conducted. The authors sincerely thank Dr. Dawn McAlpin for her assistance with data labeling and extend special thanks to Dr. Weichang Li for his technical review.

References

Adler, F. J., Adler, F. J., Caplan, W. M. et al. 1971. Future Petroleum Provinces of the Mid-Continent, Region 7. *Future petroleum provinces of the United States: Their geology and potential: AAPG Memoir* **15**: 985–1120. https://doi.org/10.1306/02060705012.

Alberti, M., Pondenkandath, V., Würsch, M. et al. 2018. Deepdiva: A Highly-Functional Python Framework for Reproducible Experiments. Presented at the 2018 16th International Conference on Frontiers in Handwriting Recognition (ICFHR), Niagara Falls, NY, USA,. https://doi.org/10.1109/ICFHR-2018.2018.00080.

Ausbrooks, R., Hurley, N. F., May, A. et al. 1999. Pore-Size Distributions in Vuggy Carbonates from Core Images, Nmr, and Capillary Pressure. Presented at the SPE annual technical conference and exhibition, Houston, TX. SPE-56506-MS. https://doi.org/10.2118/56506-MS.

Bergen, K. J., Johnson, P. A., Maarten, V. et al. 2019. Machine Learning for Data-Driven Discovery in Solid Earth Geoscience. *Science* **363** (6433): eaau0323. https://doi.org/10.1126/science.aau0323.

Chen, M. C., Ball, R. L., Yang, L. et al. 2017. Deep Learning to Classify Radiology Free-Text Reports. *Radiology* **286** (3): 845-852. https://doi.org/10.1148/radiol.2017171115.

Choquette, P. W. and Pray, L. C. 1970. Geologic Nomenclature and Classification of Porosity in Sedimentary Carbonates. *AAPG bulletin* **54** (2): 207-250. https://doi.org/10.1306/5D25C98B-16C1-11D7-8645000102C1865D.

Cole, V. B. 1975. Subsurface Ordovician-Cambrian Rocks in Kansas. *Reprinted 1981ed) Lawrence, Kansas: Kansas Geological Survey* **2**.

Cunningham, K. J., Carlson, J. I., and Hurley, N. F. 2004. New Method for Quantification of Vuggy Porosity from Digital Optical Borehole Images as Applied to the Karstic Pleistocene Limestone of the Biscayne Aquifer, Southeastern Florida. *Journal of Applied Geophysics* **55** (1-2): 77-90. https://doi.org/10.1016/j.jappgeo.2003.06.006.

Doveton, J. and Watney, L. 2014. Textural and Pore Size Analysis of Carbonates from Integrated Core and Nuclear Magnetic Resonance Logging: An Arbuckle Study. *Interpretation* **3** (1): SA77-SA89. https://doi.org/10.1190/INT-2014-0050.1.

Franseen, E. 1994. Facies and Porosity Relationships of Arbuckle Strata: Initial Observations from Two Cores, Rice and Rush Counties, Kansas: Kansas Geol. *Survey Open-File Rep*: 94-53.

Franseen, E. 2000. A Review of Arbuckle Group Strata in Kansas from a Sedimentologic Perspective: Insights for Future Research from Past and Recent Studies. *The Compass: Earth Science Journal of Sigma Gamma Epsilon* **75** (2-3): 68-89.

Franseen, E. K., Brynes, A. P., Cansler, J. R. et al. 2004. The Geology of Kansas Arbuckle Group. *Midcontinent Geoscience*: 1-43.

Franseen, E. K. and Byrnes, A. P. 2012. Arbuckle Group Platform Strata in Kansas: A Synthesis.

He, K., Zhang, X., Ren, S. et al. 2016. Deep Residual Learning for Image Recognition. *Proc.,* Proceedings of the IEEE conference on computer vision and pattern recognition770-778. https://doi.org/10.1109/cvpr.2016.90

Hu, F., Xia, G.-S., Hu, J. et al. 2015. Transferring Deep Convolutional Neural Networks for the Scene Classification of High-Resolution Remote Sensing Imagery. *Remote Sensing* **7** (11): 14680-14707. https://doi.org/10.3390/rs71114680.

James, S. C., Zhang, Y., and O'Donncha, F. 2018. A Machine Learning Framework to Forecast Wave Conditions. *Coastal Engineering* **137**: 1-10. https://doi.org/10.1016/j.coastaleng.2018.03.004.

Jobe, T., Vital-Brazil, E., and Khaif, M. 2018. Geological Feature Prediction Using Image-Based Machine Learning. *Petrophysics* **59** (06): 750-760. https://doi.org/10.30632/PJV59N6-2018a1.

Jungmann, M., Kopal, M., Clauser, C. et al. 2011. Multi-Class Supervised Classification of Electrical Borehole Wall Images Using Texture Features. *Computers & geosciences* **37** (4): 541-553. https://doi.org/10.1016/j.cageo.2010.08.008.

Kalchbrenner, N., Grefenstette, E., and Blunsom, P. 2014. A Convolutional Neural Network for Modelling Sentences. *arXiv preprint arXiv:14042188*. https://doi.org/10.3115/v1/p14-1062

Keroher, R. P. and Kirby, J. J. 1948. *Upper Cambrian and Lower Ordovician Rocks in Kansas*: University of Kansas publications.

Krizhevsky, A., Sutskever, I., and Hinton, G. E. 2012. Imagenet Classification with Deep Convolutional Neural Networks. *Proc.,* Advances in neural information processing systems1097-1105. https://doi.org/10.1145/3065386.

Lary, D. J., Alavi, A. H., Gandomi, A. H. et al. 2016. Machine Learning in Geosciences and Remote Sensing. *Geoscience Frontiers* **7** (1): 3-10. https://doi.org/10.1016/j.gsf.2015.07.003.

LeCun, Y. and Bengio, Y. 1995. Convolutional Networks for Images, Speech, and Time Series. *The handbook of brain theory and neural networks* **3361** (10): 1995.

LeCun, Y., Bengio, Y., and Hinton, G. 2015. Deep Learning. *nature* **521** (7553): 436. https://doi.org/10.1038/nature14539.

Lee, H. and Kwon, H. 2017. Going Deeper with Contextual CNN for Hyperspectral Image Classification. *IEEE Transactions on Image Processing* **26** (10): 4843-4855. https://doi.org/10.1109/TIP.2017.2725580.

Li, B., Tan, X., Wang, F. et al. 2017. Fracture and Vug Characterization and Carbonate Rock Type Automatic Classification Using X-Ray Ct Images. *Journal of Petroleum Science and Engineering* **153**: 88-96. https://doi.org/10.1016/j.petrol.2017.03.037.

Lønøy, A. 2006. Making Sense of Carbonate Pore Systems. *AAPG bulletin* **90** (9): 1381-1405. https://doi.org/10.1306/03130605104.

Lucia, F. 1983. Petrophysical Parameters Estimated from Visual Descriptions of Carbonate Rocks: A Field Classification of Carbonate Pore Space. *Journal of petroleum technology* **35** (03): 629-637. SPE-10073-PA. https://doi.org/10.2118/10073-PA.

Lucia, F. J. 1995. Rock-Fabric/Petrophysical Classification of Carbonate Pore Space for Reservoir Characterization. *AAPG bulletin* **79** (9): 1275-1300. https://doi.org/10.1306/7834D4A4-1721-11D7-8645000102C1865D.

Marrone, S., Olivieri, S., Piantadosi, G. et al. 2019. Reproducibility of Deep CNN for Biomedical Image Processing across Frameworks and Architectures. *Proc.,* 2019 27th European Signal Processing Conference (EUSIPCO)1-5. https://doi.org/10.23919/EUSIPCO.2019.8902690.

Newberry, B., Grace, L., and Stief, D. 1996. Analysis of Carbonate Dual Porosity Systems from Borehole Electrical Images. *Proc.,* Permian Basin Oil and Gas Recovery ConferenceSPE-35158-MS. https://doi.org/10.2118/35158-MS.

Ross Jr, R. J. 1976. Ordovician Sedimentation in the Western United States. Presented at the Rocky Mountain Association of Geologists Symposium.

Russakovsky, O., Deng, J., Su, H. et al. 2015. Imagenet Large Scale Visual Recognition Challenge. *International journal of computer vision* **115** (3): 211-252. https://doi.org/10.1007/s11263-015-0816-y.

Simonyan, K. and Zisserman, A. 2014. Very Deep Convolutional Networks for Large-Scale Image Recognition. *arXiv preprint arXiv:14091556*.

Srivastava, N., Hinton, G., Krizhevsky, A. et al. 2014. Dropout: A Simple Way to Prevent Neural Networks from Overfitting. *The journal of machine learning research* **15** (1): 1929-1958. https://dl.acm.org/doi/abs/10.5555/2627435.2670313.

Steinhauff, M., Franseen, E., and Byrnes, A. 1998. Arbuckle Reservoirs in Central Kansas—Relative Importance of Depositional Facies, Early Diagenesis and Unconformity Karst Processes on Reservoir Properties: Kansas Geological Survey. *Open-file Report*: 98-55.

Szegedy, C., Ioffe, S., Vanhoucke, V. et al. 2017. Inception-V4, Inception-Resnet and the Impact of Residual Connections on Learning. *Proc.,* Thirty-First AAAI Conference on Artificial Intelligence.

Tilke, P. G., Allen, D., and Gyllensten, A. 2006. Quantitative Analysis of Porosity Heterogeneity: Application of Geostatistics to Borehole Images. *Mathematical Geology* **38** (2): 155-174. https://doi.org/10.1007/s11004-005-9011-y.

USGS. 2006. FGDC Digital Cartographic Standard for Geologic Map Symbolization. *US Geological Survey Techniques and Methods* **11** (A2). https://doi.org/10.3133/tm11a2

Vik, B., Djurhuus, K., Spildo, K. et al. 2007. Characterisation of Vuggy Carbonates. *Proc.,* SPE/EAGE Reservoir Characterization and Simulation ConferenceSPE-111434-MS. https://doi.org/10.2118/111434-MS.

Walters, R. F. 1958. Differential Entrapment of Oil and Gas in Arbuckle Dolomite of Central Kansas. *AAPG Bulletin* **42** (9): 2133-2173.

Wilson, J., Fritz, R., and Medlock, P. 1991. The Arbuckle Group: Relationship of Core and Outcrop Analyses to Cyclic Stratigraphy and Correlation. *Proc.,* Arbuckle core workshop and field trip: Oklahoma Geological Survey Special Publication133-144.

Witten, I. H., Frank, E., Hall, M. A. et al. 2016. *Data Mining: Practical Machine Learning Tools and Techniques*: Morgan Kaufmann.

Wu, X., Liang, L., Shi, Y. et al. 2019. Faultseg3d: Using Synthetic Data Sets to Train an End-to-End Convolutional Neural Network for 3d Seismic Fault Segmentation. *Geophysics* **84** (3): IM35-IM45. https://doi.org/10.1190/geo2018-0646.1.

Xu, C., Misra, S., Srinivasan, P. et al. 2019. When Petrophysics Meets Big Data: What Can Machine Do? *Proc.,* SPE Middle East Oil and Gas Show and Conference. https://doi.org/10.2118/195068-MS.

Yamashita, R., Nishio, M., Do, R. K. G. et al. 2018. Convolutional Neural Networks: An Overview and Application in Radiology. *Insights into imaging* **9** (4): 611-629. https://doi.org/10.1007/s13244-018-0639-9.

CHAPTER FOUR

Drilling-induced Fracture Segmentation Using a Convolutional Neural Network

This chapter prepared as: Jiang, J., James, S.C.
Drilling-induced Fracture Segmentation Using a Convolutional Neural Network,
Journal of Petroleum Science & Engineering.

Abstract

Identifying drilling-induced fractures (DIFs) and understanding their genesis are critical for reservoir geomechanical analyses. Although microresistivity image logs have been used to trace DIFs, this process is labor intensive and typically requires expensive software. Recently, Fully Convolutional Network (FCN) algorithms have approached human-level performance at multi-image semantic segmentation tasks. A modified U-Net, a form of FCN, was used to segment DIFs from a microrestivity image log from a well in the Arbuckle Group in Kansas. The U-Net algorithm was trained with the borehole resistivity image (feature) against manually labeled image logs (label: 1 for DIF pixels, 0 for non-DIF pixels) using two datasets. The first of these was simply the original borehole resistivity log while the second (augmented) included the mirror image of the original dataset. A balanced cross-entropy loss function was used because of the unbalanced label data (about 60× more non-fracture pixels than fracture pixels). After training, each U-Net model (trained on one of the two datasets) made predictions for a continuous segment of the borehole. Because of the potential for discontinuities in predictions across adjacent image logs of a continuous borehole segment, a stitching strategy was implemented by vertically overlapping pixels, which were Gaussian

weighted. All predictions achieved better than 0.56 intersection over union performance thus demonstrating the robustness of this U-Net model for DIF segmentation. Moreover, the model trained on the augmented dataset outperformed that trained on the original dataset (intersection over union of 0.73 versus 0.61). Finally, consistent with other studies, we demonstrated that overlapping pixels improved prediction accuracy. This effort lays the foundation for developing U-Nets to segment natural fractures, beddings, and vugs.

Introduction

During the drilling and production phases of developing petroleum and geothermal reservoirs, reservoir geomechanical analyses are necessary to prevent wellbore sidewall collapse or wellbore failure (Dasgupta et al. 2019, Zoback 2010, Fellgett et al. 2018, Brudy and Zoback 1999). Also, reservoir geomechanics significantly govern hydrofracturing procedures for unconventional petroleum reservoirs (Weng 2015). The stress state, which is simply represented by three end-member regimes (vertical stress S_v, maximum horizontal stress S_H, and minimum horizontal stress S_h) provides key controls for reservoir geomechanics models (Dasgupta et al. 2019, Zoback 2010).

Because S_v is due to overburden pressure, it can be estimated from density logs (Tingay et al. 2003). The horizontal stresses, S_h and S_H, are largely affected by global and reginal tectonic stresses (Brudy and Zoback 1999, Zoback 1992). The magnitude of S_h is measured with leak-off tests or from hydro-fracturing data (De Bree and Walters 1989, Raaen et al. 2006). The magnitude of S_H can be calculated based on known S_h (Brudy and Zoback 1999). The orientations of S_h and S_H can be estimated from well breakouts and

drilling-induced fractures (DIFs). One of the best methods to identify well breakouts and DIFs is through examination of image logs. Traditionally, well-trained engineers or geoscientists visualize and interpret image logs with software suites (Dasgupta et al. 2019). This study identifies DIFs using a deep-learning method based on open-source Python libraries, which can improve time and cost efficiencies.

When a wellbore is drilled, the cylindrical hollow volume provides no support for surrounding rock. Once stresses concentrated at the well sidewall exceed the rock compressive strength, breakouts occur (Bell and Gough 1979, Zhou 1994), which are wellbore enlargements (sidewall spalling) caused by compressive failures. Previous studies have shown that spalling occurs along the S_h direction and are separated by 180° (Brudy and Zoback 1999, Tingay et al. 2003).

On the other hand, if stresses at the well sidewall exceed the rock tensile strength, DIFs occur (Barton and Zoback 2002, Tingay et al. 2003). There are two types of DIFs: vertical and en-echelon DIFs. DIFs typically come in pairs separated by 180° along the S_H direction (Brudy and Zoback 1999). Vertical DIFs are parallel or near parallel to the well axis, whereas en-echelon DIFs are inclined to the well axis. Under theoretical conditions, both types of DIFs should be separated by 90° from breakouts.

DIFs can be difficult to identify on conventional wireline logs because these logs lack dimensional resolution; DIFs are 3D features and wireline data are 1D. To identify and further segment DIFs, image logging tools, which can generate 2D images based on physical-property contrasts of wellbore sidewall, are used. Generally, there are two types of image-logging tools can be used: resistivity and acoustic image-logging tools. Compared to acoustic image-logging tools, resistivity tools are more sensitive to finer

scale geologic features (Ja'fari et al. 2012, Massiot et al. 2015). This study used resistivity image logs.

Machine learning (ML) has proven to be a powerful tool for identification of geologic features from unstructured data (Bergen et al. 2019, James et al. 2018, Lary et al. 2016, Xu et al. 2019). Among ML algorithms, a convolutional neural network (CNN) was selected because of successful applications to computer-vision problems (Kalchbrenner et al. 2014, Krizhevsky et al. 2012, LeCun et al. 2015). More specifically, fracture segmentation is a form of image semantic segmentation. Fully convolutional networks (FCNs), a subset of CNNs, have outperformed other methods for image semantic segmentation tasks (Ronneberger et al. 2015, Long et al. 2015). A recent milestone by Wu et al. (2019) impressed the petroleum geoscience community by demonstrating that an FCN beat all other previous methods for fault-picking tasks from 3D seismic datasets. This study segmented vertical DIFs in a borehole resistivity image log by applying an FCN.

Vertical Drilling-induced Fractures

Here, we assumed that the well axis is vertically drilled and the S_v is a principal stress. As mentioned above, a hole drilled in an ideal elastic medium concentrates stresses on the wellbore sidewall. Kirsch (1898) concluded that stress is a function of angular position and radial distance from the center of the wellbore for a circular hole in an elastic medium and this is expressed mathematically as:

$$\sigma_\theta = S_H + S_h - 2\left(S_H - S_h\right)\cos 2\theta - 2P_0 - \Delta P, \tag{22}$$

where σ_θ is the tangential stress around the borehole, θ is the angle around the borehole wall start from the orientation of S_H, P_0 is pore pressure, and ΔP is the pressure difference

between P_0 and the drilling mud pressure. In the preceding equation, when θ equals $\pi/2$ or $3\pi/2$, the maximum σ_θ coincides with the minimum horizontal stress S_h while the minimum σ_θ coincides with the maximum horizontal stress S_H at $\theta = 0$ or π as shown in Figure 4.1.

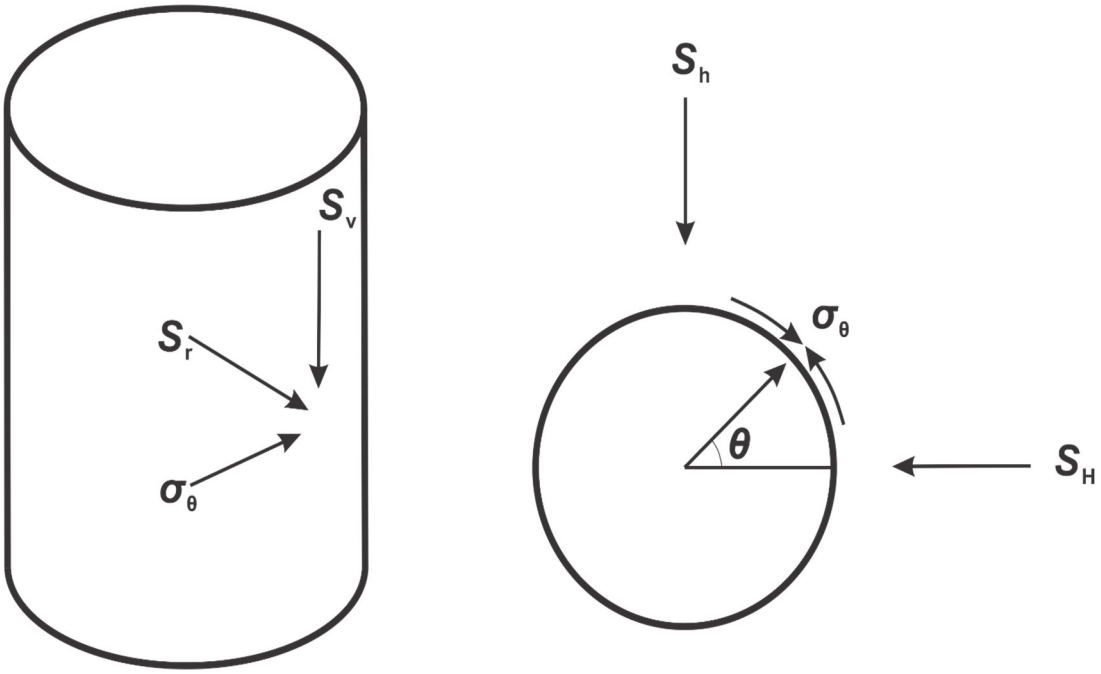

Figure 4.1. Stress on the borehole sidewall.

Thus, breakouts (sidewall spalling) tend to occur in alignment with S_h if the (maximum) σ_θ exceeds the rock compressive strength. Conversely, in the direction of S_H, DIFs tend to occur because the rock tensile strength (T) is overcome when aligned with minimum σ_θ. The conditions that can initialize vertical DIFs can be derived from (1):

$$3S_h - S_H - 2P_0 - \Delta P < T. \qquad (23)$$

S_h and S_H are primarily controlled by tectonic stresses. Additionally, pore and drilling mud pressures also play important roles in the initiation of vertical DIFs.

In real systems, vertical DIFs are not absolutely straight and often slightly inclined. These situations may be caused by, among other things, well axis deviation, a principal stress other than S_v, and rock heterogeneity (Brudy and Zoback 1999). Because this study focused on fracture segmentation of resistivity images, further discussion of geomechanics is beyond the scope of this paper.

Fractures on Image Logs

A typical resistivity image-logging tool has 4, 6, or 8 pads that are pressed against the borehole sidewall. Halliburton's XRMI used in this study has 6 pads spaced 60° apart (Nie et al. 2013, Lai et al. 2018). Electrical currents are forced into the rock through electric node arrays on each pad. Geologic features and lithologies can be identified by different resistivity responses received by the tool. Light-colored (white-yellow) pixels represent resistive materials cement and dense rocks, organic matter, or hydrocarbon-bearing rocks; dark-colored (brown-black) pixels represent conductive clay and shale or water-invaded voids and pore spaces (Khoshbakht et al. 2012, Muniz and Bosence 2015, Lai et al. 2018).

In this study, the borehole image log was taken from a well with water-based drilling mud, so the mud-invaded open fractures should be shown in dark colors. Because we targeted vertical DIFs, different types of fractures must be distinguished: (1) natural fractures are shown as partial or full sinusoidal waves because these are failure planes intersected with the borehole; (2) vertical or tensile DIFs are parallel or near-parallel to well axis (vertical wells) and appear in pairs spaced 180° apart; (3) en-echelon DIFs are inclined and also have 180° offsets (they look like well-known en-echelon faults or fractures in geology).

Data Preparation

Data used in this study were from the Wellington KGS 1-32 well, Arbuckle Group (Figure 2 and Figure 3). The Arbuckle Group ranges from 150 to 1,500 m thick and covers most Kansas (Keroher and Kirby 1948, Cole 1975). The existing geological model of the Arbuckle Group is mainly based on early well drillings (1917–1940); however, only shallow portions of the formation (3 to 15 m) were broken through with low-quality logging data that do not meet modern standards (Franseen and Byrnes 2012). In recent decades, deep wells with modern logging data were accessible for Arbuckle Group rocks, but core samples are only available in handful wells. What's more, the dearth of equivalent strata and a biostratigraphic framework limits a comprehensive understanding of the Arbuckle Group. As a target, especially for gas production and carbon-dioxide sequestration, more study in detail need to be engaged to evaluate its economic values.

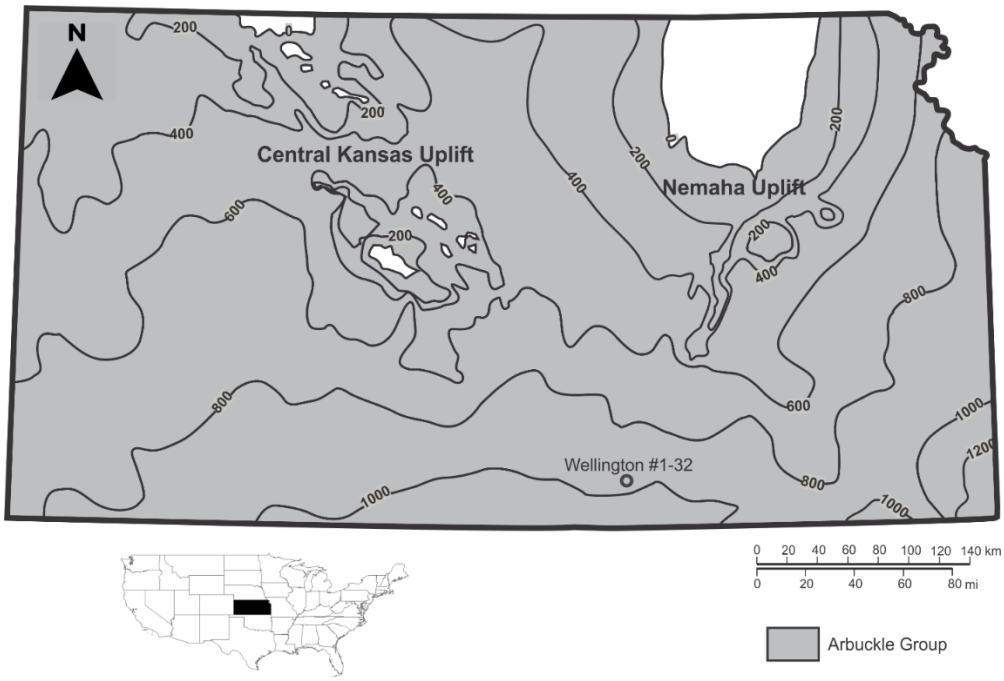

Figure 4.2. Location of Wellington #1-32 and isopach map of the Kansas Arbuckle Group, which is thicker in southeastern Kansas and absent in the white area. Contours were modified from Cole (1975).

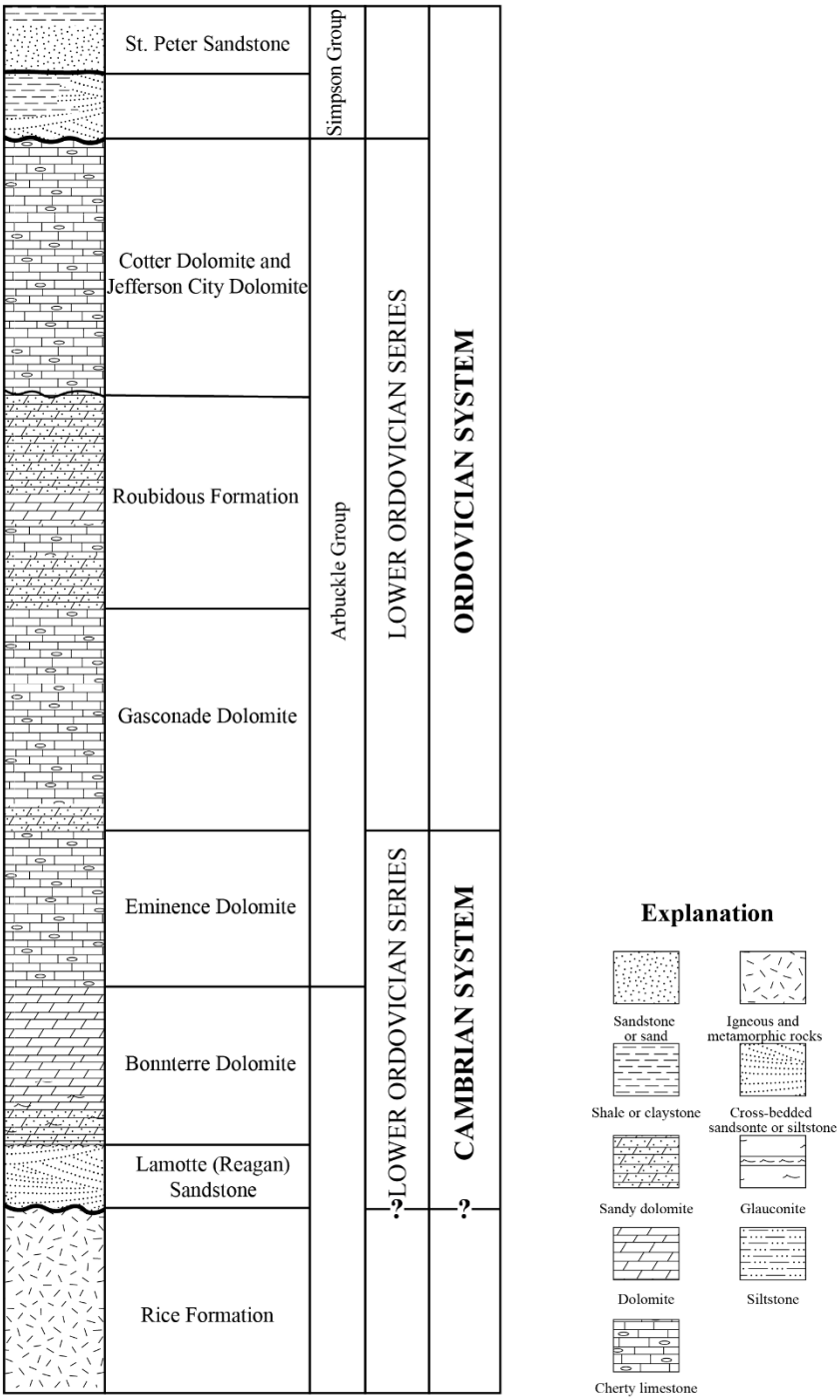

Figure 4.3. Stratigraphic chart for the Arbuckle Group and adjacent formations (modified from Franseen and Byrnes, 2012).The lithologic patterns were from USGS (2006). Cambrian-Ordovician Arbuckle Group rocks are mainly composed of shallow-water subtidal to peritidal carbonates.

The dataset (2,695 ft (821.4 m) of images from 2,549 (776.9) to 5,244 ft (1,600 m) below surface) covers the Cambrian-Ordovician Arbuckle Group as well as the overburden Simpson Group and underburden Precambrian igneous formations. Given the paucity of training data (due to the labor-intensive manual labeling exercise) only 500 ft (152.4 m) (from 3,466 (1,056.4) to 3,966 ft (1,208.8 m)) and 83 ft (25.3 m) (from 3,966 (1,208.8 m) to 4,049 ft (1,234.1)) of images were labeled and used as the training and test datasets , respectively. Notably, having a small training dataset often precludes effective development of machine learning models; however, here, if the U-Net model can be effectively trained on this small dataset, then the robustness of the algorithm will be demonstrated. The medical image processing software, ImageJ, was used to manually label vertical DIFs (Abràmoff et al. 2004). A labeled image is the same size as the corresponding log image; it is a binary image where 1 and 0 denote fracture and non-fracture pixels, respectively.

The original image and labels with a width of 200 pixels and a length of 60,000 pixels (500 ft × 120 pixels/ft) (152.4 m × 394 pixels/m) need to be divided into a smaller, trainable sizes for ML exercises. A moving window with a size of 128×128 scanned the resistivity image and corresponding labeled image horizontally before jumping to the next row for another horizontal scan. Two scans were taken across each row with 56-pixel overlap. This process was repeated over the entire 60,000-pixel image and each 128×128 scan was saved as an input sample and an image label. To accommodate the balanced cross-entropy loss function (discussed later), samples with no labeled fracture pixels were screened out. Ultimately, the training dataset had 310 samples while the

augmented training dataset comprised those 310 samples along with another 310 samples that were the mirror images (upside down) of the original dataset.

Methodology

For image classification tasks, CNN frameworks such as ResNet, Inception, and VGGNet have proven their robustness (He et al. 2016, Simonyan and Zisserman 2014, Szegedy et al. 2017). However, these frameworks typically output 1D vectors that cannot provide enough information for image segmentation. Long et al. (2015) introduced an FCN that includes only convolutional layers (no fully connected layers) and therefore produces segmentation maps that have the same dimensions as the input images. However, their FCN had several drawbacks including poor time efficiency, global context information was ignored, and limited application to 3D images (Liu et al. 2015, Minaee et al. 2020).

To improve the performance of this FCN, FCN variants were invented (He et al. 2017, Zhao et al. 2017, Liu et al. 2015). U-Net, the encoder-decoder-based FCN used in this study, was originally designed for biological microscopy image segmentation (Ronneberger et al. 2015). The original U-Net was applied to images with dimensions of 572×572. Due to our smaller input (128×128 greyscale images), the U-Net used in this study had fewer layers each with reduced dimensions.

Generally, a U-Net comprises two parts: a contracting path on the left and an expanding path on right. The contracting path functions as an encoder that compresses input images into a latent space. Here, the latent space refers to a feature representation (usually with smaller dimensions) that distills and saves useful semantic information

(Minaee et al. 2020, Ronneberger et al. 2015). The expanding path (decoder) predicts segmentation based on the information stored in the latent space.

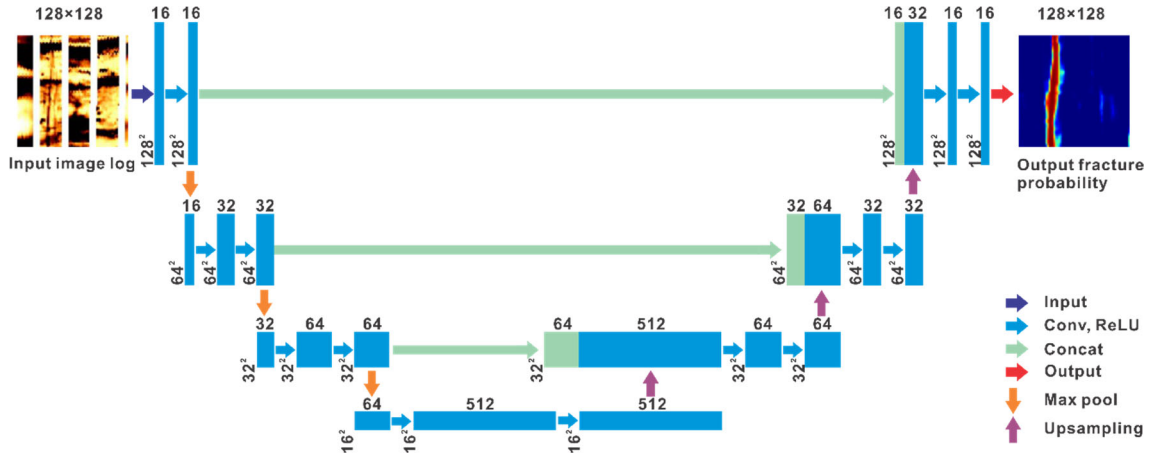

Figure 4.4. Topology of the simplified U-Net used in this study.

U-Net is typically composed of four types of layers: convolutional, concatenation, max pooling, and upsampling layers (input and output layers are convolutional layers). Convolutional layers are responsible for detecting local image features and their nodes only connect to a small spatial subsets of input image channels through sets of shared weights. Each set of shared weights is known as a kernel (or filter). For convolutional layers, one (e.g., grayscale) or more (e.g., RGB or outputs from previous convolutional layers) two-dimensional (2D) arrays (channels) are input and multiple 2D arrays are output. The following equation is used to generate a single output array from a convolutional layer:

$$\mathbf{A}_j = f\left(\sum_{i=1}^{N} \mathbf{I}_i * \mathrm{K}_j + B_j\right) \qquad j = 1,\mathrm{K}\ J. \tag{24}$$

Above, each input array, $\mathbf{I}_i$, which is one of N channels of an image, is convoluted with (*) with filter $\mathbf{K}j$. Then bias B_j is added to the sum of these convoluted matrices to

produce a total input. Ultimately, nonlinear activation function, f (sigmoid for the output layer and ReLU for all other layers), is applied to each element of the matrix of total inputs to produce output matrix $\mathbf{A}_j$. Each of these 2D output matrices, one for each of J filters, is assembled into a 3D tensor. The goal of the training process is to find the components of each filter that extract appropriate image features for optimal image segmentation.

To reduce the computational expense and to extract hierarchical image features (patterns such as edges that assemble into higher-order features), a convolutional layer is followed by a pooling layer. Max pooling layers decrease the dimensions of feature maps (outputs from convolutional layers) by selecting the maximum value from within a user-defined number of neighboring elements (e.g., 4 for a 2×2 kernel size):

$$\mathbf{A}_j^l = \max_s \left(\mathbf{A}_j^{l-1} \right). \tag{25}$$

Here, the output from the upstream convolutional layer, $\mathbf{A}_j^{l-1}$, has its maximum value extracted from each distinct $s \times s$ pooling block, all of which are assembled into $\mathbf{A}_j^l$. The output tensor is s times smaller along both spatial dimensions, but the number of output arrays remains the same.

The image-to-image process of U-Net cannot be implemented without using upsampling layers. Upsampling layers increase the feature map dimensions from previously extracted semantic information until the dimensions of input image are achieved. The upsampling method used in this study was bilinear interpolation. The elements of an input tensor were sparsely and evenly placed to an enlarged tensor. The

empty positions in the enlarged tensor were filled using bilinear interpolation that honors the closest known elements at the four corners of each empty position:

$$\mathbf{A}_j^l = \mathrm{up}_s\left(\mathbf{A}_j^{l-1}\right), \tag{26}$$

where the output tensor is s times larger than the input and the numbers of output arrays remains the same.

Concatenation layers are used in the expanding path to include global context:

$$\mathbf{X}_{\mathrm{con}} = \left[\mathbf{X}_1, \mathbf{X}_2\right], \tag{27}$$

where $\mathbf{X}_{\mathrm{con}}$ is the output concatenated 3D tensor (feature map), $\mathbf{X}_1$ is the 3D tensor that is not upsampled and contains global information while $\mathbf{X}_2$ is the 3D tensor from an upsampling layer.

The cross-entropy loss function for general binary image segmentation is:

$$\mathcal{L}\left(y_i, \hat{y}_i\right) = -\sum_{i=1}^{N} y_i \log(\hat{y}_i) - \sum_{i=1}^{N}\left(1-y_i\right)\log(1-\hat{y}_i), \tag{28}$$

where y_i is a binary label (0 or 1) for a single pixel, $\hat{y}_i$ is the corresponding prediction ($0 < \hat{y}_i < 1$), and N is the number of pixel in a sample (128×128 = 16,384). However, due to significantly different numbers of fracture and non-fracture pixels (fracture pixels do not exceed 1.6% of the total number of pixels in this training dataset), the U-Net model can erroneously achieve a high accuracy by correctly determining the non-fracture pixels and misidentifying the few fracture pixels. To overcome this shortcoming of the original cross-entropy loss function when applied to imbalanced datasets, a balanced cross-entropy loss function was proposed (Xie and Tu 2015). This method first calculates the class-balancing weight, which is the ratio of non-fracture to total pixels:

$$\beta = \sum_{i=1}^{N} \frac{1 - y_i}{N}. \tag{29}$$

Thus $1 - \beta$ denotes the ratio of fracture-to-total pixels while $\beta / 1 - \beta$ is the ratio of non-fracture-to-fracture pixels. If $\beta = 1$, $\beta / 1 - \beta$ cannot be solved so samples without fracture pixels were excluded. The balanced cross-entropy loss function is:

$$\mathcal{L}\left(y_i, \hat{y}_i\right) = -\beta \sum_{i=1}^{N} y_i \log(\hat{y}_i) - \left(1 - \beta\right) \sum_{i=1}^{N} \left(1 - y_i\right) \log(1 - \hat{y}_i). \tag{30}$$

The U-Net used here was built with TensorFlow GPU 1.8.0 and Keras GPU 2.2.4. TensorFlow is an open-source software library for deep learning written in Python. Keras is a high-level neural network application program interface capable of running on top of TensorFlow. An epoch is defined as presentation of all samples in a training dataset to the network.

A continuous section of 83 ft (25.3 m) of image logs (120 pixels per foot) was supplied to the trained U-Net model to test its performance. Given that there were two image samples across the 200-pixel width of the borehole, a 56-pixel horizontal overlap was required as shown in Figure 4.5(a). This necessitated a post-processing step applied to each sample's prediction to seamlessly stitch together overlapping samples. This was achieved by element-wise multiplication of the prediction matrix by a filter matrix where the filter component for non-overlapping pixels was 1 and was weighted using a Gaussian distribution that was a function of overlap distance when corresponding to an overlapping pixel (shaded light blue in Figure 4.5(b)) (Wu et al., 2019).

In addition to the 56-pixel horizontal overlap, an approach using an 8-pixel vertical overlap to stitch together vertically adjacent samples (Figure 5(b)) was compared to a run without vertical overlap.

Predictions were element-wise multiplied by a Gaussian weight filter:

$$w_d = \exp\left[-\frac{8(D-d)^2}{D^2}\right], \tag{31}$$

where d is the distance index for a pixel in an overlapping area and D is the width of overlapping pixels (1 for the pixels on the border to $D = 8$ or 56 for the pixels at the innermost row or column of the overlapping areas). Results were compared both with and without the 8-pixel vertical overlap.

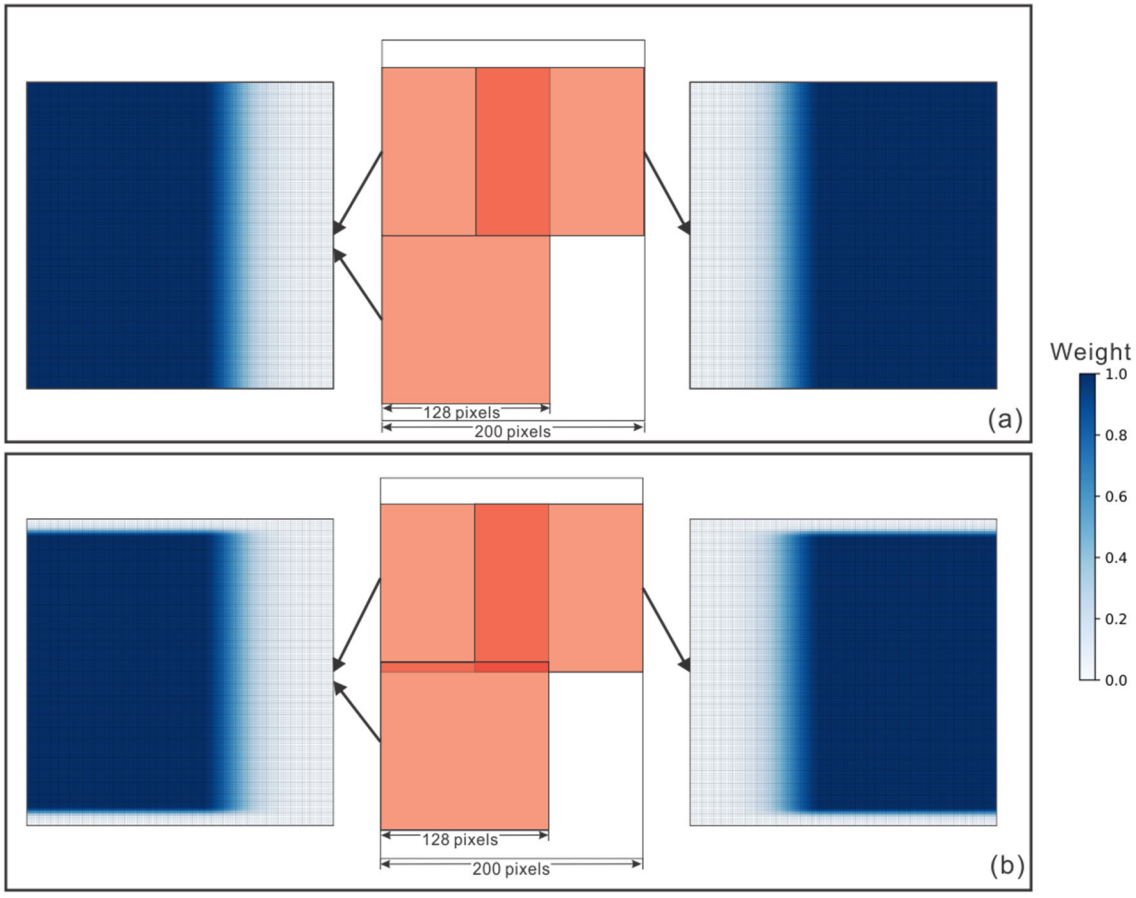

Figure 4.5. In the center, red squares represent adjacent image-log samples and dark red areas denote overlapping pixels. To each side are the post-processing filters with the intensity of the blue color indicating the weight. (a) No vertical overlapping with Gaussian weighting (as a function of overlap distance) in the 56-pixel overlapping areas. (b) Eight-pixel vertical overlap with Gaussian weighting.

Results and Discussion

The U-Net architecture was trained using both the original and augmented datasets. Predictions with different training datasets and with or without vertical overlap were compared using standard AUC (Area Under the Curve)-ROC (Receiver Operating Characteristics) curves (Figure 4.6). The model trained by original data without VO showed slightly weak performance and rest three exercises performed similarly strong (Table 4.1).

Because of the unbalanced nature of the datasets (60× more fracture than non-fracture pixels), the Intersection Over Union (IOU), known as the Jaccard Index, was used to further assess performance. The IOU is calculated as the area of the intersection between the predicted segmentation and true label divided by the area of the union between the predicted segmentation and true label (1 represents perfect segmentation and 0 denotes zero prediction accuracy). Table lists the IOUs calculated for the non-fracture pixels, the fracture pixels, and their arithmetic average. The augmented dataset outperformed the original dataset, which was expected given the larger size of the training dataset. The results also show that VO can improve average IOU by 5.9% for the model trained on the original dataset and 3.3% on the model trained on the augmented dataset.

Figure 4.6. AUC-ROC curves were used to evaluate the U-Net fracture segmentation methods with different datasets and with and without vertical overlap (VO).

Table 4.1. AUC and IOU measurements for four exercises with different datasets and with and without VO.

Metrics	Original dataset	Original dataset with VO	Augmented dataset	Augmented dataset with VO
AUC	0.967	0.989	0.983	0.990
IOU (non-fracture)	0.899	0.921	0.964	0.970
IOU (fracture)	0.215	0.259	0.420	0.460
IOU (average)	0.557	0.590	0.692	0.715

Figure 4.7 shows 8 ft (2.4 m) of input images and the corresponding probability that a pixel is a fracture. The model trained on only the original datasets reveals quite a bit of misprediction (second and third columns in Figure 4.7). The model trained with the augmented dataset shows a significant improvement (fourth and fifth columns in Figure 4.7). Noise is evident on the stitching lines between image logs for predictions

made without VO (second and fourth columns in Figure 4.7), whereas that noise was significantly reduced in predictions with VO (third and fifth columns in Figure 4.7).

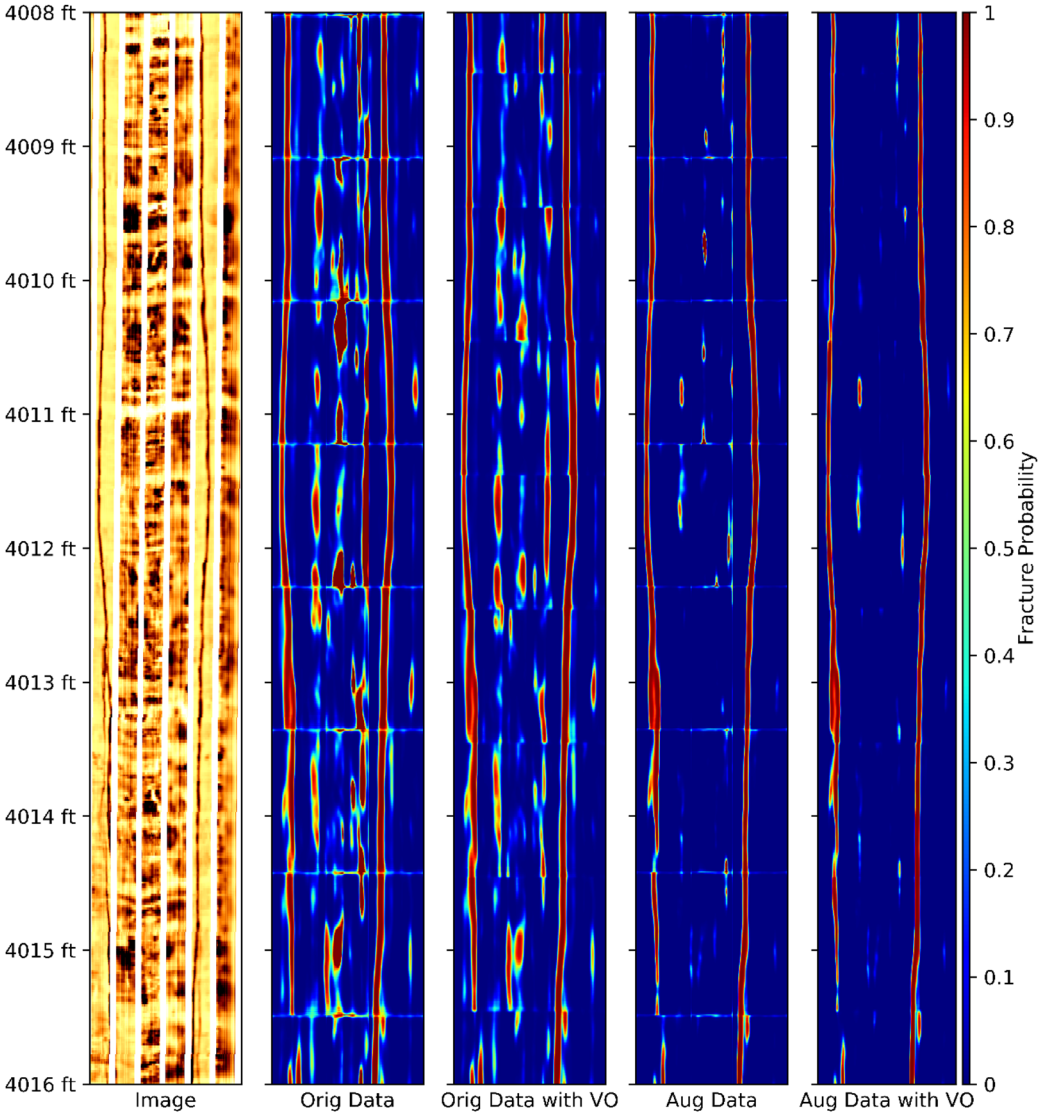

Figure 4.7. Eight feet of U-Net predictions presented as the probability. The first column is input image data. The second to fifth columns indicate prediction probabilities from models trained with the original and augmented datasets and predicted with or without VO.

Both the original and augmented datasets were trained using 200 epochs (i.e., the number of times that the neural network is fed the entire dataset). Each dataset was divided into minibatches composed of 32 samples. Network weights and biases were

updated at end of each minibatch to gradually reduce prediction error (loss). Recall that the augmented dataset (with 620 samples) was twice the size of the original dataset (310 samples). With the fixed minibatch size, the model trained on the augmented dataset had network weights and biases updated twice as many times. To confirm that performance improvement was correctly attributed to the data augmentation and not the more frequent weights/biases updates, the model trained on the original dataset was specified to run for 400 epochs (twice as many to yield the same number of network weights/biases updates as the augmented dataset), but no additional improvements resulted.

The final assignment of a pixel as either fracture or non-fracture was made using a probability threshold of 0.5 (<0.5 is non-fracture, ≥0.5 is fracture) as shown in Figure 4.8. The model trained with the augmented dataset shows robust tracing of all fractures although they were predicted to be slightly thicker than the true fractures (see, for example, the log between 4,103 (1,250.9) and 4,014 ft (1,223.5 m)). Final predictions made without VO show discontinuities between adjacent vertical images because some of that noise was greater than the threshold value. Implementing VO improved model performance.

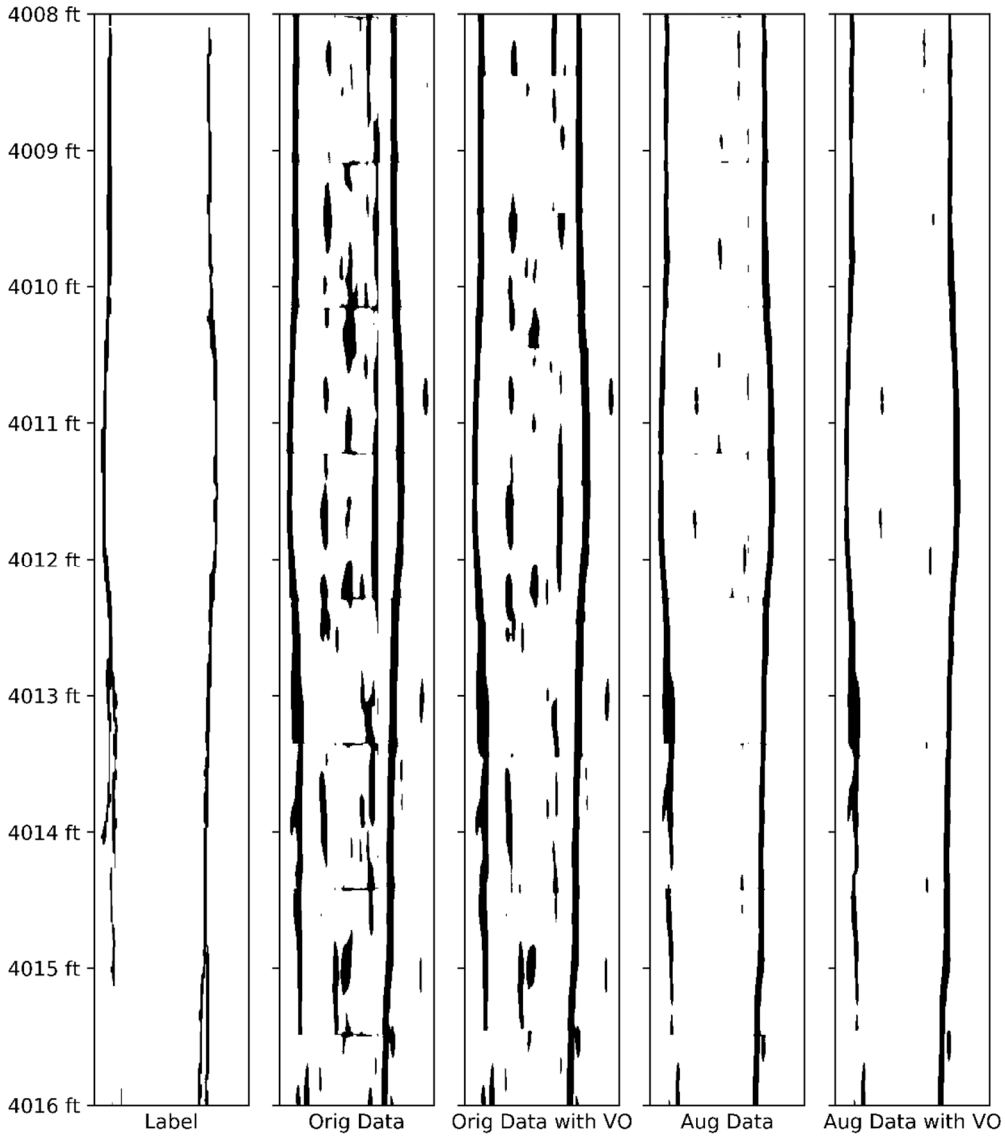

Figure 4.8: Final image segmentation corresponding to the probabilities in Figure 4.7. The first column is the label. The second to fifth columns indicate predictions from models trained with the original or augmented datasets and predicted with or without VO.

Conclusions and Future Work

In this study, pixel-wise manual fracture labeling was done on 583 ft (177.7 m) of microresistivity image logs (500 ft (152.4 m) for training and 83 ft (25.3 m) for testing) from the Wellington 1-32 borehole. Images without fractures in them were discarded leaving 310 samples in the original training dataset. An augmented dataset was generated by simply reversing the images and labels (double the size of the original training dataset). Next, an FCN-based U-Net framework was customized to segment DIFs from microresistivity image logs. To accommodate the unbalance dataset (fracture pixels were only 1.6% of all pixels), the balanced cross-entropy loss function was used. Finally, two trained U-Net models (original and augmented datasets) generate predictions with and without VO. The AUC-ROC curves, typically used to quantify the performance of segmentation tasks, were virtually indistinguishable across the four sets of predictions. Instead, the IOU metric better indicated relative performances. Training on the augmented dataset significantly improved segmentation performance (21.2% improvement over predictions trained with the original dataset). Use VO also improved segmentation performance (5.9% improvement with the original dataset and 3.3% with the augmented dataset).

Historically, machine-learning applications in the geosciences have been hindered by insufficient data availability for model training (a large labeled dataset). This study demonstrated how a small dataset can be used to successfully perform image segmentation especially upon implementation of data augmentation.

The overarching goal of this effort was to segment natural fractures from image logs. However, this dataset did not include many natural fractures, instead having DIFs.

As a follow-on to this work, a labeled dataset with natural fractures will be supplied to this U-net model to determine whether it can also segment natural fractures. Moreover, this study can be easily extended to identify other geological features from image logs including beddings and vugs.

Acknowledgments

The authors wish to acknowledge the use of Aramco Americas Houston Research Center facilities for this study that resulted in this paper. Jiajun Jiang was a graduate intern by Aramco Americas during the time the study was conducted and the paper was written.

References

Abràmoff, M. D., Magalhães, P. J., and Ram, S. J. 2004. Image Processing with Imagej. *Biophotonics international* **11** (7): 36-42.

Barton, C. A. and Zoback, M. D. 2002. Wellbore Imaging Technologies Applied to Reservoir Geomechanics and Environmental Engineering. *Geological applications of well logs: AAPG Methods in Exploration* **13**: 229-239.

Bell, J. and Gough, D. 1979. Northeast-Southwest Compressive Stress in Alberta Evidence from Oil Wells. *Earth and planetary science letters* **45** (2): 475-482. https://doi.org/10.1016/0012-821x(79)90146-8

Bergen, K. J., Johnson, P. A., Maarten, V. et al. 2019. Machine Learning for Data-Driven Discovery in Solid Earth Geoscience. *Science* **363** (6433): eaau0323. https://doi.org/10.1126/science.aau0323.

Brudy, M. and Zoback, M. 1999. Drilling-Induced Tensile Wall-Fractures: Implications for Determination of in-Situ Stress Orientation and Magnitude. *International Journal of Rock Mechanics and Mining Sciences* **36** (2): 191-215. https://doi.org/10.1016/s0148-9062(98)00182-x

Cole, V. B. 1975. Subsurface Ordovician-Cambrian Rocks in Kansas. *Reprinted 1981ed) Lawrence, Kansas: Kansas Geological Survey* **2**.

Dasgupta, T., Dasgupta, S., and Mukherjee, S. 2019. Image Log Interpretation and Geomechanical Issues. In *Teaching Methodologies in Structural Geology and Tectonics*, 237-251. Springer.

De Bree, P. and Walters, J. 1989. Micro/Minifrac Test Procedures and Interpretation for in Situ Stress Determination. *Proc.,* International Journal of Rock Mechanics and Mining Sciences & Geomechanics Abstracts6, 515-521. https://doi.org/10.1016/0148-9062(89)91429-0

Fellgett, M. W., Kingdon, A., Williams, J. D. et al. 2018. Stress Magnitudes across Uk Regions: New Analysis and Legacy Data across Potentially Prospective Unconventional Resource Areas. *Marine and Petroleum Geology* **97**: 24-31. https://doi.org/10.1016/j.marpetgeo.2018.06.016

He, K., Gkioxari, G., Dollár, P. et al. 2017. Mask R-CNN. *Proc.,* Proceedings of the IEEE international conference on computer vision2961-2969. https://doi.org/10.1109/iccv.2017.322

He, K., Zhang, X., Ren, S. et al. 2016. Deep Residual Learning for Image Recognition. *Proc.,* Proceedings of the IEEE conference on computer vision and pattern recognition770-778. https://doi.org/10.1109/cvpr.2016.90

Ja'fari, A., Kadkhodaie-Ilkhchi, A., Sharghi, Y. et al. 2012. Fracture Density Estimation from Petrophysical Log Data Using the Adaptive Neuro-Fuzzy Inference System. *Journal of Geophysics and Engineering* **9** (1): 105-114. https://doi.org/10.1088/1742-2132/9/1/013

James, S. C., Zhang, Y., and O'Donncha, F. 2018. A Machine Learning Framework to Forecast Wave Conditions. *Coastal Engineering* **137**: 1-10. https://doi.org/10.1016/j.coastaleng.2018.03.004.

Kalchbrenner, N., Grefenstette, E., and Blunsom, P. 2014. A Convolutional Neural Network for Modelling Sentences. *arXiv preprint arXiv:14042188*. https://doi.org/10.3115/v1/p14-1062

Khoshbakht, F., Azizzadeh, M., Memarian, H. et al. 2012. Comparison of Electrical Image Log with Core in a Fractured Carbonate Reservoir. *Journal of Petroleum Science and Engineering* **86**: 289-296. https://doi.org/10.1016/j.petrol.2012.03.007

Kirsch, C. 1898. Die Theorie Der Elastizitat Und Die Bedurfnisse Der Festigkeitslehre. *Zeitschrift des Vereines Deutscher Ingenieure* **42**: 797-807.

Krizhevsky, A., Sutskever, I., and Hinton, G. E. 2012. Imagenet Classification with Deep Convolutional Neural Networks. *Proc.,* Advances in neural information processing systems1097-1105. https://doi.org/10.1145/3065386.

Lai, J., Wang, G., Wang, S. et al. 2018. A Review on the Applications of Image Logs in Structural Analysis and Sedimentary Characterization. *Marine and Petroleum Geology* **95**: 139-166. https://doi.org/10.1016/j.marpetgeo.2018.04.020

Lary, D. J., Alavi, A. H., Gandomi, A. H. et al. 2016. Machine Learning in Geosciences and Remote Sensing. *Geoscience Frontiers* **7** (1): 3-10. https://doi.org/10.1016/j.gsf.2015.07.003.

LeCun, Y., Bengio, Y., and Hinton, G. 2015. Deep Learning. *nature* **521** (7553): 436. https://doi.org/10.1038/nature14539.

Liu, W., Rabinovich, A., and Berg, A. C. 2015. Parsenet: Looking Wider to See Better. *arXiv preprint arXiv:150604579*.

Long, J., Shelhamer, E., and Darrell, T. 2015. Fully Convolutional Networks for Semantic Segmentation. *Proc.,* Proceedings of the IEEE conference on computer vision and pattern recognition3431-3440. https://doi.org/10.1109/cvpr.2015.7298965

Massiot, C., McNamara, D. D., and Lewis, B. 2015. Processing and Analysis of High Temperature Geothermal Acoustic Borehole Image Logs in the Taupo Volcanic Zone, New Zealand. *Geothermics* **53**: 190-201. https://doi.org/10.1016/j.geothermics.2014.05.010

Minaee, S., Boykov, Y., Porikli, F. et al. 2020. Image Segmentation Using Deep Learning: A Survey. *arXiv preprint arXiv:200105566*.

Muniz, M. and Bosence, D. 2015. Pre-Salt Microbialites from the Campos Basin (Offshore Brazil): Image Log Facies, Facies Model and Cyclicity in Lacustrine Carbonates. *Geological Society, London, Special Publications* **418** (1): 221-242. https://doi.org/10.1144/sp418.10

Nie, X., Zou, C., Pan, L. et al. 2013. Fracture Analysis and Determination of in-Situ Stress Direction from Resistivity and Acoustic Image Logs and Core Data in the Wenchuan Earthquake Fault Scientific Drilling Borehole-2 (50–1370 M). *Tectonophysics* **593**: 161-171. https://doi.org/10.1016/j.tecto.2013.03.005

Raaen, A., Horsrud, P., Kjørholt, H. et al. 2006. Improved Routine Estimation of the Minimum Horizontal Stress Component from Extended Leak-Off Tests. *International Journal of Rock Mechanics and Mining Sciences* **43** (1): 37-48. https://doi.org/10.1016/j.ijrmms.2005.04.005

Ronneberger, O., Fischer, P., and Brox, T. 2015. U-Net: Convolutional Networks for Biomedical Image Segmentation. *Proc.,* International Conference on Medical image computing and computer-assisted intervention234-241. https://doi.org/10.1007/978-3-319-24574-4_28

Simonyan, K. and Zisserman, A. 2014. Very Deep Convolutional Networks for Large-Scale Image Recognition. *arXiv preprint arXiv:14091556*.

Szegedy, C., Ioffe, S., Vanhoucke, V. et al. 2017. Inception-V4, Inception-Resnet and the Impact of Residual Connections on Learning. *Proc.,* Thirty-First AAAI Conference on Artificial Intelligence.

Tingay, M., Hillis, R., Morley, C. et al. 2003. Variation in Vertical Stress in the Baram Basin, Brunei: Tectonic and Geomechanical Implications. *Marine and Petroleum Geology* **20** (10): 1201-1212. https://doi.org/10.1016/j.marpetgeo.2003.10.003

USGS. 2006. FGDC Digital Cartographic Standard for Geologic Map Symbolization. *US Geological Survey Techniques and Methods* **11** (A2). https://doi.org/10.3133/tm11a2

Weng, X. 2015. Modeling of Complex Hydraulic Fractures in Naturally Fractured Formation. *Journal of Unconventional Oil and Gas Resources* **9**: 114-135. https://doi.org/10.1016/j.juogr.2014.07.001

Wu, X., Liang, L., Shi, Y. et al. 2019. Faultseg3d: Using Synthetic Data Sets to Train an End-to-End Convolutional Neural Network for 3d Seismic Fault Segmentation. *Geophysics* **84** (3): IM35-IM45. https://doi.org/10.1190/geo2018-0646.1.

Xie, S. and Tu, Z. 2015. Holistically-Nested Edge Detection. *Proc.,* Proceedings of the IEEE international conference on computer vision1395-1403. https://doi.org/10.1109/iccv.2015.164

Xu, C., Misra, S., Srinivasan, P. et al. 2019. When Petrophysics Meets Big Data: What Can Machine Do? *Proc.,* SPE Middle East Oil and Gas Show and Conference. https://doi.org/10.2118/195068-MS.

Zhao, H., Shi, J., Qi, X. et al. 2017. Pyramid Scene Parsing Network. *Proc.,* Proceedings of the IEEE conference on computer vision and pattern recognition2881-2890. https://doi.org/10.1109/cvpr.2017.660

Zhou, S. 1994. A Program to Model the Initial Shape and Extent of Borehole Breakout. *Computers & Geosciences* **20** (7-8): 1143-1160. https://doi.org/10.1016/0098-3004(94)90068-x

Zoback, M. D. 2010. *Reservoir Geomechanics*: Cambridge University Press.

Zoback, M. L. 1992. First‐and Second‐Order Patterns of Stress in the Lithosphere: The World Stress Map Project. *Journal of Geophysical Research: Solid Earth* **97** (B8): 11703-11728. https://doi.org/10.1029/92jb00132

CHAPTER FIVE

Conclusions

Decreasing the environmental footprint and executing data transformation are two ongoing challenges for the petroleum industry. This study, which was split into two parts, studied two selected topics related to these challenges. In the first topic, a multiphase, multicomponent reservoir simulation framework was built to simulate the innovative TEOR method STRIP. In the second topic, geologic features were classified and segmented by deep-learning methods from microresistivity image logs.

In the first topic, an innovative simulation framework, which leverages the advantages of CMG's STARS and GEM emissions simulated STRIP operation. This framework was validated by replicating a simple steam injection case from STARS. Then the performances of STRIP and steam injection were compared. STRIP outperformed traditional steam injection in multiple aspects: same oil produced with less enthalpy injected, lower SOR, and earlier reservoir breakthrough. This framework also demonstrated the significance of solvent CO_2 that decreased heavy oil viscosity and improved oil recovery.

The second topic started with a CNN method to identify vuggy facies from microresistivity image logs. Labels of either vuggy or non-vuggy facies for image logs were interpreted using a combination of core descriptions and conventional data including gamma ray, neutron/density porosity, photoelectric factor, and NMR T2. As a comparison, a cleaned dataset was generated by removing images with poor quality.

After hyperparameter optimization, the prediction accuracies of CNN models were improved. The results illustrated that the data-cleaning process had the capacity to further improve model performance. Domain knowledge, insight from data science, and sufficient training data are needed to further improve prediction accuracy for classifying heterogeneous geologic features.

The second topic was extended to segment DIFs from same image-log dataset. 583 ft of microresistivity image log were manually labeled and split into training and test datasets. A data-augmentation method, simply reversing the input images and corresponding labels, doubled the training dataset size for a comparison. An FCN-based U-Net method was customized to segment DIFs. The results showed that data augmentation can significantly improve model performance. Making prediction with VO also improved performance.

BIBLIOGRAPHY

Abràmoff, Michael D, Magalhães, Paulo J, and Ram, Sunanda J. 2004. Image processing with ImageJ. *Biophotonics international* **11** (7): 36-42.

Adler, Frank J, Adler, Frank J, Caplan, William M et al. 1971. Future Petroleum Provinces of the Mid-Continent, Region 7. *Future petroleum provinces of the United States: Their geology and potential: AAPG Memoir* **15**: 985–1120. https://doi.org/10.1306/02060705012.

Alberti, Michele, Pondenkandath, Vinaychandran, Würsch, Marcel et al. 2018. DeepDIVA: a highly-functional python framework for reproducible experiments. Presented at the 2018 16th International Conference on Frontiers in Handwriting Recognition (ICFHR), Niagara Falls, NY, USA,. https://doi.org/10.1109/ICFHR-2018.2018.00080.

Ausbrooks, Robin, Hurley, Neil F, May, Andrew et al. 1999. Pore-size distributions in vuggy carbonates from core images, NMR, and capillary pressure. Presented at the SPE annual technical conference and exhibition, Houston, TX. SPE-56506-MS. https://doi.org/10.2118/56506-MS.

Aziz, Khalid and Settari, Antonin. 1979. *Petroleum Reservoir Simulation*: Chapman & Hall.

Barton, Colleen A and Zoback, Mark D. 2002. Wellbore imaging technologies applied to reservoir geomechanics and environmental engineering. *Geological applications of well logs: AAPG Methods in Exploration* **13**: 229-239.

Bell, JS and Gough, DI. 1979. Northeast-southwest compressive stress in Alberta evidence from oil wells. *Earth and planetary science letters* **45** (2): 475-482. https://doi.org/10.1016/0012-821x(79)90146-8

Bergen, Karianne J, Johnson, Paul A, Maarten, V et al. 2019. Machine learning for data-driven discovery in solid Earth geoscience. *Science* **363** (6433): eaau0323. https://doi.org/10.1126/science.aau0323.

Brudy, Mo and Zoback, MoD. 1999. Drilling-induced tensile wall-fractures: implications for determination of in-situ stress orientation and magnitude. *International Journal of Rock Mechanics and Mining Sciences* **36** (2): 191-215. https://doi.org/10.1016/s0148-9062(98)00182-x

Chang, Yih-Bor, Coats, Brian K, and Nolen, James S. 1996. A Compositional Model for CO_2 Floods Including CO_2 Solubility in Water. *SPE Res Eval & Eng* **1** (2): 155-160. SPE-35164-PA. https://doi.org/10.2118/35164-PA.

Chen, Matthew C, Ball, Robyn L, Yang, Lingyao et al. 2017. Deep learning to classify radiology free-text reports. *Radiology* **286** (3): 845-852. https://doi.org/10.1148/radiol.2017171115.

Chen, Y, Voskov, D, and Khait, M. 2018. Optimization of CO_2 Injection Using Multi-Scale Reconstruction of Compositional Transport. *Proc.,* ECMOR XVI-16th European Conference on the Mathematics of Oil Recovery, Barcelona, Spain, 3–6 September. https://doi.org/10.3997/2214-4609.201802240.

Choquette, Philip W and Pray, Lloyd C. 1970. Geologic nomenclature and classification of porosity in sedimentary carbonates. *AAPG bulletin* **54** (2): 207-250. https://doi.org/10.1306/5D25C98B-16C1-11D7-8645000102C1865D.

Chow, L and Butler, RM. 1996. Numerical simulation of the steam-assisted gravity drainage process (SAGD). *Journal of Canadian Petroleum Technology* **35** (06): 9. PETSOC-96-06-06. https://doi.org/10.2118/96-06-06.

CMG. 2015a. CMG GEM User's Guide.

CMG. 2015b. CMG STARS User's Guide.

CMG. 2015c. CMG WINPROP User's Guide.

Cole, Virgil B. 1975. Subsurface Ordovician-Cambrian Rocks in Kansas. *Reprinted 1981ed) Lawrence, Kansas: Kansas Geological Survey* **2**.

Collins, D. A., Nghiem, L. X., Li, Y. K. et al. 1992. An Efficient Approach to Adaptive-implicit Compositional Simulation with an Equation of State. *SPE Journal* **7** (02): 395-401. SPE-15133-PA. https://doi.org/10.2118/15133-PA.

Cunningham, Kevin J, Carlson, Janine I, and Hurley, Neil F. 2004. New method for quantification of vuggy porosity from digital optical borehole images as applied to the karstic Pleistocene limestone of the Biscayne aquifer, southeastern Florida. *Journal of Applied Geophysics* **55** (1-2): 77-90. https://doi.org/10.1016/j.jappgeo.2003.06.006.

Cyr, Ted, Coates, Roy, and Polikar, Marcel. 2001. Steam-assisted gravity drainage heavy oil recovery process; International (PCT) Patent No. 6,257,334.

Dasgupta, Troyee, Dasgupta, Swagato, and Mukherjee, Soumyajit. 2019. Image Log Interpretation and Geomechanical Issues. In *Teaching Methodologies in Structural Geology and Tectonics*, 237-251. Springer.

De Bree, P and Walters, JV. 1989. Micro/minifrac test procedures and interpretation for in situ stress determination. *Proc.,* International Journal of Rock Mechanics and Mining Sciences & Geomechanics Abstracts6, 515-521. https://doi.org/10.1016/0148-9062(89)91429-0

Dhima, Aleksandër, de Hemptinne, Jean-Charles, and Jose, Jacques. 1999. Solubility of hydrocarbons and CO2 mixtures in water under high pressure. *Industrial & engineering chemistry research* **38** (8): 3144-3161. https://doi.org/10.1021/ie980768g.

Doherty, John E. 2016a. Model-independent Parameter Estimation User Manual Part I: PEST, SENSAN and Global Optimisers, PEST Manual, Watermark Numerical Computing, Brisbane, Australia.

Doherty, John E. 2016b. Model-independent Parameter Estimation User Manual Part II: PEST Utility Support Software, PEST Addendum, Watermark Numerical Computing, Brisbane, Australia.

Doveton, John and Watney, Lynn. 2014. Textural and pore size analysis of carbonates from integrated core and nuclear magnetic resonance logging: An Arbuckle study. *Interpretation* **3** (1): SA77-SA89. https://doi.org/10.1190/INT-2014-0050.1.

Ertekin, Turgay, Abou-Kassen, Jamal H, and King, Gregory R. 2001. *Basic Applied Reservoir Simulations*: Society of Petroleum Engineers.

Fellgett, Mark W, Kingdon, Andrew, Williams, John DO et al. 2018. Stress magnitudes across UK regions: new analysis and legacy data across potentially prospective unconventional resource areas. *Marine and Petroleum Geology* **97**: 24-31. https://doi.org/10.1016/j.marpetgeo.2018.06.016

Franseen, EK. 1994. Facies and porosity relationships of Arbuckle Strata: initial observations from two cores, Rice and Rush Counties, Kansas: Kansas Geol. *Survey Open-File Rep*: 94-53.

Franseen, EK. 2000. A review of Arbuckle Group strata in Kansas from a sedimentologic perspective: Insights for future research from past and recent studies. *The Compass: Earth Science Journal of Sigma Gamma Epsilon* **75** (2-3): 68-89.

Franseen, Evan K, Brynes, Alan P, Cansler, Jason R et al. 2004. The geology of Kansas Arbuckle Group. *Midcontinent Geoscience*: 1-43.

Franseen, Evan K and Byrnes, Alan P. 2012. Arbuckle Group platform strata in Kansas: A synthesis.

Ganapathy, Chandrashekar and Voskov, Denis V. 2018. Multiscale Reconstruction in Physics for Compositional Simulation. *Journal of Computational Physics* **375**: 747-762. https://doi.org/10.1016/j.jcp.2018.08.046.

Harvey, Allan H. 1996. Semiempirical correlation for Henry's constants over large temperature ranges. *AIChE Journal* **42** (5): 1491-1494. https://doi.org/10.1002/aic.690420531.

Hassanzadeh, Hassan, Pooladi-Darvish, Mehran, Elsharkawy, Adel M. et al. 2008. Predicting PVT data for CO2–brine mixtures for black-oil simulation of CO2 geological storage. *International Journal of Greenhouse Gas Control* **2** (1): 65-77. https://doi.org/10.1016/S1750-5836(07)00010-2.

He, Kaiming, Gkioxari, Georgia, Dollár, Piotr et al. 2017. Mask r-CNN. *Proc.,* Proceedings of the IEEE international conference on computer vision2961-2969. https://doi.org/10.1109/iccv.2017.322

He, Kaiming, Zhang, Xiangyu, Ren, Shaoqing et al. 2016. Deep residual learning for image recognition. *Proc.,* Proceedings of the IEEE conference on computer vision and pattern recognition770-778. https://doi.org/10.1109/cvpr.2016.90

Hecht, Ethan S, Shaddix, Christopher R, Houf, William G et al. 2011. Evaluation of Light-Off Limits for a Novel Oxy-Combustion Process for Advanced EOR, Sandia National Lab.

Heidari, Mohammadreza. 2014. *Equation of State Based Thermal Compositional Reservoir Simulator for Hybrid Solvent/Thermal Processes*. PhD, University of Calgary, Calgary, Alberta, Canada.

Hill, Richard W., Dewey, F. Skinner, and Thorsness, Charles B. 1985. Silane-propane ignitor/burner. USA Patent Application No. 498,438; International (PCT) Patent No. 4,499,945.

Hu, Fan, Xia, Gui-Song, Hu, Jingwen et al. 2015. Transferring deep convolutional neural networks for the scene classification of high-resolution remote sensing imagery. *Remote Sensing* **7** (11): 14680-14707. https://doi.org/10.3390/rs71114680.

Ja'fari, Ahmad, Kadkhodaie-Ilkhchi, Ali, Sharghi, Yoosef et al. 2012. Fracture density estimation from petrophysical log data using the adaptive neuro-fuzzy inference system. *Journal of Geophysics and Engineering* **9** (1): 105-114. https://doi.org/10.1088/1742-2132/9/1/013

James, S. C., Moore, K., Muuray, D. et al. 2014. RII NA's STRIP Technology Pilot Project: Progress Report, 1206940.000 2746, E^{x}ponent, Inc., Irvine, CA.

James, S. C., Murray, D., Caffaro, L. et al. 2015. RII NA's STRIP Technology Pilot Project: Summary Report, Baylor University, Waco, TX.

James, S. C., Shaddix, Christopher R., Hecht, Ethan S. et al. 2012. Solvent Thermal Resource Innovations Process (STRIP) Research and Development Report, E^{x}ponent Inc., Irvine, CA.

James, Scott C, Zhang, Yushan, and O'Donncha, Fearghal. 2018. A machine learning framework to forecast wave conditions. *Coastal Engineering* **137**: 1-10. https://doi.org/10.1016/j.coastaleng.2018.03.004.

Jobe, TD, Vital-Brazil, E, and Khaif, M. 2018. Geological Feature Prediction Using Image-Based Machine Learning. *Petrophysics* **59** (06): 750-760. https://doi.org/10.30632/PJV59N6-2018a1.

Jungmann, Matthias, Kopal, Margarete, Clauser, Christoph et al. 2011. Multi-class supervised classification of electrical borehole wall images using texture features. *Computers & geosciences* **37** (4): 541-553. https://doi.org/10.1016/j.cageo.2010.08.008.

Kalchbrenner, Nal, Grefenstette, Edward, and Blunsom, Phil. 2014. A convolutional neural network for modelling sentences. *arXiv preprint arXiv:14042188*. https://doi.org/10.3115/v1/p14-1062

Keroher, Raymond P and Kirby, Jewell J. 1948. *Upper Cambrian and Lower Ordovician rocks in Kansas*: University of Kansas publications.

Khait, M, Voskov, D, and Konidala, G. 2018. Tie-Simplex Parametrization For Operator-Based Linearization For Non-Isothermal Multiphase Compositional Flow In Porous. *Proc.,* ECMOR XVI-16th European Conference on the Mathematics of Oil Recovery, Barcelona, 3-6 September. https://doi.org/10.3997/2214-4609.201802183.

Khoshbakht, F, Azizzadeh, M, Memarian, H et al. 2012. Comparison of electrical image log with core in a fractured carbonate reservoir. *Journal of Petroleum Science and Engineering* **86**: 289-296. https://doi.org/10.1016/j.petrol.2012.03.007

Kirsch, C. 1898. Die theorie der elastizitat und die bedurfnisse der festigkeitslehre. *Zeitschrift des Vereines Deutscher Ingenieure* **42**: 797-807.

Kondo, Shigeo, Tokuhashi, Kazuaki, Nagai, Hidekazu et al. 1994. Experimental study of spontaneous ignition limit of oxygen-lean silane mixtures. *Combustion and Flame* **97** (3): 296-300. https://doi.org/10.1016/0010-2180(94)90022-1.

Kondo, Shigeo, Tokuhashi, Kazuaki, Nagai, Hidekazu et al. 1995. Spontaneous ignition limits of silane and phosphine. *Combustion and Flame* **101** (1–2): 170-174. https://doi.org/10.1016/0010-2180(94)00175-R.

Krizhevsky, Alex, Sutskever, Ilya, and Hinton, Geoffrey E. 2012. Imagenet classification with deep convolutional neural networks. *Proc.,* Advances in neural information processing systems1097-1105. https://doi.org/10.1145/3065386.

Lai, Jin, Wang, Guiwen, Wang, Song et al. 2018. A review on the applications of image logs in structural analysis and sedimentary characterization. *Marine and Petroleum Geology* **95**: 139-166. https://doi.org/10.1016/j.marpetgeo.2018.04.020

Lake, Larry W. 1989. *Enhanced oil recovery*: Prentice Hall.

Lary, David J, Alavi, Amir H, Gandomi, Amir H et al. 2016. Machine learning in geosciences and remote sensing. *Geoscience Frontiers* **7** (1): 3-10. https://doi.org/10.1016/j.gsf.2015.07.003.

LeCun, Yann and Bengio, Yoshua. 1995. Convolutional networks for images, speech, and time series. *The handbook of brain theory and neural networks* **3361** (10): 1995.

LeCun, Yann, Bengio, Yoshua, and Hinton, Geoffrey. 2015. Deep learning. *nature* **521** (7553): 436. https://doi.org/10.1038/nature14539.

Lee, Hyungtae and Kwon, Heesung. 2017. Going deeper with contextual CNN for hyperspectral image classification. *IEEE Transactions on Image Processing* **26** (10): 4843-4855. https://doi.org/10.1109/TIP.2017.2725580.

Li, Binhui, Tan, Xuequn, Wang, Fuyong et al. 2017. Fracture and vug characterization and carbonate rock type automatic classification using X-ray CT images. *Journal of Petroleum Science and Engineering* **153**: 88-96. https://doi.org/10.1016/j.petrol.2017.03.037.

Liu, Wei, Rabinovich, Andrew, and Berg, Alexander C. 2015. Parsenet: Looking wider to see better. *arXiv preprint arXiv:150604579*.

Long, Jonathan, Shelhamer, Evan, and Darrell, Trevor. 2015. Fully convolutional networks for semantic segmentation. *Proc.,* Proceedings of the IEEE conference on computer vision and pattern recognition3431-3440. https://doi.org/10.1109/cvpr.2015.7298965

Lønøy, Arve. 2006. Making sense of carbonate pore systems. *AAPG bulletin* **90** (9): 1381-1405. https://doi.org/10.1306/03130605104.

Lucia, Angelo. 2010. A MultiScale Gibbs-Helmholtz Constrained Cubic Equation of State. *Journal of Thermodynamics* **2010**. http://dx.doi.org/10.1155/2010/238365.

Lucia, Angelo and Bonk, Brian M. 2012. Molecular Geometry Effects and the Gibbs–Helmholtz Constrained Equation of State. *Computers & Chemical Engineering* **37**: 1-14. https://doi.org/10.1016/j.compchemeng.2011.08.006.

Lucia, Angelo, Bonk, Brian M, Waterman, Richard R et al. 2012. A Multi-scale Framework for Multi-phase Equilibrium Flash. *Computers & Chemical Engineering* **36**: 79-98. https://doi.org/10.1016/j.compchemeng.2011.07.011.

Lucia, F Jerry. 1995. Rock-fabric/petrophysical classification of carbonate pore space for reservoir characterization. *AAPG bulletin* **79** (9): 1275-1300. https://doi.org/10.1306/7834D4A4-1721-11D7-8645000102C1865D.

Lucia, FJ. 1983. Petrophysical parameters estimated from visual descriptions of carbonate rocks: a field classification of carbonate pore space. *Journal of petroleum technology* **35** (03): 629-637. SPE-10073-PA. https://doi.org/10.2118/10073-PA.

Maini, Brij B. 1999. Foamy oil flow in primary production of heavy oil under solution gas drive. *Proc.,* SPE Annual Technical Conference and Exhibition, Houston, TX. SPE-56541-MS. https://doi.org/10.2118/56541-MS.

Marrone, Stefano, Olivieri, Stefano, Piantadosi, Gabriele et al. 2019. Reproducibility of Deep CNN for Biomedical Image Processing Across Frameworks and Architectures. *Proc.,* 2019 27th European Signal Processing Conference (EUSIPCO)1-5. https://doi.org/10.23919/EUSIPCO.2019.8902690.

Massiot, Cécile, McNamara, David D, and Lewis, B. 2015. Processing and analysis of high temperature geothermal acoustic borehole image logs in the Taupo Volcanic Zone, New Zealand. *Geothermics* **53**: 190-201. https://doi.org/10.1016/j.geothermics.2014.05.010

Mifflin, RT, Watts, JW, and Weiser, A. 1991. A fully coupled, fully implicit reservoir simulator for thermal and other complex reservoir processes. Presented at the SPE Symposium on Reservoir Simulation, Anaheim, California. 17–20 February. SPE-21252-MS. https://doi.org/10.2118/21252-MS.

Minaee, Shervin, Boykov, Yuri, Porikli, Fatih et al. 2020. Image Segmentation Using Deep Learning: A Survey. *arXiv preprint arXiv:200105566*.

Moore, Catherine and Doherty, John. 2005. Role of the calibration process in reducing model predictive error. *Water Resources Research* **41** (5). https://doi.org/10.1029/2004WR003501.

Muniz, MC and Bosence, DWJ. 2015. Pre-salt microbialites from the Campos Basin (offshore Brazil): image log facies, facies model and cyclicity in lacustrine carbonates. *Geological Society, London, Special Publications* **418** (1): 221-242. https://doi.org/10.1144/sp418.10

Newberry, BM, Grace, LM, and Stief, DO. 1996. Analysis of carbonate dual porosity systems from borehole electrical images. *Proc.,* Permian Basin Oil and Gas Recovery ConferenceSPE-35158-MS. https://doi.org/10.2118/35158-MS.

Nie, Xin, Zou, Changchun, Pan, Li et al. 2013. Fracture analysis and determination of in-situ stress direction from resistivity and acoustic image logs and core data in the Wenchuan Earthquake Fault Scientific Drilling Borehole-2 (50–1370 m). *Tectonophysics* **593**: 161-171. https://doi.org/10.1016/j.tecto.2013.03.005

Nourozieh, Hossein, Kariznovi, Mohammad, and Abedi, Jalal. 2012. Development and evaluation of a modified experimental apparatus for phase behavior study of solvent–heavy crude systems. *Fuel processing technology* **102**: 116-123. https://doi.org/10.1016/j.fuproc.2012.04.032.

Orr, F.M. 2007. *Theory of Gas Injection Processes*, Vol. 5. Copenhagen, Denmark: Tie-Line Publications.

Pedersen, Karen Schou and Fredenslund, Aage. 1987. An improved corresponding states model for the prediction of oil and gas viscosities and thermal conductivities. *Chemical Engineering Science* **42** (1): 182-186. https://doi.org/10.1016/0009-2509(87)80225-7.

Petroleum Technology Alliance Canada. 2005. PTAC Knowledge Centre: Upstream oil and gas energy efficiency, Petroleum Technology Alliance Canada, Calgary, Alberta, Canada.

Raaen, AM, Horsrud, P, Kjørholt, H et al. 2006. Improved routine estimation of the minimum horizontal stress component from extended leak-off tests. *International Journal of Rock Mechanics and Mining Sciences* **43** (1): 37-48. https://doi.org/10.1016/j.ijrmms.2005.04.005

Rannou, Guillaume, Voskov, Denis, and Tchelepi, Hamdi A. 2013. Tie-line-based K-value Method for Compositional Simulation. *SPE Journal* **16** (06): 1112-1122. PETSOC-96-06-06. https://doi.org/10.2118/167257-PA.

Robinson, D. B. and Peng, D. 1978. *The Characterization of the Heptanes and Heavier Fractions for the GPA Peng-Robinson Programs*. Tulsa, Okla.: Gas Processors Association.

Ronneberger, Olaf, Fischer, Philipp, and Brox, Thomas. 2015. U-net: Convolutional networks for biomedical image segmentation. *Proc.,* International Conference on Medical image computing and computer-assisted intervention234-241. https://doi.org/10.1007/978-3-319-24574-4_28

Ross Jr, Reuben J. 1976. Ordovician sedimentation in the western United States. Presented at the Rocky Mountain Association of Geologists Symposium.

Rubin, Barry and Buchanan, W Lloyd. 1985. A General Purpose Thermal Model. *SPE Journal* **25** (02): 202-214. SPE-11713-PA. https://doi.org/10.2118/11713-PA.

Russakovsky, Olga, Deng, Jia, Su, Hao et al. 2015. Imagenet large scale visual recognition challenge. *International journal of computer vision* **115** (3): 211-252. https://doi.org/10.1007/s11263-015-0816-y.

Saner, WB and Patton, JT. 1986. CO2 recovery of heavy oil: Wilmington field test. *Journal of Petroleum Technology* **38** (07): 769-776. SPE-12082-PA. https://doi.org/10.2118/12082-PA.

Schneider, FN and Owens, WW. 1976. Relative Permeability Studies of Gas-water Flow Following Solvent Injection in Carbonate Rocks. *SPE Journal* **16** (01): 23-30. SPE-5554-PA. https://doi.org/10.2118/5554-PA.

Sigmund, Phillip M. 1976. Prediction of molecular diffusion at reservoir conditions. Part 1-Measurement and prediction of binary dense gas diffusion coefficients. *Journal of Canadian Petroleum Technology* **15** (02). PETSOC-76-02-05. https://doi.org/10.2118/76-02-05.

Simonyan, Karen and Zisserman, Andrew. 2014. Very deep convolutional networks for large-scale image recognition. *arXiv preprint arXiv:14091556*.

Srivastava, Nitish, Hinton, Geoffrey, Krizhevsky, Alex et al. 2014. Dropout: a simple way to prevent neural networks from overfitting. *The journal of machine learning research* **15** (1): 1929-1958. https://dl.acm.org/doi/abs/10.5555/2627435.2670313.

Steinhauff, M, Franseen, EK, and Byrnes, A. 1998. Arbuckle reservoirs in central Kansas—Relative importance of depositional facies, early diagenesis and unconformity karst processes on reservoir properties: Kansas Geological Survey. *Open-file Report*: 98-55.

Szegedy, Christian, Ioffe, Sergey, Vanhoucke, Vincent et al. 2017. Inception-v4, inception-resnet and the impact of residual connections on learning. *Proc.,* Thirty-First AAAI Conference on Artificial Intelligence.

Tharanivasan, Asok Kumar, Yang, Chaodong, and Gu, Yongan. 2006. Measurements of molecular diffusion coefficients of carbon dioxide, methane, and propane in heavy oil under reservoir conditions. *Energy & fuels* **20** (6): 2509-2517. https://doi.org/10.1021/ef060080d.

Tilke, Peter G, Allen, David, and Gyllensten, Asbjorn. 2006. Quantitative analysis of porosity heterogeneity: Application of geostatistics to borehole images. *Mathematical Geology* **38** (2): 155-174. https://doi.org/10.1007/s11004-005-9011-y.

Tingay, MRP, Hillis, RR, Morley, CK et al. 2003. Variation in vertical stress in the Baram Basin, Brunei: tectonic and geomechanical implications. *Marine and Petroleum Geology* **20** (10): 1201-1212. https://doi.org/10.1016/j.marpetgeo.2003.10.003

USGS. 2006. FGDC Digital Cartographic Standard for Geologic Map Symbolization. *US Geological Survey Techniques and Methods* **11** (A2). https://doi.org/10.3133/tm11a2

Van-Quy, N., Simandoux, P., and Corteville, J. 1972. A numerical study of diphasic multicomponent flow. *SPE Journal* **12** (02): 14. SPE-3006-PA. https://doi.org/10.2118/3006-PA.

Varavei, Abdoljalil and Sepehrnoori, Kamy. 2009. An EOS-based compositional thermal reservoir simulator. Presented at the SPE Reservoir Simulation Symposium, Woodlands, Texas. 2–4 February. SPE-119154-MS. https://doi.org/10.2118/119154-MS.

Vik, Bartek, Djurhuus, Ketil, Spildo, Kristine et al. 2007. Characterisation of vuggy carbonates. *Proc.,* SPE/EAGE Reservoir Characterization and Simulation ConferenceSPE-111434-MS. https://doi.org/10.2118/111434-MS.

Voskov, Denis V. 2017. Operator-based linearization approach for modeling of multiphase multi-component flow in porous media. *Journal of Computational Physics* **337**: 275-288. http://dx.doi.org/10.1016/j.jcp.2017.02.041.

Voskov, Denis, Zaydullin, Rustem, and Lucia, Angelo. 2016. Heavy oil recovery efficiency using SAGD, SAGD with propane co-injection and STRIP-SAGD. *Computers & Chemical Engineering* **88**: 115-125. http://dx.doi.org/10.1016/j.compchemeng.2016.02.010.

Walters, Robert F. 1958. Differential entrapment of oil and gas in Arbuckle dolomite of central Kansas. *AAPG Bulletin* **42** (9): 2133-2173.

Weijermars, Ruud. 2011. Credit Ratings and Cash-Flow Analysis of Oil and Gas Companies: Competitive Disadavantage in Financing Costs for Smaller Companies in Tight Capital Markets. *SPE Economics & Management* **3** (02): 54-67. https://doi.org/10.2118/144489-PA.

Weng, Xiaowei. 2015. Modeling of complex hydraulic fractures in naturally fractured formation. *Journal of Unconventional Oil and Gas Resources* **9**: 114-135. https://doi.org/10.1016/j.juogr.2014.07.001

Wilson, JL, Fritz, RD, and Medlock, PL. 1991. The Arbuckle Group: Relationship of core and outcrop analyses to cyclic stratigraphy and correlation. *Proc.,* Arbuckle core workshop and field trip: Oklahoma Geological Survey Special Publication133-144.

Witten, Ian H, Frank, Eibe, Hall, Mark A et al. 2016. *Data Mining: Practical machine learning tools and techniques*: Morgan Kaufmann.

Wu, Xinming, Liang, Luming, Shi, Yunzhi et al. 2019. FaultSeg3D: Using synthetic data sets to train an end-to-end convolutional neural network for 3D seismic fault segmentation. *Geophysics* **84** (3): IM35-IM45. https://doi.org/10.1190/geo2018-0646.1.

Xie, Saining and Tu, Zhuowen. 2015. Holistically-nested edge detection. *Proc.,* Proceedings of the IEEE international conference on computer vision1395-1403. https://doi.org/10.1109/iccv.2015.164

Xu, Chicheng, Misra, Siddharth, Srinivasan, Poorna et al. 2019. When Petrophysics Meets Big Data: What can Machine Do? *Proc.,* SPE Middle East Oil and Gas Show and Conference. https://doi.org/10.2118/195068-MS.

Yamashita, Rikiya, Nishio, Mizuho, Do, Richard Kinh Gian et al. 2018. Convolutional neural networks: an overview and application in radiology. *Insights into imaging* **9** (4): 611-629. https://doi.org/10.1007/s13244-018-0639-9.

Young, Larry C. and Stephenson, Robert E. 1983. A generalized compositional approach for reservoir simulation. *SPE Journal* **23** (05): 727-742. SPE-10516-PA. https://doi.org/10.2118/10516-PA.

Zaydullin, R, Voskov, DV, and Tchelepi, HA. 2017. Comparison of eos-based and k-values-based methods for three-phase thermal simulation. *Transport in Porous Media* **116** (2): 663-686. https://doi.org/10.1007/s11242-016-0795-7.

Zhao, Hengshuang, Shi, Jianping, Qi, Xiaojuan et al. 2017. Pyramid scene parsing network. *Proc.,* Proceedings of the IEEE conference on computer vision and pattern recognition2881-2890. https://doi.org/10.1109/cvpr.2017.660

Zhou, Shaohua. 1994. A program to model the initial shape and extent of borehole breakout. *Computers & Geosciences* **20** (7-8): 1143-1160. https://doi.org/10.1016/0098-3004(94)90068-x

Zoback, Mark D. 2010. *Reservoir geomechanics*: Cambridge University Press.

Zoback, Mary Lou. 1992. First‐and second‐order patterns of stress in the lithosphere: The World Stress Map Project. *Journal of Geophysical Research: Solid Earth* **97** (B8): 11703-11728. https://doi.org/10.1029/92jb00132